FRACTURE TOUGHNESS OF WIRE ARC ADDITIVE MANUFACTURED DUPLEX STAINLESS STEEL GRADE 2509

A THESIS SUBMITTED TO
THE GRADUATE SCHOOL OF NATURAL AND APPLIED SCIENCES
OF
MIDDLE EAST TECHNICAL UNIVERSITY

BY

RAUF BATUHAN ERSAN

IN PARTIAL FULFILLMENT OF THE REQUIREMENTS
FOR
THE DEGREE OF MASTER OF SCIENCE
IN
METALLURGICAL AND MATERIALS ENGINEERING

JANUARY 2023

Approval of the thesis:

FRACTURE TOUGHNESS OF WIRE ARC ADDITIVE MANUFACTURED DUPLEX STAINLESS STEEL GRADE 2509

submitted by **RAUF BATUHAN ERSAN** in partial fulfillment of the requirements for the degree of **Master of Science** i**n Metallurgical and Materials Engineering, Middle East Technical University** by,

Prof. Dr. Halil Kalıpçılar
Dean, Graduate School of **Natural and Applied Sciences** _____

Prof. Dr. Ali Kalkanlı
Head of the Department, **Metallurgical and Materials Eng.** _____

Prof. Dr. Cemil Hakan Gür
Supervisor, **Metallurgical and Materials Eng., METU** _____

Dr. Koray Yurtışık
Co-Supervisor, **Metallurgical and Materials Eng., METU** _____

Examining Committee Members:

Prof. Dr. Rıza Gürbüz
Metallurgical and Materials Eng, METU _____

Prof. Dr. Cemil Hakan Gür
Metallurgical and Materials Eng., METU _____

Prof. Dr. Bilgehan Ögel
Metallurgical and Materials Eng., METU _____

Prof. Dr. Benat Koçkar
Mechanical Eng., Hacettepe University _____

Assoc. Prof. Dr. Caner Şimşir
Metallurgical and Materials Eng., METU _____

Date: 24.01.2023

I hereby declare that all information in this document has been obtained and presented in accordance with academic rules and ethical conduct. I also declare that, as required by these rules and conduct, I have fully cited and referenced all material and results that are not original to this work.

Name, Last name: Rauf Batuhan Ersan

Signature :

ABSTRACT

FRACTURE TOUGHNESS OF WIRE ARC ADDITIVE MANUFACTURED DUPLEX STAINLESS STEEL GRADE 2509

Ersan, Rauf Batuhan
Master of Science, Metallurgical and Materials Engineering
Supervisor: Prof. Dr. Cemil Hakan Gür
Co-Supervisor: Dr. Koray Yurtışık

January 2023, 106 pages

There are two significant benefits of duplex stainless steels as being corrosion resistant and having enhanced mechanical properties. In virtue of these advantages, they are suitable for industries that deal with aggressive environments. Additive manufacturing is a promising technology as it has considerable amount of advantages. Practicality of wire arc additive manufacturing technique, which is an influential method in term of cost and deposition efficiency, for this grade was researched in this study. The microstructure of this grade is changed because of being exposed to instantaneous heating and cooling, therefore handling of ferrite / austenite ratio is a notable parameter. Complex thermal cycles bring formation of secondary phases which are detrimental for properties. Additionally, used shielding gas during process has also essential impression on microstructure and mechanical properties eventually. Since crack like defects are present in structural materials, evaluation is behooved. At this point fracture toughness steps in as it designates criticality of discontinuities. In this work, fracture toughness tests at -10°C temperature with distinctive constraint conditions were applied to wrought material and additively

manufactured coupons which were deposited with different shielding gases. Results together with extensive investigations demonstrate that constraint of single edge notch tension specimen is lower than constraint of single edge notch bend specimen that yields to better resistance for fracture. Moreover, $Ar+O_2$ shielding gas causes oxide inclusions in microstructure which deteriorates crack extension resistance.

Keywords: Duplex Stainless Steels, Fracture Toughness, Wire Arc Additive Manufacturing, Microstructure

ÖZ

TEL ARK KATMANLI ÜRETİLMİŞ 2509 SINIFI ÇİFT FAZLI PASLANMAZ ÇELİKLERİN KIRILMA TOKLUĞU

Ersan, Rauf Batuhan
Yüksek Lisans, Metalurji ve Malzeme Mühendisliği
Tez Yöneticisi: Prof. Dr. Cemil Hakan Gür
Ortak Tez Yöneticisi: Dr. Koray Yurtışık

Ocak 2023, 106 sayfa

Çift fazlı paslanmaz çeliklerin iki önemli avantajı vardır; korozyon direnci ve gelişmiş mekanik özellikler. Bu avantajlara binaen, onlar agresif ortamlara maruz kalınan endüstriler için elverişlidirler. Eklemeli imalat kayda değer avantajlara sahip olması sayesinde gelecek vadeden bir teknolojidir. Maliyet ve üretim verimliliği yönlerinden etkili bir metot olan tel ark katmanlı üretim tekniğinin bu sınıf için uygulanabilirliği bu çalışmada araştırılacaktır. Bu sınıfın mikroyapısı ani ısınma ve soğumaya maruz kalındığı zaman değişmektedir, dolayısıyla ferrit / östenit oranının ayarlanması önemli bir parametredir. Karmaşık termal çevrimler, özellikler için zararlı olan, ikincil fazların oluşmasına neden olurlar. Ayrıca proses esnasında kullanılan koruma gazı da, mikroyapıda ve nihayetinde mekanik özellikler üzerinde önemli etkiye sahiptir. Yapısal malzemelerde çatlak benzeri kusurlar bulunduğundan, bu kusurların değerlendirilmesi gerekmektedir. Bu noktada süreksizliklerin kritikliğini tayin ettiği için kırılma tokluğu devreye girmektedir. Bu çalışmada işlenmiş malzemeye ve farklı koruma gazlarıyla üretilmiş olan eklemeli imalat kuponlarına farklı kısıtlama koşullarına sahip olan kırılma tokluğu testleri -10°C sıcaklığında uygulanmıştır. Kapsamlı araştırmalarla birlikte sonuçlar tek

kenarı çentikli çekme numune kısıtlamasının tek kenarı çentikli eğme numune kısıtlamasından düşük olduğunu, bunun daha iyi kırılma direnci sağladığını göstermiştir. Dahası $Ar+O_2$ koruma gazı, mikroyapıda oksit inklüzyonuna sebep olmuştur, bu durum çatlak ilerleme direncini kötüleştirmiştir.

Anahtar Kelimeler: Çift Fazlı Paslanmaz Çelikler, Kırılma Tokluğu, Tel Ark Katmanlı Üretim, Mikroyapı

To my dear family

ACKNOWLEDGMENTS

I sincerely thank to my supervisor Prof. Dr. C. Hakan Gür for his guidance, advice and encouragement throughout this study.

I would like to express my very deep appreciation to my co-supervisor Dr. Koray Yurtışık for his precious support and motivation. Words are useless to describe valuableness of his teachings in both academic, professional and everyday life.

No doubt that contributions of METU Welding Technology and Non-Destructive Testing Research / Application Center & Ion Industrial Metallurgy Research and Development Inc. are priceless. Dr Süha Tirkeş, Mine Kalkanci, Dr. Göksu Gürer, Murat Tolga Ertürk, Elina Akbarzadeh, Hafize Çakmak Alpaslan, Kaan Uslu, Hande Bilir Bunsuz, Arif Atalay Özdemir, Orhan Aydın and Mevlüt Bağcıoğlu were very helpful during experimental studies in both characterization and fabrication processes.

I owe gratefulness to my lovely parents Ali & Sevim Ersan and my lovely grandparents Nermin Ersan and Döndü Özcan for their endless support, generosity and faith which make the path easier through all time. My friends who have been accompanied me also deserve a regard gramercy.

Finally, I wish to emphasize from the bottom of heart thankfulness to my beloved wife Tuğçe Altuntop Ersan for her infinite contributions and insightfulness in every aspect of my life.

I am always glad to their presence.

TABLE OF CONTENTS

LIST OF TABLES

TABLES

LIST OF FIGURES

FIGURES

LIST OF ABBREVIATIONS

ABBREVIATIONS

3D	Three Dimensional
AM	Additive Manufacturing
ASTM	American Society for Testing and Materials
AWS	American Welding Society
BCL	Bead Centerline
BS	British Standards Institution
CMOD	Crack Mouth Opening Displacement
CMT	Cold Metal Transfer
Cr_{eq}	Chromium Equivalent
CTOD	Crack Tip Opening Displacement
DED	Direct Energy Deposition
DLF	Directed Light Fabrication
DMD	Direct Metal Deposition
DSS	Duplex Stainless Steel
EBM	Electron Beam Melting
EDM	Electrical Discharge Machining
EDX	Energy Dispersive X-ray
EPFM	Elastic Plastic Fracture Mechanics
FL	Fusion Line
GBA	Grain Boundary Austenite
GMAW	Gas Metal Arc Welding
GTAW	Gas Tungsten Arc Welding
HAZ	Heat Affected Zone
HV	Vickers Hardness
IGA	Intragranular Austenite
IGC	Intergranular Corrosion
ISO	International Organization for Standardization

LAM	Laser Augmented Manufacturing
LEFM	Linear Elastic Fracture Mechanics
LENS	Laser Entegrated Net Shaping
NDT	Non-Destructive Testing
Ni_{eq}	Nickel Equivalent
OM	Optical Microscope
PAW	Plasma Arc Welding
PBF	Powder Bed Fusion
PRE_N	Pitting Equivalent Resistance Number
PRE_W	Pitting Resistance Equivalent Number (Including Tungsten)
PT	Penetration Testing
RT	Radiographic Testing
RT	Room Temperature
SCC	Stress Corrosion Cracking
SEM	Scanning Electron Microscope
SENB	Single Edge Notch Bending
SENT	Single Edge Notch Tension
SLM	Selective Laser Melting
SS	Stainless Steel
TTT	Time Temperature Transformation
WA	Widmanstatten Austenite
WAAM	Wire Arc Additive Manufacturing
XRD	X-ray Diffraction

LIST OF SYMBOLS

SYMBOLS

a_0	Initial Crack Length
a_f	Final Crack Length
G	Elastic Energy Release Rate
Hz	Hertz
J	J-integral
K	Stress Intensity Factor
R	R-phase
R_m	Ultimate Tensile Strength
$R_{p0.2}$	0.2% Offset Yield Strength
α	Fe-rich Ferrite
α'	Cr-rich Ferrite
γ	Austenite
γ_2	Secondary Austenite
δ	Delta Ferrite
Δa	Stable Crack Extension
σ	Sigma
χ	Chi

CHAPTER 1

INTRODUCTION

Duplex stainless steel (DSS) has a dual phase microstructure that are ferrite (δ) and austenite (γ). Combination of these two phases yields to superior corrosion resistance and advanced mechanical properties which are vital for aggressive service conditions. Under favor of these features DSS is utilized in nuclear, offshore, oil and gas industry for decades. Equality of phase proportions is significant as properties depend on this rate [1]. Excess austenite results in a decline in strength and hardness as well as over-abundant ferrite lowers toughness and resistance to corrosion. Austenite rate between 35% and 65% is reasonable [2]. Apart from balanced microstructure, formation of secondary phases such as nitrides, carbides and intermetallics (sigma and chi) affects properties of DSS adversely. Additionally, when DSS is exposed to high temperatures, secondary austenite precipitation also occurs upon cooling [3]. Alloying elements and cooling rate are two major parameters that affect balanced microstructure and precipitations of secondary phases [4, 5].

Additive manufacturing (AM) is a novel process which builds structures via deposition of layers. Near net shape components could be produced without wastage of material and time [6, 7]. Since AM has no use for fabrication and assembly tools, it is a cost-effective technique. It has a flexibility in terms of generating customized structures [8]. There are variations of AM techniques. Among them powder bed fusion and direct energy deposition are two main types for producing metallic materials. In these techniques feedstock could be powder or wire whereas heat source could be laser, electron or arc [6]. Wire arc additive manufacturing is a promising

method and it has several benefits such as high deposition rate which enables building of large pieces, producing goods rapidly and reduced cost since it only requires a welding robot and wire [9, 10]. Owing to advantages stated above AM, especially wire arc additive manufacturing, is a more efficient way of fabrication when compared to conventional manufacturing and processing methods.

Production of DSS via wire arc additive manufacturing has some challenging points. During deposition of layers DSS undergoes complex thermal cycles in terms of both heating and cooling subsequently. Integrity, microstructure and properties are impacted greatly due to these steps. If a rapid cooling rate is implemented, ferrite phase dominates the microstructure. On the contrary, when DSS is subjected to slow cooling, austenite formation is favored, but it raises precipitation of detrimental secondary phases [11, 12]. Utilized shielding gas during process has also an effect on microstructure and properties eventually. Secondary austenite, which is re-nucleated after decomposition, influences properties of DSS as well as other secondary phases.

Discontinuities in structures could not be prohibited completely. Hence, determination of whether existing defects are destructive or not becomes a necessity [13]. A phenomenon called fracture toughness identifies resistance to crack propagation of a material [14].

The main objective of this study is investigating fracture toughness properties of wire arc additively manufactured DSS within the scope of different crack tip constraints. Acquired considerations are affirmed together with perspective of microstructure and mechanical metallurgy.

CHAPTER 2

THEORY

2.1 The Process; Wire Arc Additive Manufacturing

Additive manufacturing is a process that creates three dimensional (3D) pieces through adding or joining materials in the pattern of layer upon layer with superior degree of freedom. The phenomenon has been studied since 1980s where it was used only for design purposes at the beginning. Metals, ceramics, polymers and composites could be produced by AM. Synonyms utilized for this technique are rapid prototyping, 3D printing, layer manufacturing, freedom fabrication and so on [15]. In this technique several layers are deposited in horizontal plane on one another and as a result a three-dimensional part is generated along vertical plane as seen in Figure 1 [8].

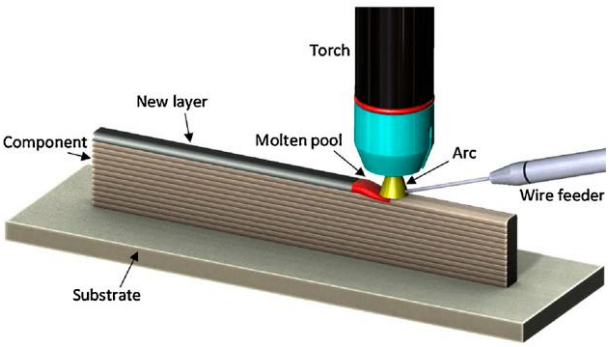

Figure 1. Schematic representation of additive manufacturing [16].

Additive manufacturing has ability to generate complex pieces that are hard or impossible to produce by conventional techniques. Near net shape parts could be manufactured directly in one step. Since scrap is absent or very low, AM consumes excessively less amount of material compared to conventional manufacturing where removal from bulk is performed. Joining of multiple constituents do not require assembly tools such as rivets or screws, therefore lightweight structures could be obtained by AM. Also, the requirement of equipment such as dies, molds, etc. are not necessary for AM. Moreover, customized products could be manufactured on demand without excessive lead time and cost. For these reasons, AM is an environmental friendly method as achieving reduced cost, energy consumption and carbon footprint [8, 17]. According to ASTM F2792 additive manufacturing is categorized as vat-photopolymerization, material extrusion, binder jetting, material jetting, sheet lamination, powder bed fusion and direct energy deposition [18]. Among these, powder bed fusion (PBF) and direct energy deposition (DED) are major processes that are adequate for producing metallic materials with comparable mechanical properties [6, 19]. For metals, additive manufacturing could be classified in terms of; feed stock material, energy source and build volume as seen in Figure 2 [15].

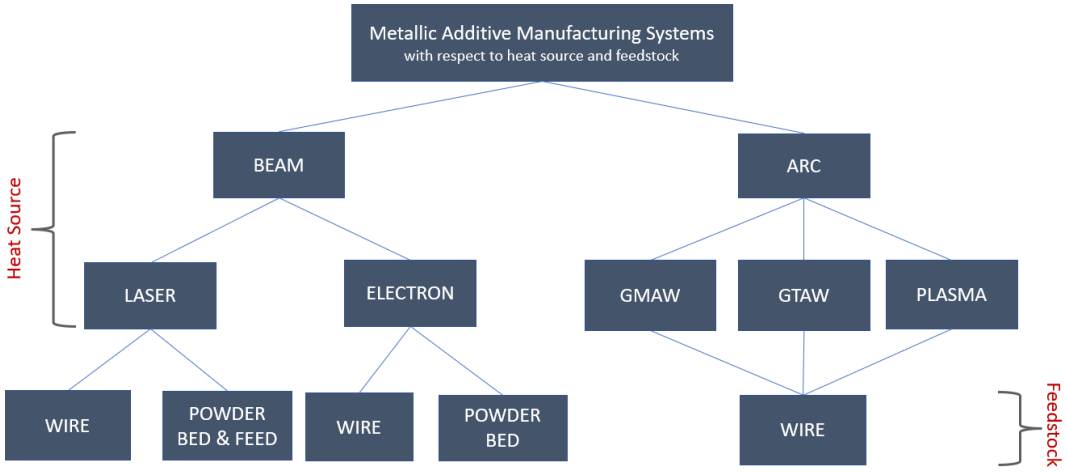

Figure 2. Classification of additive manufacturing in metals.

Generating a part by using powder as feedstock material requires relatively extra time as rate of feeding and speed of scanning have restrictions. Nevertheless, sophisticated objects could be produced via achieving excellent surface finish when powder is utilized. It has ability to fabricate functionally graded materials [20]. Quality of powders is a substantial parameter since it affects quality of process and final product eventually. Size, distribution, shape, purity and porosity of powders are primary factors that influence powder quality. The main drawbacks of powders are their high cost, inefficient usage percentage and being hazardous for both operator and environment [21]. In the case of using wire as feedstock, parts with largest volumes among all could be attained. However, further machining is essential for setting up the final layout as a result of high surface roughness of components that are deposited by wire. For PBF and DED methods energy is evaluated with energy intensity (E_i), linear energy input (E_l) and specific heat input intensity (E_v). These terms are calculated as

$$E_i = \frac{4P}{\pi d^2} \tag{1}$$

$$E_l = \frac{P}{V_s} \tag{2}$$

$$E_i = \frac{4P}{V_s h_s t_l} \tag{3}$$

Where P is power of input, d is heat sources' direct action area's diameter, V_s is speed of scanning, h_s is space of hatching and t_l is thickness of layer.

Laser, beam and plasma are the energy sources that have high E_i. For welding E_l is operative whereas E_v is suitable for PBF [6].

2.1.1 Powder Bed Based Deposition

Volume of manufactured parts, that use powder bed as feedstock, is below 0.03 m^3. The main benefit of powder bed is reproducibility. Energy supplied by electron or laser beam is introduced to surface of bed in order to fuse or sinter the powder. Initially, adequate amount of powder with respect to desired layer thickness is laid over the platform. Certain sections of the powder, which is required to form, is melted. After first layer is formed, the platform lowers its position in order to melt latter layers as new powder is placed on the top of formed structure. This cycles continuous numerous times up to demanded product is finished [22]. Selective laser melting (SLM) and electron beam melting (EBM) are most utilized techniques for powder bed systems. High dimensional precision and extensive workability are prominent characteristics of SLM. In case of EBM, residual stress could be suppressed whereas a vacuum chamber is essential for preventing oxidation [20]. Schematic view of powder bed fusion is represented in Figure 3.

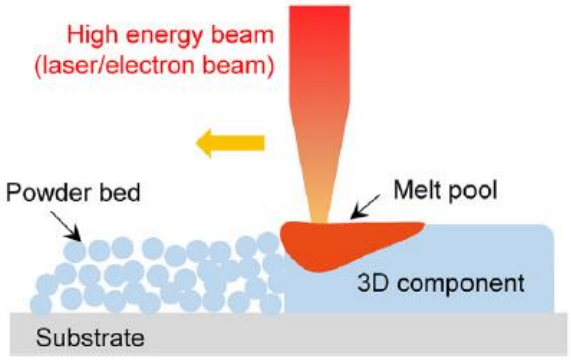

Figure 3. Illustration of powder bed systems [23].

2.1.2 Powder Feed Based Deposition

For systems which use powder feed as feedstock, acquired volumes are greater than 1.2 m^3. This type of AM is also called as powder deposition and it is regarded under DED category. The basis of powder feed method relies on laser cladding phenomena [20]. The energy, which's source is only laser in this case, is utilized for melting the powders. At the first step of this process little amount of melt pool is constituted on base while powders are introduced together with an inert gas stream through a nozzle. As powders are melted in the metal pool and thereafter solidification takes place, deposition is continued according to desired orientation. In order to arrange the deposition path mainly there are two solutions. The base could be fixed whereas the nozzle changes its position according to the base and the nozzle could be fixed whereas the base changes its position according to the nozzle. When desired layer is formed, the nozzle uppers its height for generating latter layers up to final 3D shape is obtained. In Figure 4 illustration of powder feed is shown.

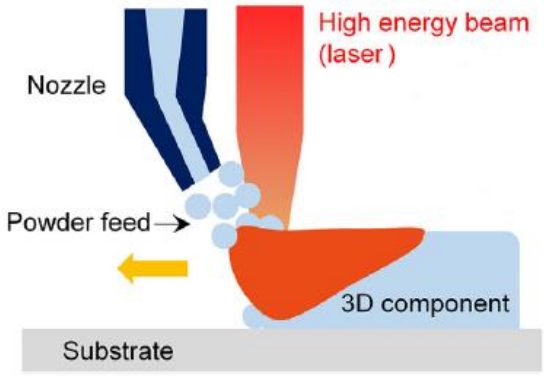

Figure 4. Representation of powder feed systems [23].

In powder feed technique greater volumes could be manufactured compared to powder bed feedstock. In addition, this method could be used for parts which requires repair for both flat and curved surfaces. However, this method may deliver

porosity to structure [20]. Most common techniques for powder feed systems are laser engineered net shaping (LENS), direct metal deposition (DMD), laser augmented manufacturing (LAM) and directed light fabrication (DLF) [22].

2.1.3 Wire Feed Based Deposition

In case of wire is used as feedstock material, components with massive volumes could be manufactured owing to great deposition rate. Wire based method is also under DED category. A variety of energy sources that are electron beam, laser and arc could be applicable to wire feed systems. A molten pool is generated at the base material as first step. Then wire is introduced to molten pool and subsequently energy starts to melt it. Deposition continues as energy source changes its position with respect to desired pattern. Layers, which are consisted of corresponding multiple beads, forms the final shape as passes are completed. Illustration of wire feed system is in Figure 5 [24].

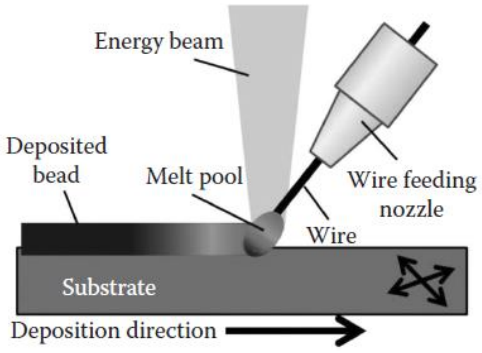

Figure 5. Schematic of wire-based feeding [24].

Productivity of wire-based systems are superior in terms of material utilization and manufacturing time. Since a variety of wires are available commercially, it is an affordable process. On the contrary, lack of precision is observed in terms of

dimensional resolution when compared to powder feeding. This situation gives rise to further treatment such as grinding or machining [24]. Wire feeding is able to produce parts which have moderate complex shapes. Moreover, residual stress and distortions are other concerns for wire-based systems [20, 25].

2.1.3.1 Beam-Based Wire Deposition

Electron beam energy is used for fusing wires in this deposition technique. Beam is an intense energy supplier that has ability to heat specific local zones. Operation is conducted under vacuum environment. Gain of being under vacuum is inhibiting unwanted contamination especially in case of accumulating reactive metals. On the contrary, vacuum rises expense of this process and it causes slow cooling rate which leads to coarser grains [26, 27]. Some metals are reflecting laser energy therefore electron beam is a more appropriate solution for these metals like aluminum and copper. Power and coupling efficiencies are greater when compared to laser-based deposition. Energy efficiency of beam is between 15% to 20% [28].

2.1.3.2 Laser-Based Wire Deposition

In this type of AM, a molten pool is created instantly as laser is applied, usually with a shielding gas, and thereafter metallic wires are delivered and melted inside the melted pool. As in the case of beam, the energy supplied by lasers are intensive and it could be applied to particular local zones with high precision. Combining this fact together with implementation of low power and fine wire size usage, highest resolution is acquired among all wire-based accumulations [27]. However, efficiency of laser energy is lowest (2% - 5%) among all wire feed systems [28]. The main factors that influence properties of end product depend on power of laser, welding speed, feeding rate, feeding orientation and wire type. These parameters are optimized so that desired geometry, microstructure and mechanical properties could be achieved. Handling of wire dipping and stubbing are critical according to build

volume [20, 21, 24]. There are three deposition directions which are front, side and back as seen in Figure 6. In order to obtain smooth finish, front and side deposition are preferable [21]. Highest stability of deposition is attained when wire is applied at leading edge [29]. Feeding rate is adjusted according to implemented laser power so that wires could be able to melt fully. Bead width and height are directly proportional to laser power and welding speed respectively [20].

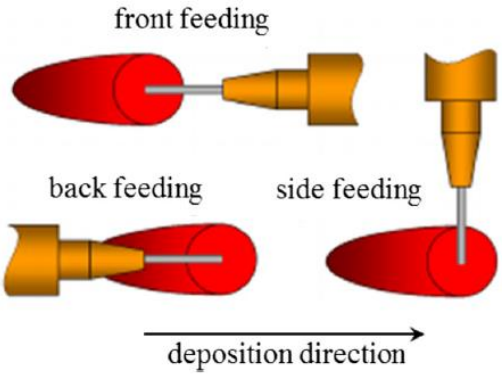

Figure 6. Directions of feeding [20].

2.1.3.3 Arc-Based Wire Deposition

The resource of heating is electric arc, which arises among the electrode and the base, in this case. It is used for melting and accumulating the feedstock with presence of a shielding gas [24]. This technique is known as wire arc additive manufacturing (WAAM) in literature. In terms of cost, arc-based deposition is a very affordable process which is able to build large-scaled and moderate complexity components with simple equipment. Fusion efficiency of arc is superior when compared to beam and laser [27] but greater heat inputs are utilized [6, 19]. As a result of high heat input distortions, residual stresses and need for post processing are deficiencies for WAAM [6]. Heat input (H) is calculated as

$$H = \frac{Arc\ voltage.Arc\ current}{Linear\ welding\ speed} Arc\ efficiency \quad (4)$$

WAAM is mainly classified as gas metal arc welding (GMAW), gas tungsten arc welding (GTAW) and plasma arc welding (PAW) [20].

2.1.3.3.1 Gas Metal Arc Welding (GMAW)

GMAW uses fusible electrodes which is fed through the nozzle of the torch with supplied shielding gas. According to metal type active and inert gases are selected [30]. The electrode has two functions as being the feedstock for accumulation and procuring electrical circuit for arc creation. When arc is formed at tip of electrode, melted drops of the electrode start to exist and deposition begins. Direct current reverse polarity is applied in which positive and negative terminals of power unit are connected to electrode and base respectively [19]. At the anode, heat and temperature are higher therefore electrode melts rapidly that makes deposition rate high. In Figure 7 a representative image of GMAW is seen. Among all WAAM methos GMAW has highest energy efficiency (close to 90%) and deposition rate. In addition, components that have high mechanical strength and density could be generated with high percentage of feedstock consumption in short time [28].

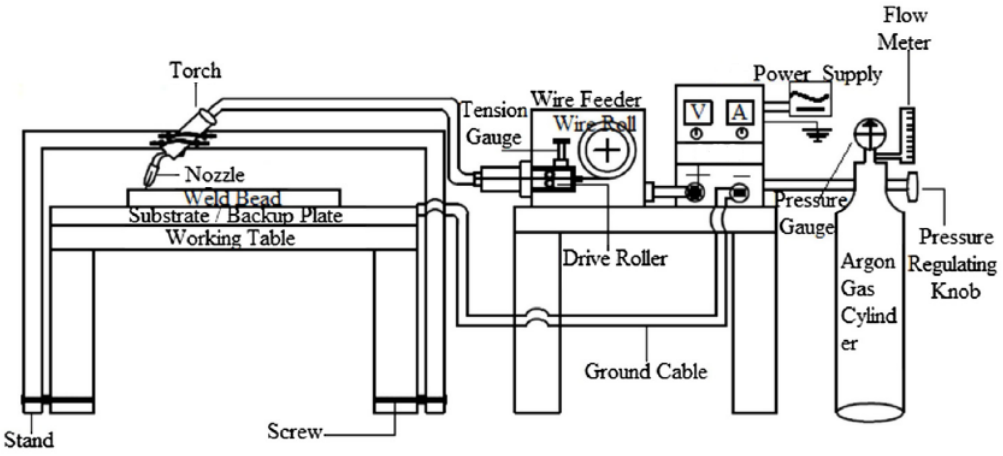

Figure 7. Illustration of GMAW [28].

Globular, short-circuiting, spray and pulsed-spray are variations of GMAW. By altering voltage and current of the arc, desired mode is attained [31]. These different metal transfer modes affect surface quality, microstructure and mechanical properties of deposited parts. Dendritic microstructure consisting of elongated columnar grains are obtained when accumulation is conducted by pulse mode. Short circuit mode yields to a fine microstructure with equiaxed grains [28]. Different types of metal transfers are shown in Figure 8.

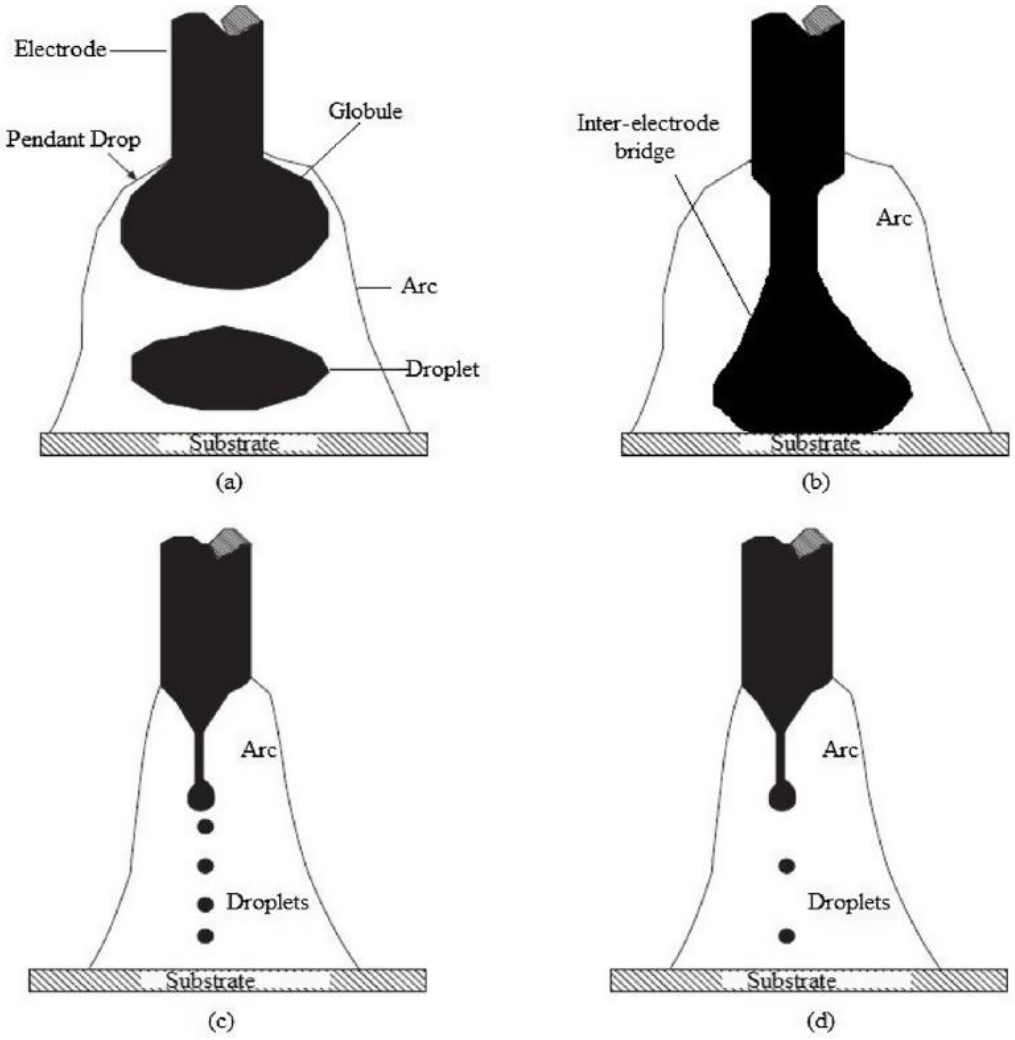

Figure 8. Demonstration of globular (a), short-circuiting (b), spray (c) and pulsed-spray (d) modes of metal transfer [28].

Cold metal transfer (CMT) is an advanced mode which is based on short-circuit GMAW. Dip transfer is controlled by a back-and-forth mechanism of wire in which delivery of single droplets takes place after solidification of former droplet is completed. At the beginning, tip of electrode touches the substrate. As short-circuit occurs, wire is withdrawn and the droplet is disentangled from wire to weld pool. After droplet transfer is completed, arc is formed again and this cycle continues with accumulation of other droplets. Stages of CMT is resembled in Figure 9.

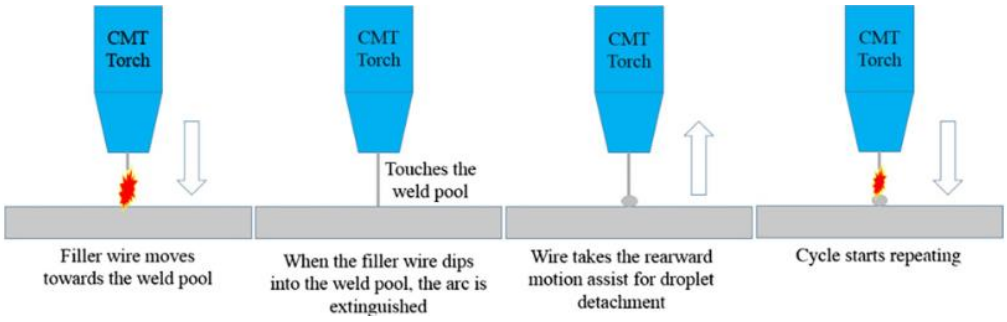

Figure 9. Stages of CMT [32].

Generated arc is steady and spatter-free while heat input is lesser than conventional GMAW. CMT ensures fine beads in terms of desired microstructure and geometry [28, 32, 33].

2.1.3.3.2 Gas Tungsten Arc Welding (GTAW)

GTAW utilizes non-fusible tungsten electrode with direct current straight polarity technique. A shielding gas exists for protection of electrode and melted pool [34]. An independent wire feeding system is present for deposition. GTAW setup is resembled in Figure 10. Since the base is the anode, heat energy only melts weld pool which results in lesser energy efficiency (65%) compared to GMAW. Deposition rate of GTAW is also lower than GMAW (about 2 - 3 times lesser) [28]. Slag and spatter formation are inhibited while obtaining a good finish [35].

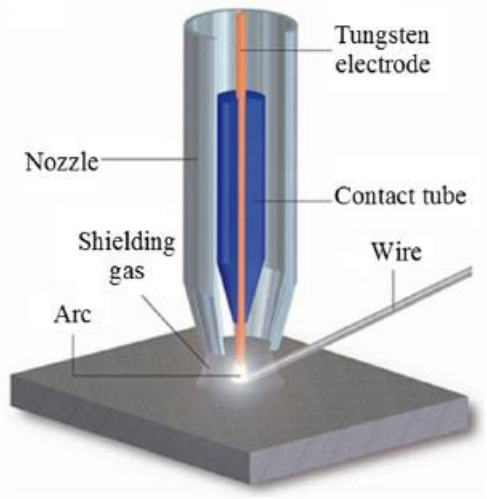

Figure 10. Constituents of GTAW [20].

2.1.3.3.3 Plasma Arc Welding (PAW)

PAW is a development of GTAW with aim of enhancing productivity. Arc is generated between non-fusible tungsten electrode and water-cooled copper nozzle in this process as seen in Figure 11. While flowing through arching zone, ionization of inert gas occurs and plasma jet is formed. Plasma jet is source of energy that creates weld pool into which wire is fed. Apart from plasma gas, another gas is present for shielding of deposited metal. Good quality beads with small amount of distortion are accumulated via PAW. Deposition rate of PAW is between GMAW and GTAW while it has a high capital cost [19, 28].

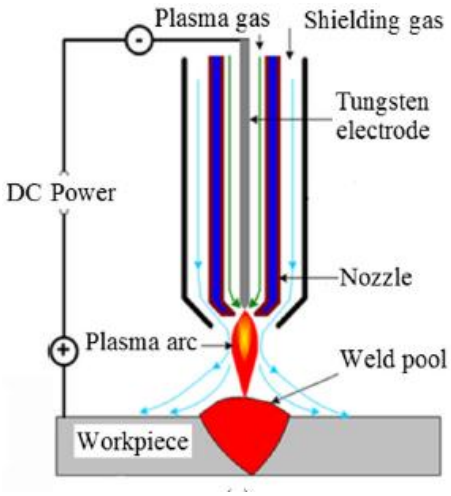

Figure 11. Schematic view of PAW [20].

2.2 The Material; Duplex Stainless Steel

Stainless steels (SS) are divided into five major groups that are austenitic, ferritic, martensitic, duplex and precipitation hardened [36]. As indicated from the names, mainly microstructure of SS determines the classification whereas heat treatment specifies precipitation-hardenable type. A stainless steel involves at least 12wt% Cr [37]. Stability areas of SS according to their ingredient elements are shown on Schaeffler diagram in Figure 12.

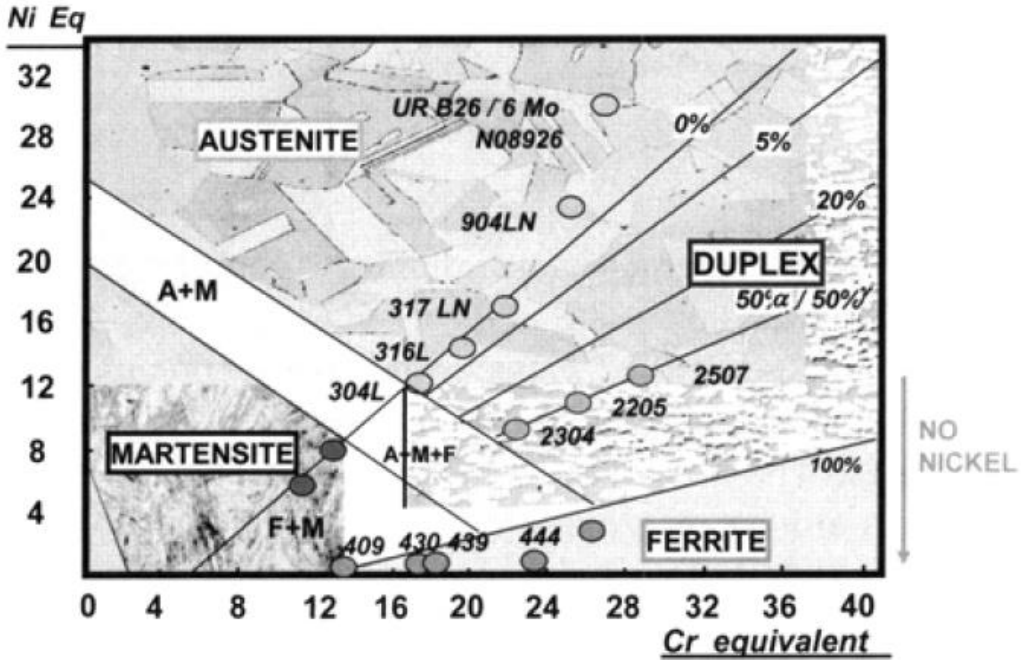

Figure 12. Schaeffler diagram [38].

SS were established at the beginning of 20th century. Primarily, ferritic and martensitic grades consisted of Fe-Cr elements were introduced. Then, austenitic grade composed of Fe-Cr-Ni elements was developed and taken the lead due to accessibility of production and fabrication. In 1933, a grade which had significant ferrite fraction in austenite matrix was found coincidentally due to a fault in melting. Investigations revealed that strength and corrosion resistance of this grade was improved, therefore it drew attention. DSS have various virtues over austenitic and other grades. Two equally proportioned phases which are austenite and delta ferrite exist in DSS. Strength and resistance to local corrosion are promoted by ferrite while ductility and resistance to general corrosion are encouraged by austenite phase. DSS have superior endurance to stress corrosion cracking (SCC) and intergranular corrosion (IGC) which are major concerns in aggressive environments where chloride exists. Hence, DSS are used in several industries like chemical, oil, gas and nuclear in the form of pipeline, vessel or valve owing to favorable combination of mechanical and corrosion properties. Pitting resistance equivalent number (PRE_N) is

a quantity which designates pitting corrosion resistance according to chemical composition of SS. PRE_N is calculated as

$$PRE_N = \%Cr + 3.3 \times (\%Mo) + 16 \times (\%N) \quad (5)$$

As it is seen Cr, Mo and N are the elements that affect PRE_N. For DSS, the value of PRE_N is about 35 whereas PRE_N of super DSS is greater than 40.

2.2.1 Microstructure

The main elements that stabilize ferrite phase are Cr, Mo, Nb and Si. Presence of Cr and Mo expand passive range which leads to creation of oxy-hydroxide films. Due to this incident, endurance to local, pitting and crevice corrosion is enhanced. Nevertheless, amount of these elements is restricted since they provoke intermetallic precipitation like sigma (σ) and chi (χ) phase. On the other side, austenite phase is stabilized by Ni, N and Mn. They compensate ferrite stabilizers to maintain equilibrium. Mainly, Ni satisfies phase balance while N contributes to pitting and crevice corrosion resistance and strength. However, there is a limit of addition, above which phase balance is broken by increasing austenite more in terms of volume fraction. In this case Cr and Mo are enriched in remaining ferrite and if a temperature interval of 650 to 950°C is subjected, intermetallic formation from ferrite occurs. Moreover, excess Ni content results in alpha prime development. In Figure 13, the impact of elements in terms of phase precipitations is given [39].

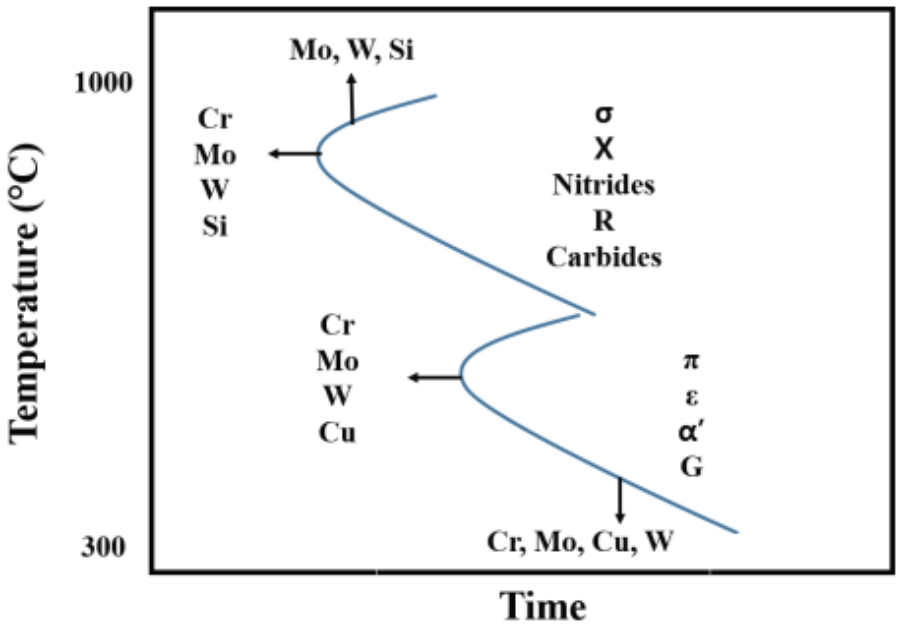

Figure 13. Influence of element addition to formation of several phases [40].

Chemical composition of SS determines obtained phase after solidification. According to Cr_{eq}/Ni_{eq} ratio either formation of ferrite or austenite from liquid phase occurs. According to Schaeffler, Cr_{eq} and Ni_{eq} are calculated as [41]

$$Cr_{eq} = \%Cr + \%Mo + 1.5 \times (\%Si) + 0.5 \times (\%Nb) \quad (6)$$

$$Ni_{eq} = \%Ni + 30 \times (\%C) + 0.5 \times (\%Mn) \quad (7)$$

Five different variations of primary solidifications are shown in Figure 14. Liquid solidifies to completely austenite in (a) while some amount of ferrite also is solidified apart from austenite in (b). In (c) and (d) ferrite is main phase whereas austenite is also present in both, but volume fraction of ferrite is greater in (d). In (e) liquid solidifies completely to ferrite and formation of austenite takes place via solid state transformation [42].

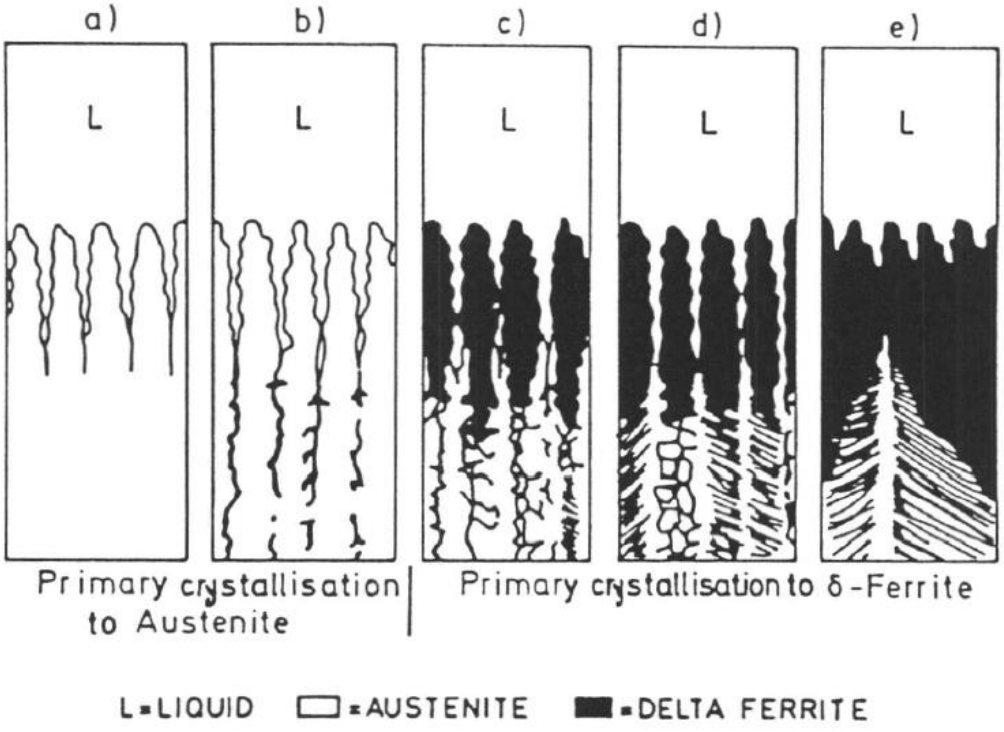

Figure 14. Crystallization variations of SS [42].

Solidification of DSS starts with nucleation of ferrite from liquid. As ferritic solvus temperature is reached and passed, nucleation of austenite begins at grain boundaries of delta ferrite. The sequence could be summarized as liquid transforms to liquid and delta ferrite mixture, then liquid and delta ferrite mixture transforms to delta ferrite and austenite mixture. Ferritic solvus temperature depends on Cr_{eq}/Ni_{eq} ratio as it is seen on Figure 15. Dashed green lines in Figure 15 represents interval for typical DSS. Transformation of delta ferrite to austenite continues approximately down to 450°C.

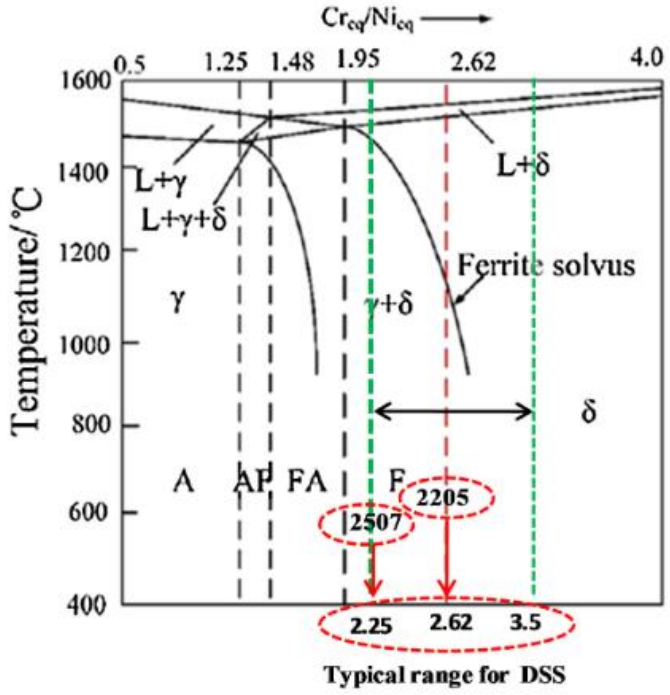

Figure 15. Fe-Cr-Ni phase diagram according to Cr_{eq}/Ni_{eq} ratio [43].

According to temperature, chemical composition of ferrite and austenite change due to different solubility limits of elements. Secondary transformations happen in case of thermal treatment exposure. Elemental partitioning is a driving force for secondary transformations. Elements' diffusion rate is favorable in ferrite phase, therefore majority of secondary transformations occur in this phase. At a temperature interval of 300 to 1000°C (the range could differ for different Cr_{eq}/Ni_{eq} ratios), secondary phases like sigma, chi, Cr-nitrides, alpha prime and secondary austenite could precipitate both at grain boundaries and in ferrite grains. Presence of these secondary phases are hazardous as they affect corrosion resistance and toughness. Sigma is the most critical secondary phase because of its greater volume fraction. It begins to precipitate at grain boundaries of ferrite and extends into the ferrite grains at temperature range of 600 to 1000°C. Elements which provokes sigma precipitation are Cr and Mo. Chi precipitation takes place among 700 and 900°C. Diffusion rate is dropped since this precipitation occurs at lower temperatures and chi requires

greater Mo amount. Due to these facts, chi is lower than sigma in terms of volume fraction. Cr-nitride demands a fast cooling between 700 and 900°C in order to form. As Cr and N are consumed, both localized, pitting and crevice corrosion resistances are depressed. 475°C embrittlement is a term that is used for formation of α and α' phases between 300 and 500°C. Spinodal decomposition of ferrite occurs and Fe rich α and Cr rich α' phases are obtained. In addition, when thermal treatment is applied, secondary austenite could be formed from ferrite. The amount Cr and Mo in secondary austenite is lower than primary austenite which leads to a decrease in pitting corrosion endurance [44]. In Figure 16 summary of phase transformation is resembled.

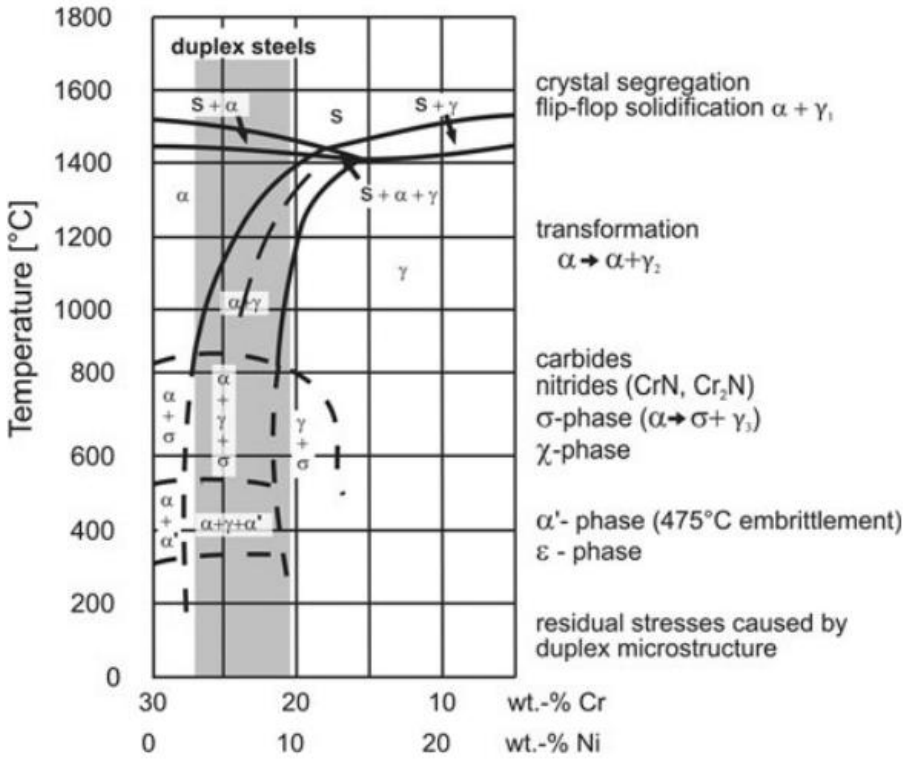

Figure 16. Overview of phase transformation of DSS [41].

2.2.2 Properties

Mechanical properties of DSS are superior in comparison to both austenitic and ferritic grades. In terms of yield strength, DSS is greater about 2 - 3 times than austenitic SS due to presence of ferrite phase. Besides, ferritic SS has also lower strength than DSS. Yield strength is significantly affected by grain size and DSS has a fine microstructure with smaller grains, because growth of grains is restrained for both present phases. In addition, strength of austenite is higher than ferrite since N partitioning takes place in austenite phase. Other than these reasons, presence of secondary austenite and interstitial (N) and substitutional (Cr and Mo) solution hardening have influence in high strength of DSS. Comparison of SS according to their mechanical properties is given in Table 1.

Table 1. Mechanical properties of different stainless steels [45].

Alloy	Standard	0.2% proof stress (min) $M.Nm^{-2}$	Ultimate tensile strength $M.Nm^{-2}$	Elongation (min) A5, %	Impact toughness at RT *J*	Fluctuating tension fatigue strength $M.Nm^{-2}$
AISI 304	UNS S 30400	210	515 - 690	45	>300	120±120
AISI 430	UNS S 43000	205	450	20		
SAF2304	UNS S 32304	400	600 - 820	25	300	245±245
SAF2205	UNS S 31803	450	680 - 880	25	250	285±285
SAF2507	UNS S 32750	550	800 - 1000	25	230	300±300

Toughness is gained by existence of austenite phase in DSS. Cleavage fracture of ferrite is suppressed by austenite that has ductility. Nevertheless, an increase in addition of alloying elements causes a decrease in toughness. Above elevated temperatures ferrite is decomposed and hazardous phases are precipitated, thus mechanical properties begin to collapse. Moreover, DSS has a ductile to brittle transition temperature because of ferrite existence. Fatigue strength of DSS is also higher than other grades. Since they have higher yield strength, amount of plastic deformation required to initiate a crack is greater [38, 40, 44, 45].

2.2.3 WAAM DSS

Because of layer-by-layer structure, multiple thermal cycles exist in case of WAAM DSS. When a layer is deposited to bulk, adjacent layers are influenced since temperature increases. This increase in temperature leads to formation of secondary phases such as sigma, chi, secondary austenite, etc. Due to this circumstance, microstructure and eventually mechanical properties are affected. Major parameters which influence microstructure are heat input and interlayer temperature. Therefore, optimization have to be conducted for desired properties. In reheated layers, austenite growth and formation of secondary austenite are obtained [46]. Ferrite and austenite are promoted by rapid and slow cooling respectively. When greater heat input is used, austenite phase becomes dominant and hazardous secondary phases are formed. Low interlayer temperature results in higher ferrite content [6]. Additionally, utilized shielding gas has also a great impact on properties. Most of the used shielding gases consist of primarily argon gas which has highest percentage in mixture. Commonly additions to argon are oxygen, carbon dioxide, nitrogen, helium, etc.

2.3 The Property; Fracture Mechanics and Fracture Toughness

Fracture stress observed for metals is much lower than theoretical cohesive stress due to flaws or cracks exist in structure. Different mechanisms could generate microcracks in a metal and occurrence of a stress could propagate this microcrack to a complete fracture. Energy transfer rate of elastic stress field to inelastic propagation of crack is called as strain-energy release rate. Fracture toughness is the critical value of strain-energy release rate that resulted extension of crack to fracture. Fracture mechanics is utilized for specifying whether length of a crack present in a metal is detrimental for crack extension which results in fracture. In order to characterize fracture parameter, which represents fracture toughness of a metal, deformation characteristic is taken into consideration [47]. Broadly fracture behavior is divided into two that are brittle and ductile fracture.

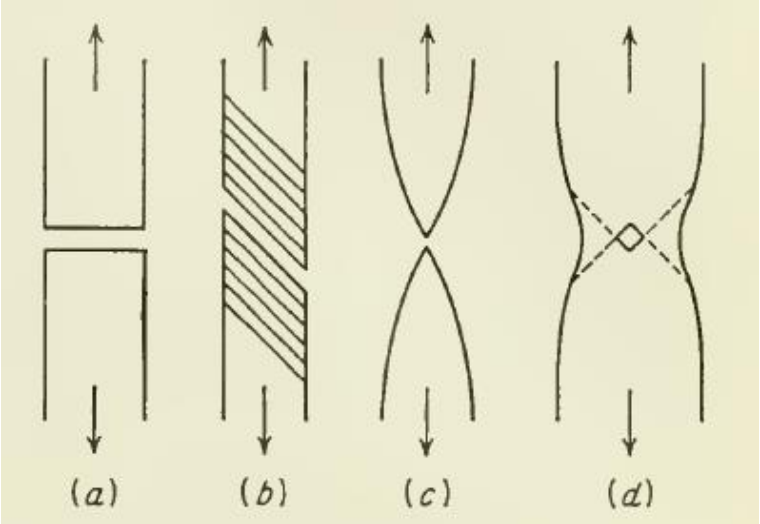

Figure 17. Fracture types observed in metals subjected to uniaxial tension; (a) brittle fracture of single crystals and polycrystals, (b) shearing fracture in ductile single crystals, (c) completely ductile fracture in polycrystals and (d) ductile fracture in polycrystals [47].

In case of brittle fracture rapid and unstable crack growth exists. This type of fracture has a certain crack initiation point and a rapid decrease in loading is observed while testing. Crack tip is controlled by linear elastic deformation's annular zone and below crack initiation, little amount of crack growth exists for fracture resistance. On the other hand, slow and stable crack growth is present in ductile fracture. More energy is absorbed since crack propagation consists of growth and coalescence of micro ductile voids. Apart from a single point, a continuous duration of ductile tearing is monitored in ductile type of fracture, therefore a resistance curve is required. Because of strain hardening, crack growth could happen under accelerating load situation. This circumstance makes determination of fracture point unclear in terms of resistance curve attitude. In order to define ductile fracture, resistance curve could be utilized. Toughness of a single point value is necessity for structural integrity evaluation. Definition of a single point ductile fracture toughness value is near the onset of stable crack tearing. This single point value could be found out near the transition from initial crack blunting to crack tearing in a resistance curve. Moreover, slope of the resistance curve could also be utilized for designating the single point value whereas it is the significant change in the slope. This phenomenon is denominated as fracture initiation toughness. In fracture mechanics, most significant parameters that used are stress intensity factor (*K*), elastic energy release rate (*G*), *J*-integral and crack tip opening displacement (CTOD) [14]. Fracture mechanics are divided according to plasticity of crack tip. Linear elastic fracture mechanics (LEFM) is generally represented by *G* and *K* which clarifies elastic crack-tip fields' intensity. This phenomenon is suitable for materials which have low ductility. The energy state for fracture was first introduced by Griffith. Later current approach was developed by Irwin. The energy release rate (*G*) of a metal that is infinitely wide and has a *2a* crack size under tension force is calculated by

$$G = \frac{\pi \sigma^2 a}{E} \tag{8}$$

where

σ is applied stress, a is half crack size and E is Young's modulus.

Stress intensity factor (K) is another phenomenon utilized for linear elastic conditions. Displacement near the crack tip, stress and strain are investigated in the context of K. It is calculated by

$$K_{(I,II,III)} = Y\sigma\sqrt{\pi a} \tag{9}$$

where

Y dimensionless constant, σ is applied stress and a is half crack size. In addition, notations of *I*, *II* and *III* represent the mode of loading which illustrated in Figure 18 [48]. Mode I is utilized for most fracture toughness tests with a notation of K_{IC} which is called plain-strain fracture toughness.

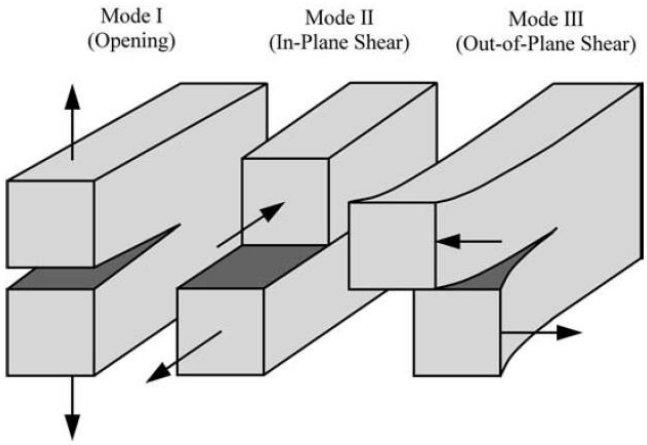

Figure 18. Three types of loading modes [48].

Elastic plastic fracture mechanics (EPFM) is generally denoted by *J*-integral and CTOD that qualify elastic plastic crack-tip fields' intensity. The interest of elastic plastic fracture mechanics includes both small- and large-scale plasticity [13]. For metals with high toughness and low strength this phenomenon is operative. CTOD which is the measure of fracture toughness in terms of crack tip opening was

introduced by Wells. The notation used for CTOD is δ. The crack which was sharp previously becomes blunted due to plastic deformation and as toughness increases the amount of crack blunting also increases in this type of fracture mechanics. According to Rice description of CTOD is the displacement where crack edge encounters with sides of the crack and the angle between two interceptions is 90° as demonstrated in Figure 19.

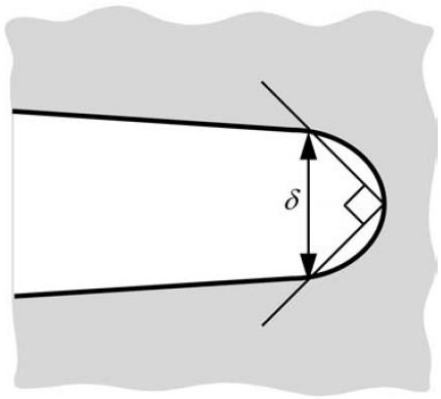

Figure 19. Definition of CTOD [48].

CTOD is calculated with respect to modified hinge model as

$$\delta = \delta_{el} + \delta_p = \frac{K_I^2}{m\sigma_{YS}E'} + \frac{r_p(W-a)V_p}{r_p(W-a)+a} \tag{10}$$

where

K_I is stress intensity factor for Mode I, m is dimensionless constant, σ_{YS} is the 0.2% offset yield stress, E' is Young's modulus for plain strain condition, r_p is plastic rotation factor, W is specimen width, a is crack length, V_p is plastic displacement at the crack mouth. Rice introduced the nonlinear energy release rate J by considering elastic plastic fracture as nonlinear elastic. In nonlinear metals, crack tip stresses and strains are qualified by J which is a path independent integral. If a surrounding path,

which is counterclockwise, around the crack tip exists as seen in Figure 20 J is calculated as

$$J = \int_{\Gamma} (wdy - T_i \frac{\partial u_i}{\partial x} \, ds) \tag{11}$$

where

w is density of strain energy, T_i is traction vector's components, u_i is displacement vector components and ds is length increment along the contour Γ.

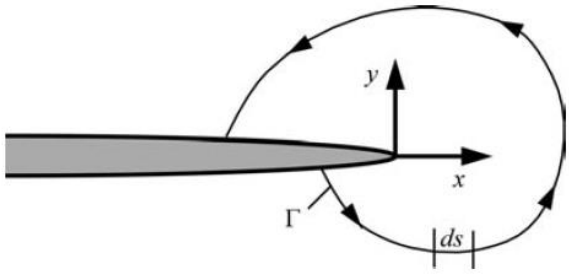

Figure 20. Path which surrounds crack tip [48].

Specifying J via integral of path that rounds the crack is not applicable due to challenge in numerical analysis. Therefore, J is determined under favor of energy release rate definement. The formula where J is stated as the energy absorbed over cross sectional area is

$$J = \frac{\eta U_c}{Bb} \tag{12}$$

where

η is dimensionless constant, U is strain energy, B is specimen thickness and b is crack remaining ligament. During crack extension absorbed energy is not regained due to permanent deformation, therefore energy difference of adjacent cracks defines J [48]. Resistance curves are plotted as fracture toughness value versus crack extension

(Δa) in the vertical axis and in the horizontal axis respectively [49]. For elastic metals, energy required for unit crack extension is constant. On the other hand, for metals, which have tendency for elastic plastic deformation, as crack grows the required energy is increasing gradually. The reason for this circumstance is increase in plastic zone as crack grows [50]. Crack extension behaviors of three particular stages are seen in Figure 21.

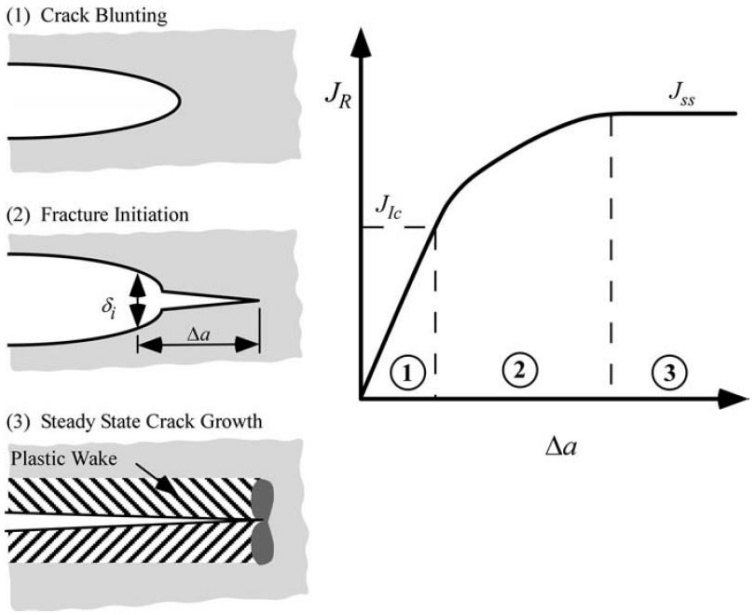

Figure 21. Different crack extension stages [48].

In first stage, a stationary crack is observed. Due to crack blunting, slope is finite. In second stage, crack extension is started. Stresses and strains at the crack tip are affected by crack blunting from the first stage at the very beginning of crack extension. The final stage is called stationary state where stresses and strains are liberated from crack blunting. A plastic wake is generated as crack extends in steady state [48]. When increase rate of crack length's driving force overcomes increase rate of resistance to crack extension, crack growth becomes unsteady [13]. Duplex stainless steels are utilized in structures of oil and gas industry for many decades

since they have two significant benefits that are being corrosion resistant and having enhanced mechanical properties. Nevertheless, unexpected or excessive loads could be present in-service conditions which may lead to catastrophic failure. Thus, consequences of crack like defects, which may be hazardous for structural integrity, have to be investigated in the aspect of fracture mechanics. Austenite phase which is gained with a slower cooling rate promotes an increase in toughness. Austenite which is more ductile restrains ferrite's cleavage fracture [45]. Moreover, multiple passes during process also raise toughness value as a result of austenite promotion [39]. Nevertheless, ferrite-austenite ratio could be altered due to exposure of instantaneous heating and cooling. Complicated thermal cycles or overmuch heat input may bring brittle secondary phases such as sigma, chi, intermetallics, etc which have an unfavorable impact on toughness. Eventually, usage of fracture mechanics in terms of fracture toughness testing is a necessity in order to assign failure characteristic.

CHAPTER 3

EXPERIMENTAL STUDIES

3.1 Methodology

Experimental studies chapter begins with reference parent metal and filler material which was used for wire arc additive manufacturing. The metals are introduced in terms of technical standards. Fabrication process is explained with measured and calculated welding parameters. Later integrity confirmation is addressed which includes testing and evaluation methods. Characterization of parent metal and wire arc additive manufactured metals are presented from the point of microstructure in following section. Then, mechanical characterization is described in terms of tensile and fracture toughness testing. This section is the primary issue of the thesis which describes resistance properties for both parent metal and wire arc additive manufactured metals. Post-test metallography and fractography are followed in order to validate fracture toughness tests. Reference standards of experimental investigation techniques are tabulated in Table 2.

Table 2. Comprehensive review of experimental investigations with respect to reference standards.

	Specimen Designation	Reference Standards
Integrity confirmation	RT	ASTM E1742, ASTM E2007 & ISO 5817
	PT	ASTM E165
Microstructural constituents	OM	
	XRD	NBS Standard XRD Patterns & ASTM E82
	EDX	ASTM E1508
	HV 0.5	ASTM E384
Strength		ASTM E8 & ISO 6892-1
Fracture toughness	*J*	BS 8571, ISO 12135 & ISO 15653
Post-test metallography	SEM	ASTM E766

3.2 Parent Metal and Wire Arc Additive Manufacturing Filler

Wire arc additive manufactured blocks of DSS grade 2509 was analogized with wrought DSS grade 2507. The parent metal had a thickness of 14 mm. The plate which was conformed to ASTM A240 S32750 was delivered from ArcelorMittal.

Grade 2507 duplex stainless steel wrought plate was also used as the substrate for wire arc additive manufacturing. The substrate had dimensions of 150 mm and 20 mm in terms of length and width.

1.2 mm diameter filler wire which conforms ISO 14343-A G 25 9 4 NL and SFA/AWS 5.9 ER2594 was utilized to manufacture the blocks of grade 2509.

Major alloying element constituents of parent metal and wire arc additive manufactured blocks were shown in Table 6. Additionally, oxygen and nitrogen

amounts of coupons, which were built under $Ar+O_2$ and $Ar+N_2$ shielding gases, were determined by inert gas fusion technique according to ASTM E1019 [51].

3.3 Process

Substrate was located at flat position and aligned on the platform manually and clamped by the help of pneumatic cylinders. After clamping, the mechanized torch was driven along the substrate. Schematic WAAM setup could be seen in Figure 22.

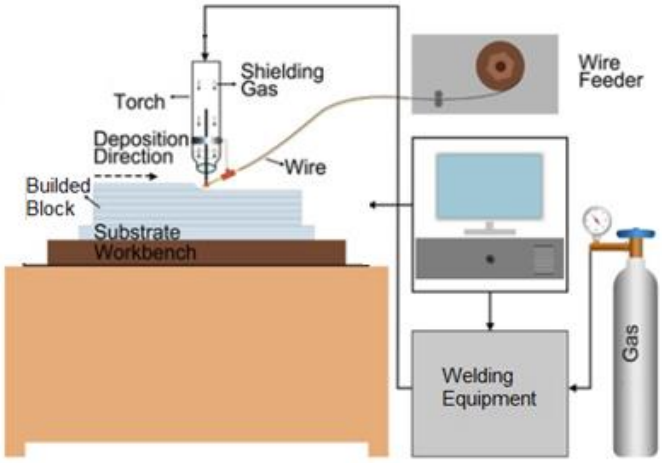

Figure 22. Schematic representation of WAAM setup [52].

In order to manufacture blocks, GMAW was used in short/spray transition zone. By virtue of optimum heat input; reduction in terms of thermal input, distortions and residual stresses are acquired. For both blocks between substrate and wire electrode, a reversed polarity direct current were utilized where substrate is cathode and electrode is anode. Shielding gas was applied during the operation in order to protect the weld pool from atmospheric contamination. Welding parameters carried out during manufacturing was stated in Table 3. Except shielding gas, all parameters were kept constant.

A section of block which was manufactured via $Ar+O_2$ was subjected to solutionizing. It was solutionized at 1100°C for 1 hour and water quenched.

As manufacturing and post processes were completed, three different WAAM coupons were obtained. These three coupons were consisted of $Ar+O_2$ as build, $Ar+O_2$ solutionized and $Ar+N_2$ as build which were compared with reference parent metal later.

Table 3. Utilized welding parameters during WAAM.

			Grade 2509
Independent variables / parameters	**Wire-arc potential**	V	21
	Wire feeding speed	$m.min^{-1}$	4.7
	Stand of distance	mm	12
	Linear welding speed	$mm.s^{-1}$	7
	Interlayer temperature	°C	200
	Shielding gas		$Ar + 2\%O_2$ / $Ar + 2\%N_2$
	Flow rate of shielding gas	$L.min^{-1}$	14 - 18
	Heat transfer coefficient	$W.m^{-1}.K^{-1}$	Stated in Figure 54
Dependent variable / parameters	**Wire-arc current**	A	180
	Line energy	$kJ.mm^{-1}$	0.54

3.4 Integrity Confirmation

Integrity assessment of manufactured blocks were conducted via non-destructive testing (NDT). Macro examination, liquid penetrant and radiographic examination were conducted. In order to promote visual inspection and investigate surface discontinuities, liquid penetrant tests were carried out. Radiographic investigation according to ASTM E1742 [53] was implemented for affirmation of deposited beams' integrity. Due to better image quality and efficient process time, behalf of traditional radiographic films, digital radiography was used for X-ray inspection. Evaluation of films were executed in compliance with ISO 5817 [54].

3.5 Microstructural Characterization

For microstructural characterization three methods which are metallography, X-ray diffraction (XRD) and energy dispersive X-ray spectroscopy (EDX) were used.

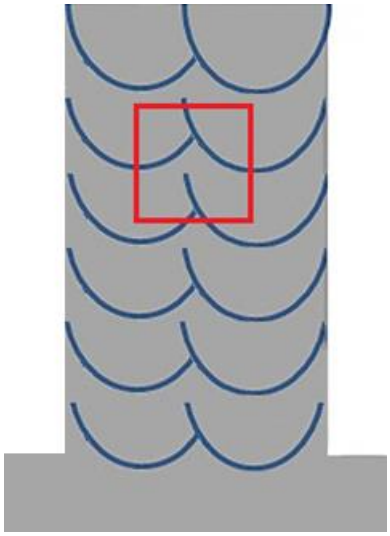

Figure 23. Location of microstructure specimens extracted from coupons of WAAM.

One face of the segmented parent metal, which is parallel to rolling direction, was subjected to metallography. Wire arc additive manufactured blocks' extracted segments, which were transverse to welding direction as seen in Figure 23, were also investigated in terms of metallography.

Employed etchants for microstructural characterization are stated in Table 4.

Table 4. Employed etchants for microstructural characterization.

Etchant	**Composition**	**Procedure**	**Purpose**
Modified Beraha	1.5 g $K_2S_2O_5$ 30 mL HCl 60 mL H_2O	etching at RT	to reveal δ and γ
Aqua Regia	45 mL HCl 15 mL HNO_3 20 mL ethanol	etching at RT	
Oxalic Acid	7 g $C_2H_2O_4$ 100 mL H_2O	4 V 10 sec	to reveal secondary phases
Marble	4 g $CuSO_4$ 20 mL HCl 20 mL H_2O	etching at RT	to reveal secondary phases

For metallographic examination all specimens were subjected to grinding, polishing and etching respectively. Firstly, specimens were grinded via SiC emery papers from coarser grade to finer grade. Then, polishing was applied to specimens using 3 and 1 μm Diamond colloidal respectively. Finally, etching was implemented with Modified Beraha at room temperature in order to reveal δ and γ phases. For revealing secondary phases electrochemical etching with Oxalic Acid and Marble was

performed. Later specimens were cleaned via alcohol in order to eliminate etchant from the surface completely.

Optical microscope (OM) was utilized for examination of the specimens. Volume fraction of phases were measured by manual point count and by image analysis software according to ASTM E562 [55] and ASTM E1245 [56] respectively under OM.

X-ray diffraction was applied to specimens via Cu radiation at 2θ range from 30° to 110° with $2°min^{-1}$ scanning rate.

EDX which attached to SEM was utilized in order to investigate Cr, Ni and Mo concentrations in δ and γ. EDX analysis was performed according to ASTM E1508 [57].

Micro hardness investigation was performed to the specimens of parent metal and wire arc additive manufactured blocks. According to ASTM E384 [58] 4.9 N (HV0.5) load was applied to the surfaces which were transverse to welding direction. An interspacing distance of 0.3 mm was used and the load was implemented for 10 seconds. Size of the of area, which were subjected to micro hardness, covers multiple zones and beads, as seen in Figure 24.

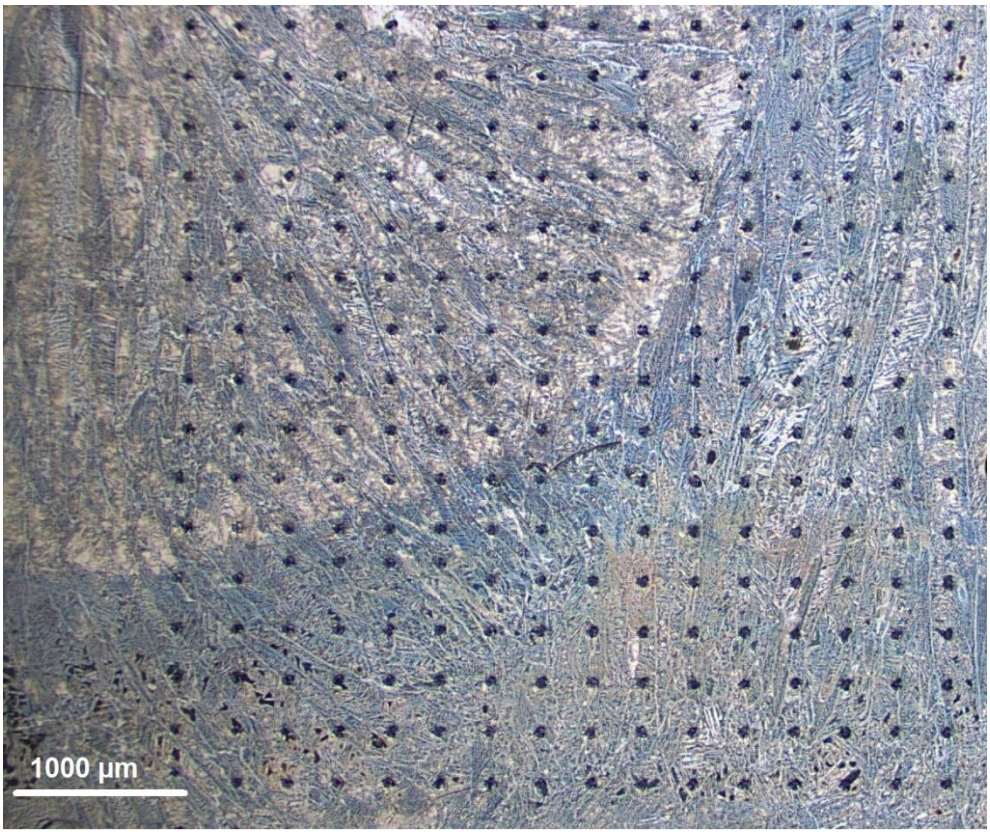

Figure 24. View of HV0.5 indentations with an interspacing distance of 0.3 mm.

3.6 Mechanical Characterization

According to ASTM E8/E8M [59] and ISO 6892-1 [60] tensile test was applied to the specimens of parent metal and wire arc additive manufactured blocks. The specimens which had circumferential cross section were tested. Reduced section's diameter was 6 mm and gauge length was five times the diameter. Basic view of the specimens is given in Figure 25.

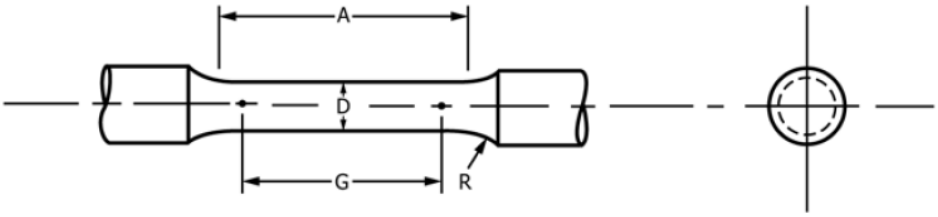

Figure 25. Geometry of tensile test specimens [59].

For wire arc additive manufactured blocks samples were extracted transverse to welding direction, as seen in Figure 26.

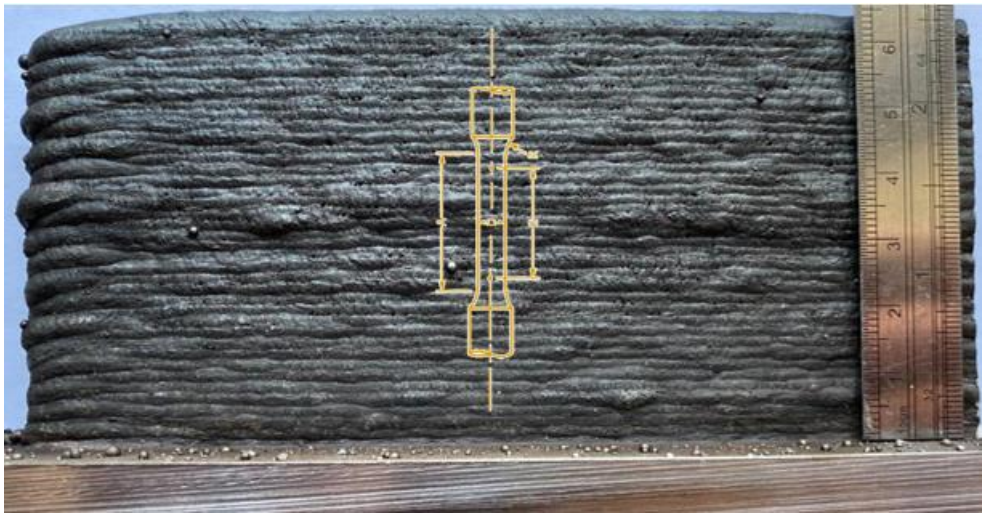

Figure 26. Extraction orientation of tensile test specimen.

For parent metal samples were extracted transverse to rolling direction. Tensile tests were implemented at room temperature (23°C ± 5°C) by an electromechanical universal tensile testing machine (BESMAK BMT-E 200 kN). Up to the yielding strength a test speed of 0.6 mm/min was utilized and after yielding the speed was set to 5 mm/min.

3.7 Fracture Toughness Tests

For obtaining single point fracture toughness values at -10°C temperature, single edge notch bending (SENB) and single edge notch tension (SENT) specimens of parent metal and wire arc additive manufactured blocks were tested up to maximum crack extensions according to ISO 12135 and BS 8571 respectively [61, 62]. The parameter of *J* was selected in order to determine elasto-plastic fracture toughness values for both SENB and SENT specimens. Specimens which had notched and fatigue pre-cracked were utilized. Force versus crack mouth opening displacement (CMOD) curve was recorded as test progressed.

For SENB specimens, bend specimen type was selected among all configurations according to ISO 12135 [61]. There are two types of SENT specimens available in the BS 8571 [62], one of them is clamped and the other one is directly pin-loaded. As clamped specimens are coherent with testing unit, which is available in laboratory, it was chosen. The crack plane orientations for both parent and wire arc additive manufactured metals are represented in Figure 27. First letter stands for the normal to the crack plane and second letter stands for expected direction of crack propagation. For the parent metal, indication of "1" shows the rolling direction. For the wire arc additive manufactured blocks, the direction of N is normal to weld, the direction of P is parallel to weld and the direction of Q is weld thickness.

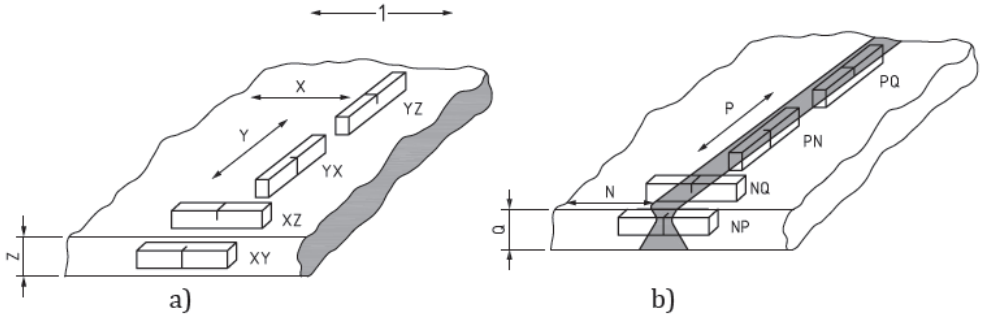

Figure 27. Orientation of crack plane for parent and weld metal [62].

Width (W) over thickness (B) ratio has three alternatives as 0.5, 1 and 2 for SENT specimens. For SENB specimens this ratio could vary from 1 to 4. For both parent metal and wire arc additive manufactured blocks, specimens W over B ratio was selected as 1 since this ratio is appropriate for all types of orientations.

Parent metal's plate had a thickness of 14 mm roughly. From the point of length and width, the plate had exceedingly large dimensions. The thickness of plate was reduced to 12 mm in order to obtain a straight specimen throughout the complete length and with respect to this thickness value other dimensions were machined as seen in Figure 28. YX orientation was preferred in order to simulate worst case, since extension of crack parallel to rolling direction is favored for fracture. As grain boundaries are weakened or embrittled by impurity segregation, oxidation, etc. they are hazardous areas and the resistance behavior of this grade was analyzed as crack propagated along the grain boundaries.

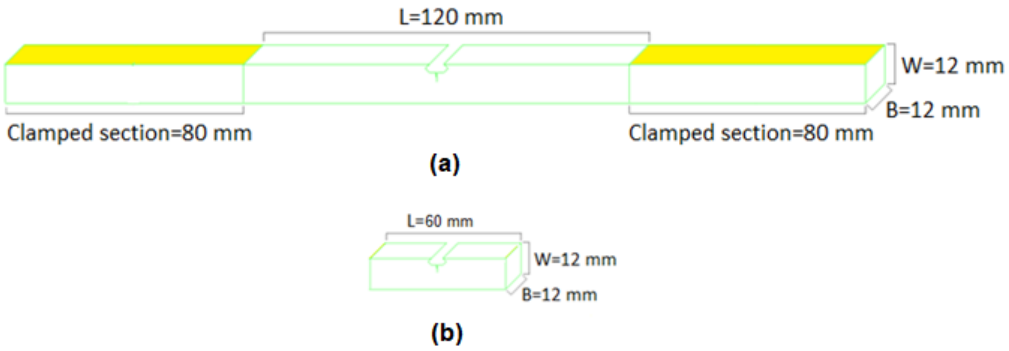

Figure 28. The geometry and dimensions of (a) SENT specimen and (b) SENB specimen.

Wire arc additive manufactured blocks had a thickness of 13 mm roughly. Its thicknesses were reduced to 12 mm and according to this value other dimensions were machined as for parent metal. For wire arc additive manufactured blocks, the

orientation QN was preferred. The orientation of extracted specimens is given Figure 29.

Figure 29. Orientation of fracture toughness specimens of WAAM coupons.

The aim behind this preference was determining most detrimental local area and analyzing the resistance behavior of that specific area by propagating the crack at that zone. The possible problematic local areas are center of the bead and fusion line between the beads. In order to establish this local zone, specimens from different regions of structure, were extracted as seen in Figure 30. In Figure 30, both notch and fatigue pre-crack are represented and at the end of this line, the crack propagation was started. Notch positions were placed and fatigue pre-cracks were introduced at those specific zones. For each region, fracture toughness values were compared.

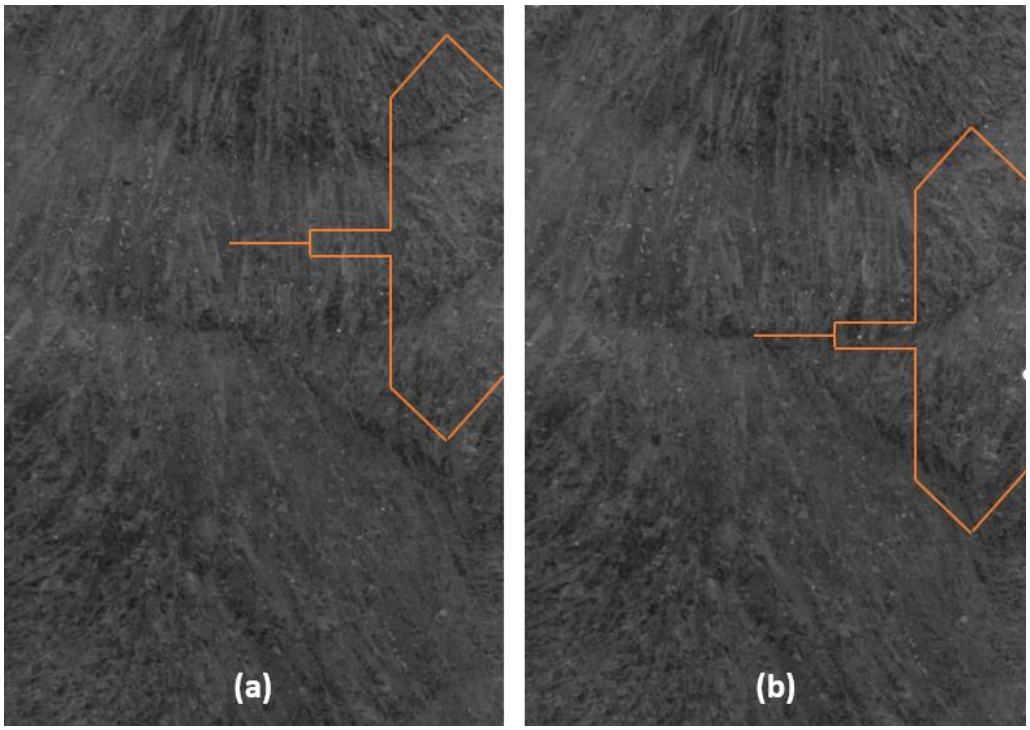

Figure 30. Notch positions of most failing areas with regard to retain stable crack extension; (a) bead centerline (BCL), (b) fusion line (FL).

Notches were introduced with electrical discharge machining (EDM). From the tip of the notch a fatigue pre-crack was initiated and propagated via applying bending forces as seen in Figure 31.

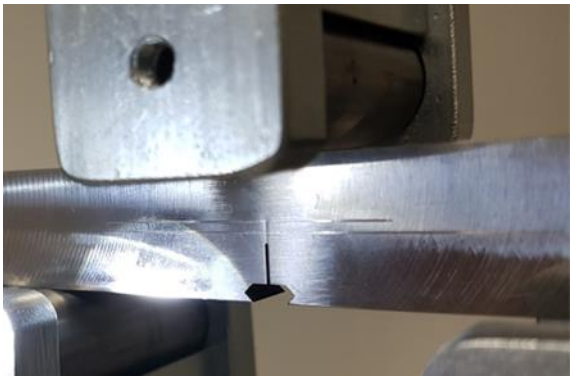

Figure 31. Fatigue pre-cracking.

An MTS servo-hydraulic testing unit was utilized. Fatigue pre-cracking was carried out in accordance with ISO 12135 [61] and ISO 15653 [63] for the parent metal and for the wire arc additive manufactured blocks respectively. The total length of notch and fatigue pre-crack to specimen width ratio for SENB and SENT have to be in the range of $0.45 \leq a_0/W \leq 0.70$ and $0.3 \leq a_0/W \leq 0.5$ respectively. Therefore, this ratio was arranged so that both requirements were satisfied. Notch and fatigue pre-crack geometry is shown in Figure 32.

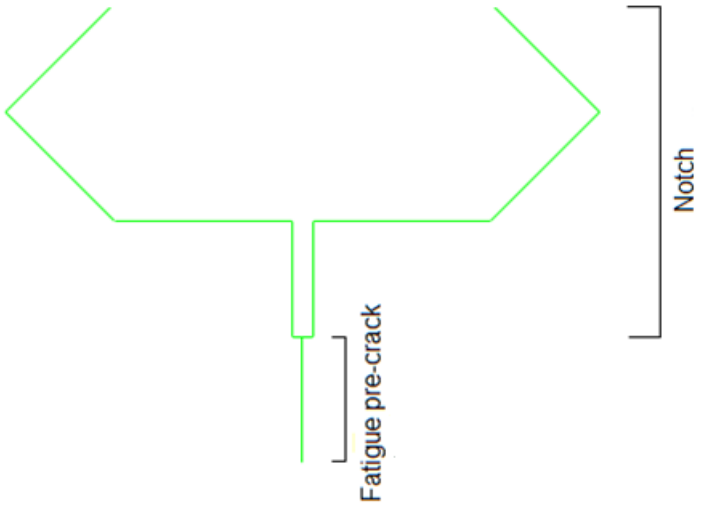

Figure 32. Notch and fatigue pre-crack geometry.

Maximum fatigue pre-cracking force during 50% of total pre-crack extension shall be the lower between below two formulas;

$$F_f = 0.8 \frac{B(W - a_0)^2}{S} R_{p0.2} \quad (13)$$

$$F_f = \xi E \frac{(W \times B \times B_N)^{0.5}}{g_1\left(\frac{a_0}{W}\right)} \frac{W}{S} \frac{(R_{p0.2})_p}{(R_{p0.2})_t} \quad (14)$$

where

$\xi = 1.6 \times 10^{-4} m^{1/2}$

$(R_{p0.2})_p$ is the yield strength at pre-cracking temperature

$(R_{p0.2})_t$ is the yield strength at test temperature

$$g_1\left(\frac{a_0}{W}\right) = \frac{3\left(\frac{a_0}{W}\right)^{0.5}\left[1.99 - \frac{a_0}{W}\left(1 - \frac{a_0}{W}\right)\left(2.15 - \frac{3.93a_0}{W} + \frac{2.7{a_0}^2}{W^2}\right)\right]}{2\left(1 + \frac{2a_0}{W}\right)\left(1 - \frac{a_0}{W}\right)^{1.5}} \quad (15)$$

4000 N was calculated as the lowest force among two formulas. Minimum to maximum force ratio was selected as 0.1, therefore specimens were pre-cracked under a mean force of 2200 N and with amplitude of 1800 N under compression-compression loading. Loading frequency was set as 34 Hz and required fatigue pre-crack was obtained between 80000 and 100000 cycles.

As pre-test operations were completed, specimens were ready for testing. A servo-hydraulic testing unit BESMAK BMT-S 1000 kN and BESMAK BMT-E 200 kN were employed for SENT and SENB tests respectively. Test temperature was set as -10°C since usage area of the duplex stainless steel is offshore environment and through the service life minimum temperature is expected to be approximately this value. Cooling pads were attached to test specimen in order to satisfy required temperature for SENT specimens. The cooling pads were connected to a chiller and cooled alcohol was passing through the pipes continuously. SENB tests were conducted in a pool filled with alcohol and fed with dry ice instantaneously for satisfying test temperature. Thermocouples were attached near the crack tip of specimens for verifying temperature accuracy of ±2°C. After reaching intended temperature, a soaking time of 15 minutes were applied in order to stabilize the environment within complete specimen. A clip-on-gauge was introduced before test

had started. Test setup is shown in Figure 33 and for SENT and SENB specimens respectively.

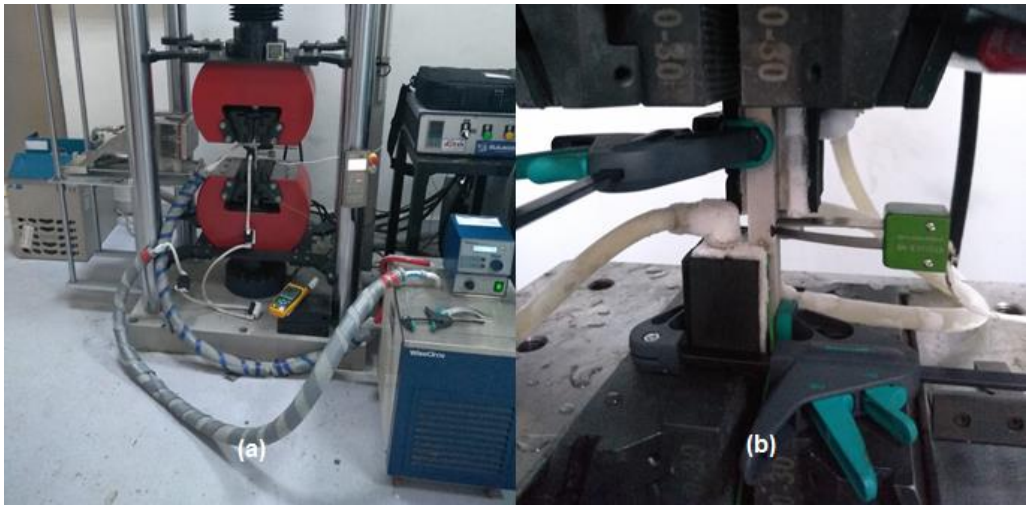

Figure 33. (a) SENT test setup and (b) specimen with attached cooling pads and clip-on-gauge.

Figure 34. SENB test setup and specimen with attached clip-on-gauge.

Under crosshead-displacement control, tests were performed. Loading was arranged such that within the elastic region, stress intensity rate was 0.35 $MPa.m^{0.5}.s^{-1}$ which was suitable for both SENB and SENT. As test was proceeded force versus CMOD curve was obtained as seen in Figure 35.

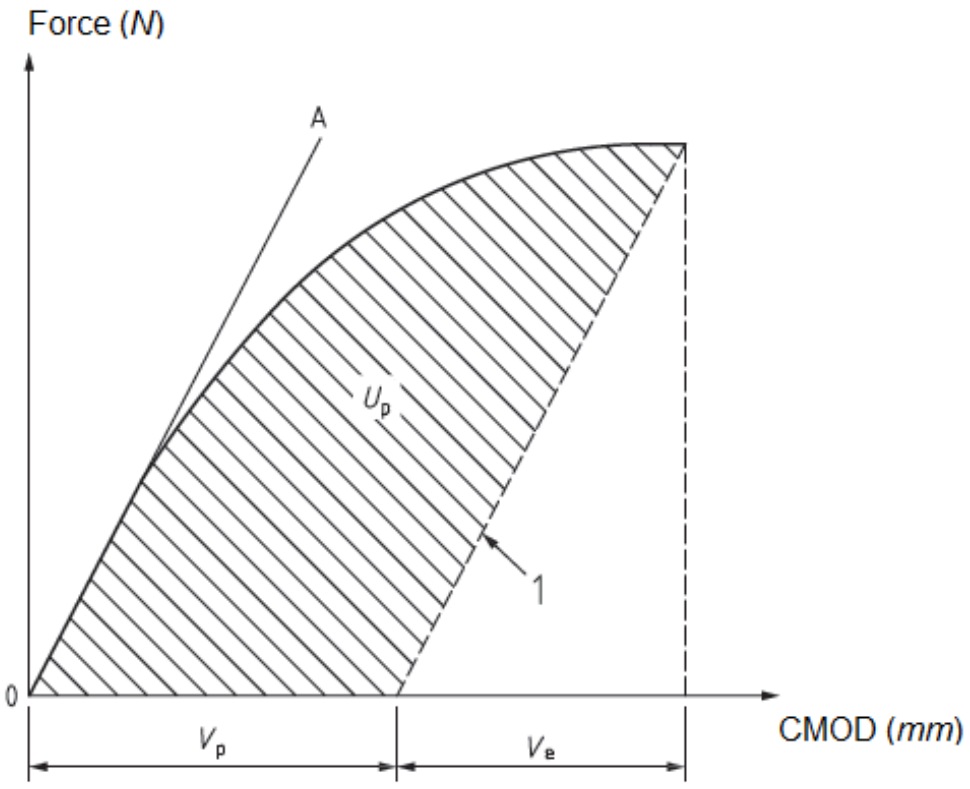

Figure 35. A typical force vs CMOD curve [62].

SENB specimens were loaded up to onset of unstable crack extension and *J* was calculated according to below formulation;

$$J = \left[\frac{FS}{(BB_N)^{0.5}W^{1.5}}\, g_1\left(\frac{a_0}{W}\right)\right]^2 \frac{1-v^2}{E} + \frac{1.9U_p}{B_N(W-a_0)}\left[1-\frac{\Delta a}{2(W-a_0}\right] \qquad (16)$$

where

F is highest force of the force versus CMOD curve

S is bending span

B is specimen thickness

W is specimen width

$$g_1\left(\frac{a_0}{W}\right) = \frac{3\left(\frac{a_0}{W}\right)^{0.5}\left[1.99 - \frac{a_0}{W}\left(1 - \frac{a_0}{W}\right)\left(2.15 - \frac{3.93a_0}{W} + \frac{2.7{a_0}^2}{W^2}\right)\right]}{2\left(1 + \frac{2a_0}{W}\right)\left(1 - \frac{a_0}{W}\right)^{1.5}} \quad (17)$$

v is Poisson's ratio

E is modulus of elasticity

U_p is the area under plastic part of load versus CMOD curve shown in Figure 35

a_0 is initial crack length

For SENT, specimens were also loaded up to onset of unstable crack extension. J was calculated according to below formulations;

$$J = \frac{K^2}{E'} + \frac{\eta_p U_p}{B b_0} \quad (18)$$

where

$$K = \left[\frac{P\sqrt{\pi a_0}}{(BB_N)^{0.5}W}\right] G\left(\frac{a_0}{W}\right) \quad (19)$$

$$G\left(\frac{a_0}{W}\right) = \sum_{i=1}^{12} t_i \left(\frac{a_0}{W}\right)^{\dot{\imath}-1} \quad (20)$$

$$\eta_p = \sum_{i=0}^{10} \varphi_i \left(\frac{a_0}{W}\right)^i \quad (21)$$

Table 5. Constants used in calculations [62].

i	t_i	φ_i
0		1.000
1	1.197	-1.089
2	-2.133	9.519
3	23.886	-48.572
4	-69.051	109.225
5	100.462	-73.116
6	-41.397	-77.984
7	-36.137	38.487
8	51.215	101.401
9	-6.607	43.306
10	-52.322	-110.770
11	18.574	
12	19.465	

Post-test measurements were taken place in order to calculate initial crack length (a_0) and stable crack extension (Δa). After test was completed, heat tint was applied to create a contrast difference. Then, specimens were put into dry ice. The reason of this was transforming specimens to brittle zone and obtaining a flat and clear fracture

surface. For post-metallography and fractography specimens, post fatigue cracking were applied in order to obtain fracture surface. According to ISO 12135 [61], measurements were hold. Initial crack length (a_0) was measured to the tip of the fatigue crack and final crack length (a_f) was measured to the final crack front both from 9 points as shown in Figure 36. Nine measurements were put in below equation;

$$a = \frac{1}{8}\left[\left(\frac{a_1+a_9}{2}\right) + \sum_{j=2}^{j=8} a_j\right] \quad (22)$$

and stable crack extension was calculated from following equation;

$$\Delta a = a_f - a_0 \quad (23)$$

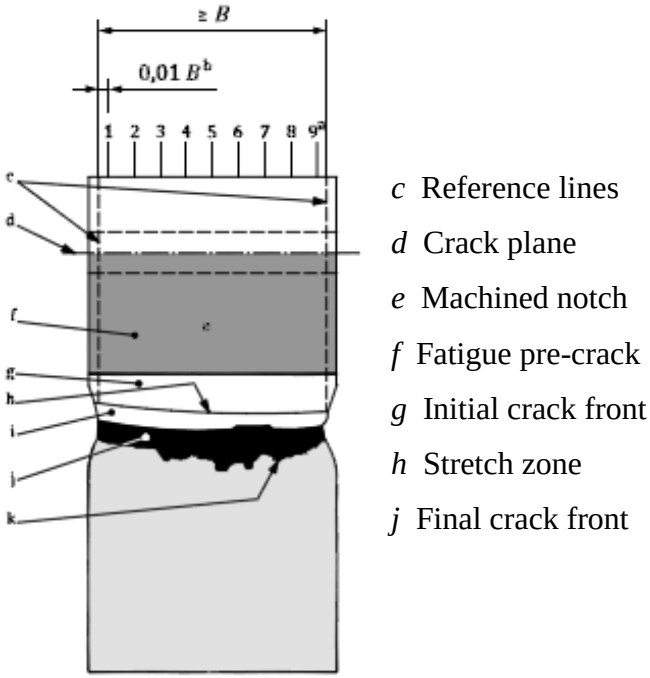

Figure 36. Schematic representation of a typical fracture surface [61].

3.8 Post-Test Metallography and Fractography

In order to validate initial machining location and crack growth direction post-test metallography was implemented. After fracture toughness tests were performed specimens were sectioned. Instead of heat tint, post fatigue pre-cracking was utilized to obtain a flat fracture surface for post-test metallography and fractography since heat tint could influence the microstructure of specimens. Representative view of sectioned post-test metallography specimens is given in Figure 37.

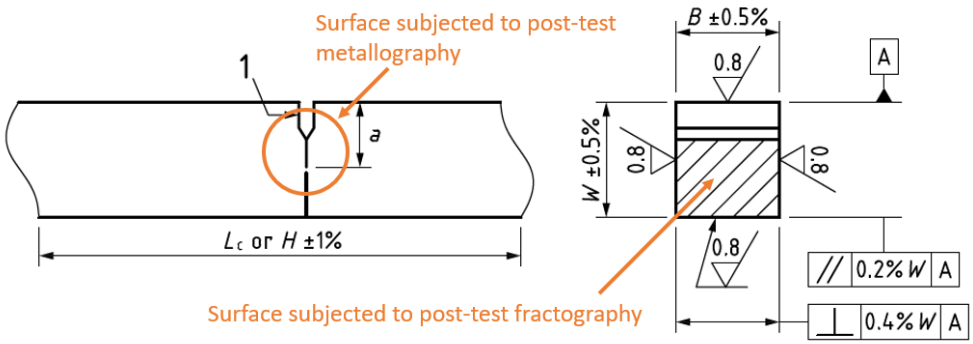

Figure 37. Schematic view of specimens used for post-test metallography and fractography [62].

For determination and monitoring secondary phases under high resolution SEM was used.

CHAPTER 4

RESULTS

4.1 Elemental Analysis

Chemical compositions of parent metal and deposited block are stated in Table 6. Optical emission spectroscopy was used for chemical analysis. When specifications of coupons are considered, the result are coherent and in acceptable range with specifications.

Table 6. Chemical compositions of parent metal (2507) and wire arc additive manufactured block (2509).

	wt. %						
2507	***Cr***	***Ni***	***Mo***	***Mn***	***Si***	***C***	***W***
	24.7	6.6	3.64	0.78	0.32	0.021	0.085
	N	***Cu***	***Nb***	***Ti***	***V***	***Al***	***Co***
	0.28	0.21	0.01	0.01	0.05	0.01	0.075
2509	***Cr***	***Ni***	***Mo***	***Mn***	***Si***	***C***	***W***
	24.6	9.38	4.2	0.35	0.42	0.012	0.07
	N	***Cu***	***Nb***	***Ti***	***V***	***Al***	***Co***
	0.18	0.095	0.025	0.011	0.05	0.09	0.064

Oxygen and nitrogen percentages of coupons, which were determined according to ASTM E1019 [51], are shown in Table 7. Even if the used filler wire was same for all coupons, oxygen and nitrogen fractions are different due to deposition with different shielding gases.

Table 7. Oxygen and nitrogen measurements of coupons built under $Ar+O_2$ and $Ar+N_2$ shielding gases.

	Oxygen %		**Nitrogen %**	
	Measurement 1	**Measurement 2**	**Measurement 1**	**Measurement 2**
$Ar+O_2$	0.1370	0.1210	0.1650	0.1590
$Ar+N_2$	0.0359	0.0389	0.2110	0.2030

PRE_W, Cr_{eq} and Ni_{eq} are calculated according to below formulas [39, 64];

$$PRE_W = \%Cr + 3.3(\%Mo + 0.5\%W) + 16\%N \quad (24)$$

$$Cr_{eq} = \%Cr + 2\%Si + 1.5(\%Mo + \%Ti) + 5\%V + 5.5\%Al + 1.75Nb + 0.75W \quad (25)$$

$$Ni_{eq} = \%Ni + \%Co + 0.5\%Mn + 0.3\%Cu + 25\%N + 30\%C \quad (26)$$

PRE_W, Cr_{eq} and Ni_{eq} values of specimens are listed in Table 8. It is stated at earlier chapter that super duplex stainless steel has a PRE_N that is greater than 40. Since it is present in alloying, W element is also taken into consideration and PRE_W is calculated. Both 2507 and 2509 ($Ar+O_2$) have PRE_W values higher than 40.

Table 8. PRE_W, Cr_{eq} and Ni_{eq} values.

	PRE_W	**Cr_{eq}**	**Ni_{eq}**
2507	41.37	31.24	14.73
2509	41.45	32.60	14.51

4.2 Integrity Confirmation

Since discontinuities strongly affects fracture toughness performance of structures, detection of volumetric and surface imperfections is essential. For volumetric imperfections, radiography tests were evaluated according to ISO 5817 [54] that is valid for arc-welded joints of steel, nickel and titanium alloys. There are quality levels that are B, C and D in which B has lowest tolerance to imperfections and represents highest quality. All deposited blocks were defect free or defects were in acceptable range. They fulfilled requirements of Class B which is greatest level in terms of quality. For surface imperfections, liquid penetrant tests revealed that there was no discontinues on surfaces of all deposited blocks.

4.3 Thermal Cycles

During being exposed to multiple thermal cycles, temperature measurements were conducted. K-Type thermocouples, with ceramic protection, were utilized while manufacturing. Measurements are given in Figure 55 and Figure 61.

4.4 Qualitative and Quantitative Phase Analysis

Corresponding locations of grade 2507 and grade 2509 according to their chemical compositions on Schaeffler Diagram are shown in Figure 38.

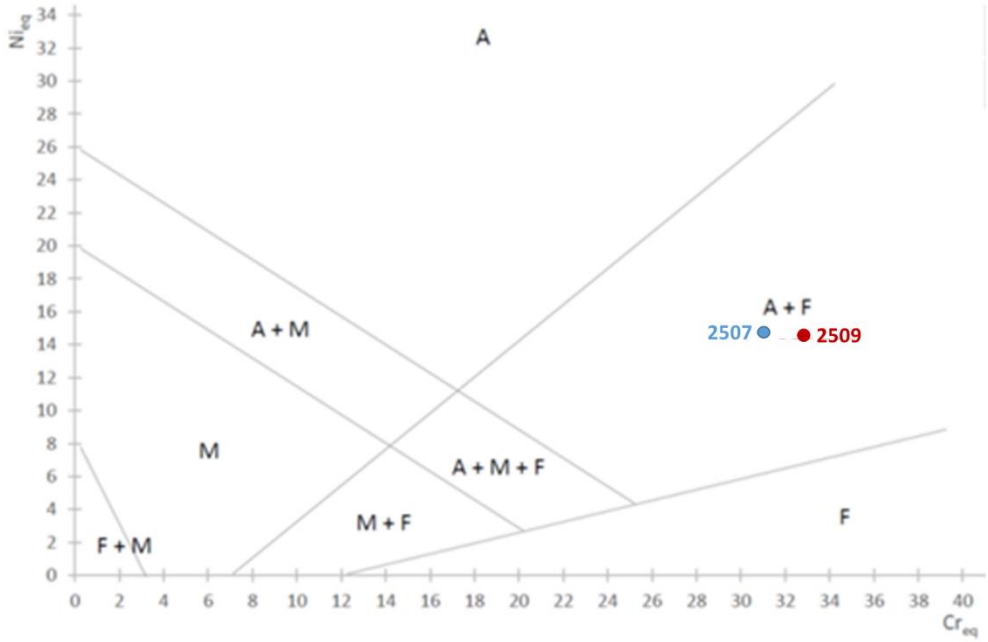

Figure 38. Location of grade 2507 and grade 2509 on Schaffler Diagram.

Phases and their fractions are determined according to XRD and metallography. The results are tabulated in Table 9.

Table 9. Phase fraction with respect to XRD and metallography.

	2507	**2509 ($Ar+O_2$)**	**2509 Sol. ($Ar+O_2$)**	**2509 ($Ar+N_2$)**
δ/γ XRD	57.3% / 42.7%	29.3% / 70.7%	35.5% / 64.5%	34.2% / 65.8%
δ/γ Metallography	54.1% / 45.9%	31.2% / 68.8%	36.5% / 63.5%	35.3% / 64.7%

Microstructure of specimens were investigated under optical microscope. Images and XRD graphs are given below:

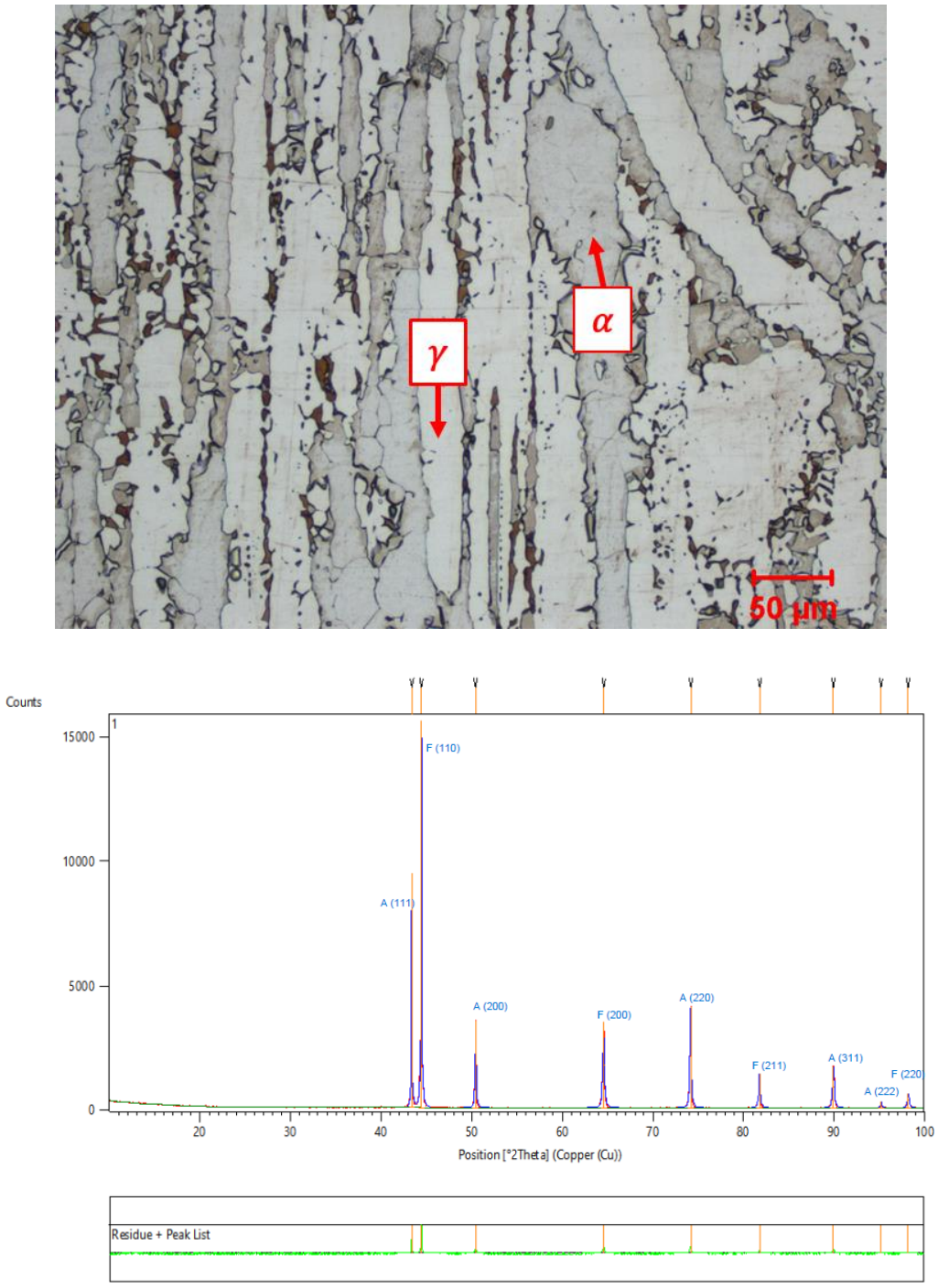

Figure 39. OM micrograph and XRD of 2507.

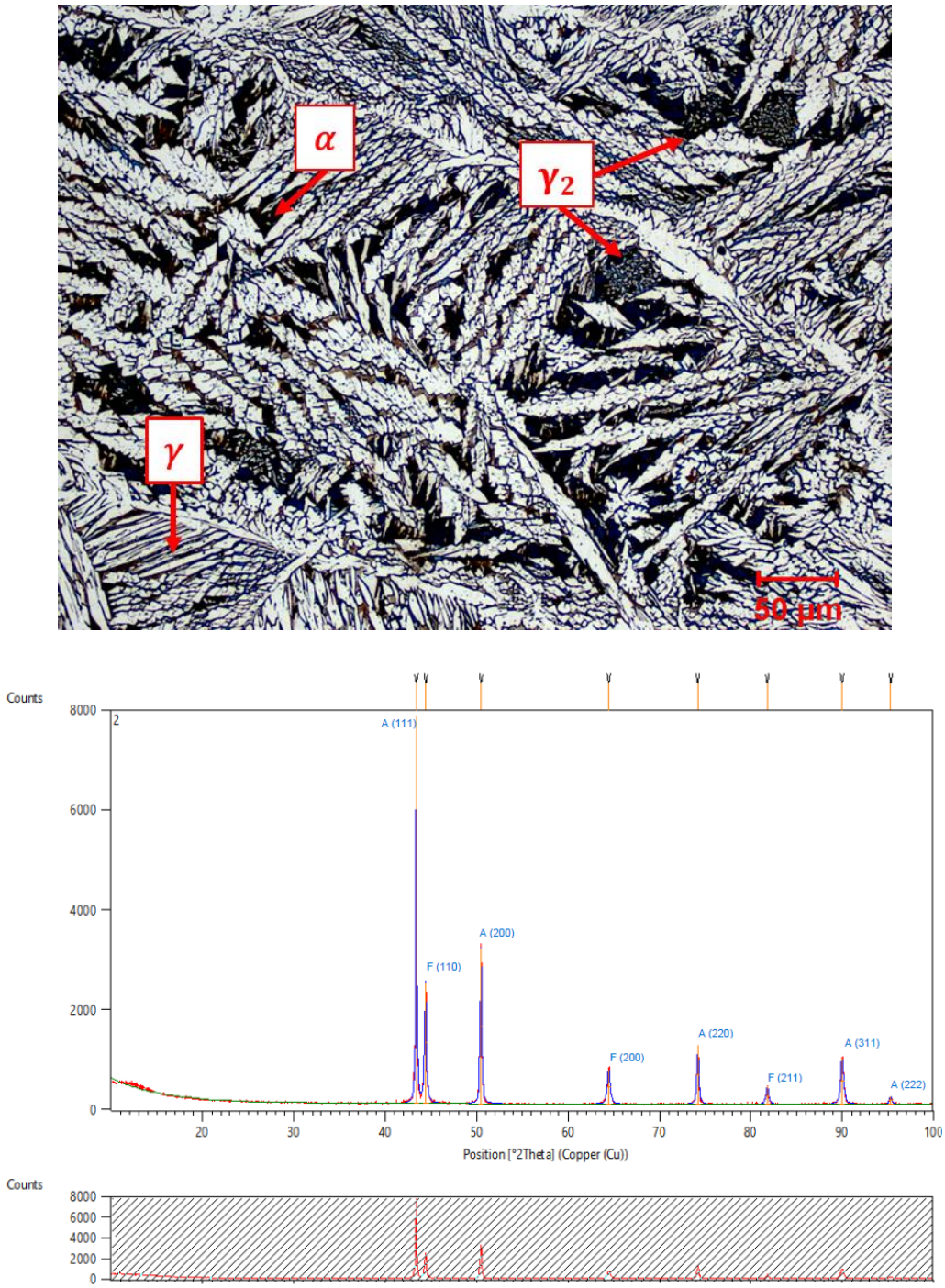

Figure 40. OM micrograph and XRD of 2509 ($Ar+O_2$).

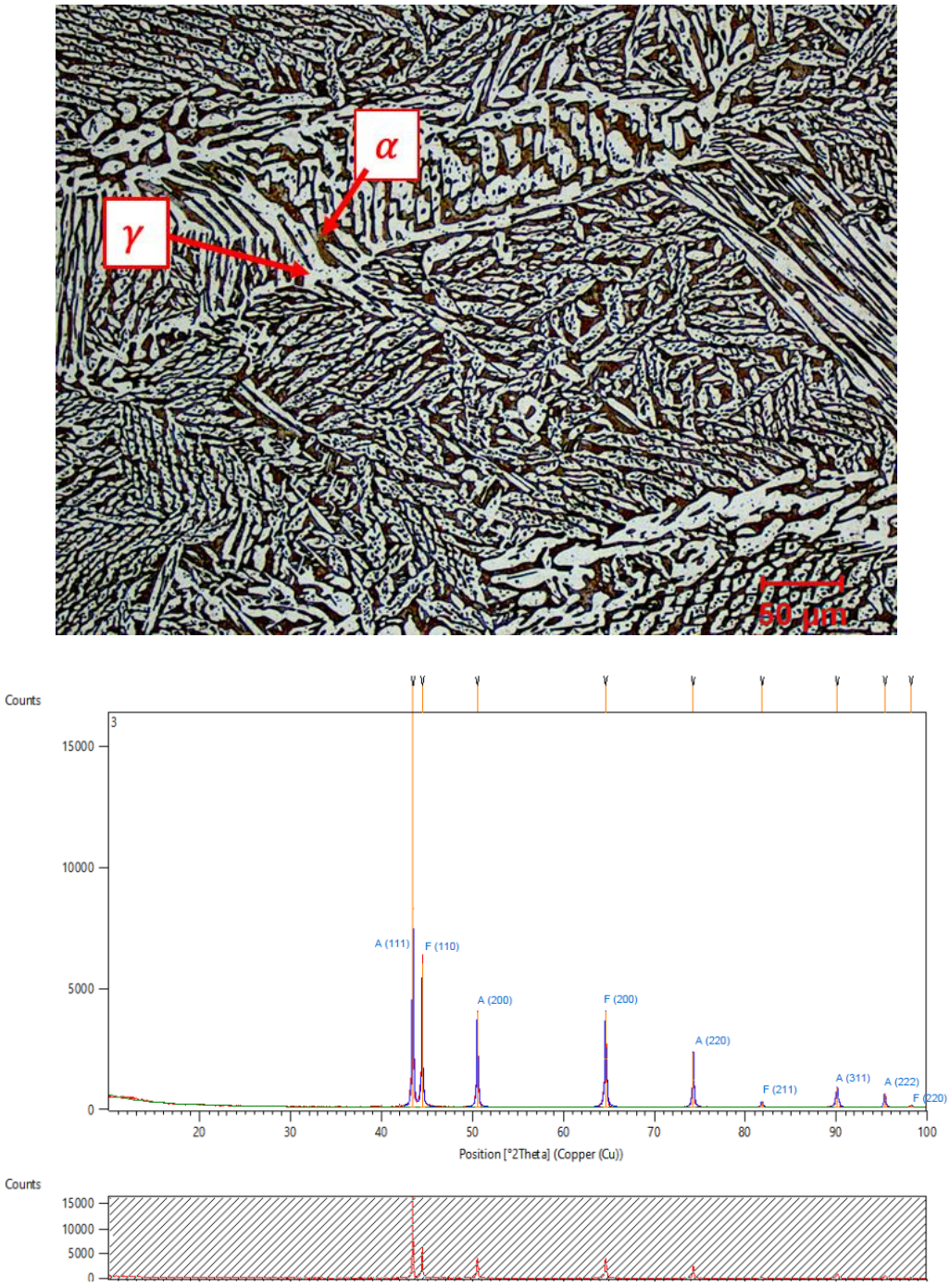

Figure 41. OM micrograph and XRD of 2509 Sol. ($Ar+O_2$).

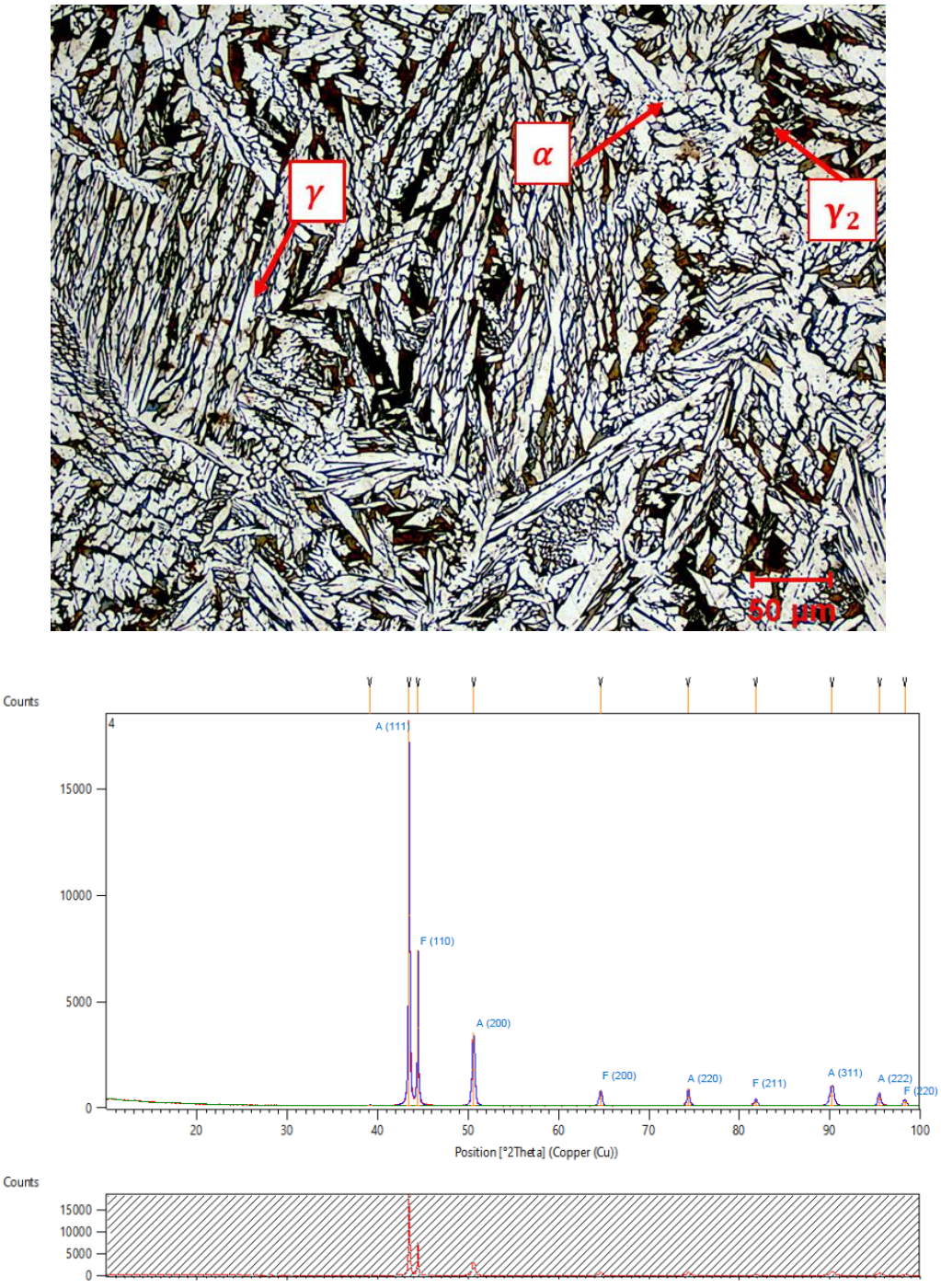

Figure 42. OM micrograph and XRD of 2509 ($Ar+N_2$).

Micro hardness test was employed to coupons in order to distinguish hardness of individual phases. Maximum hardness values and mean hardness values are given in Table 10.

Table 10. Maximum and mean micro hardness values of coupons.

	2507	**2509 ($Ar+O_2$)**	**2509 Sol. ($Ar+O_2$)**	**2509 ($Ar+N_2$)**
Max. hardness (HV 0.5)	290	325	285	288
Mean hardness (HV 0.5)	271	288	259	265

Probability densities of micro hardness values of coupons are given in Figure 43. It is seen that 2509 ($Ar+O_2$) has a wider range of hardness values with a maximum and minimum of 325 and 257 respectively.

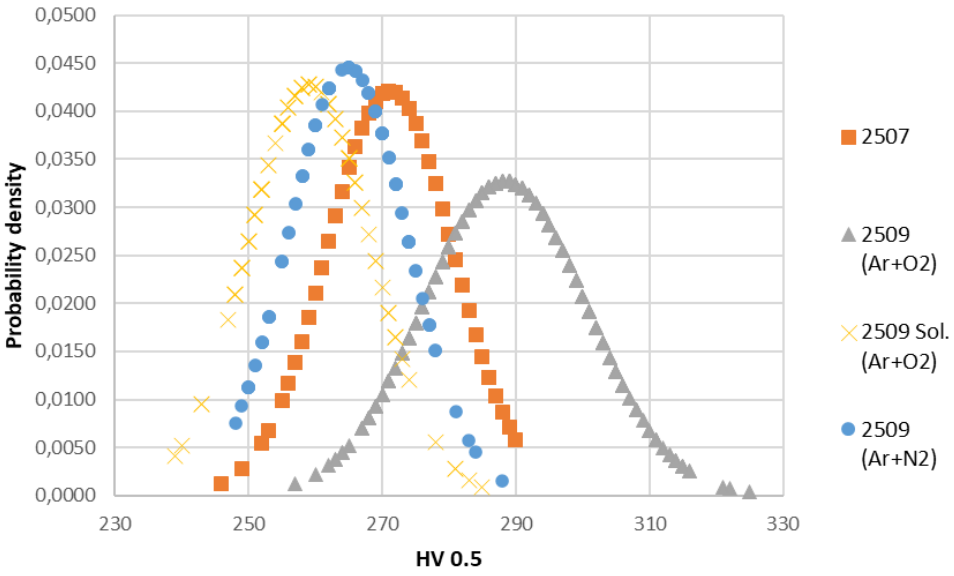

Figure 43. Probability densities of HV0.5 values of coupons.

Contour map of micro hardness values of 2509 (Ar+O_2) are given in Figure 44. When the map is investigated, it is seen that the areas close to fusion line zone has highest hardness.

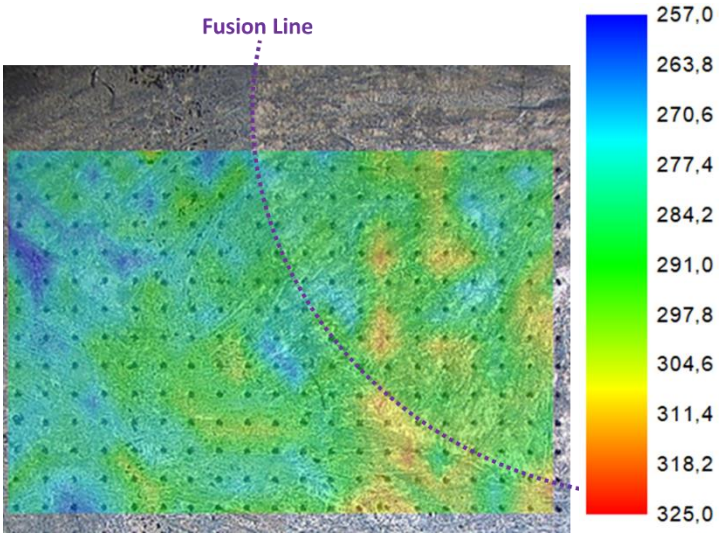

Figure 44. Contour map of HV 0.5 microhardness of 2509 (Ar+O_2).

4.5 Strength, Ductility and Fracture Toughness Parameters

Tensile test results of coupons are given in Table 11 and stress - strain curves are given in Figure 45. Tests were carried out under room temperature. It is clear that 2509 (Ar+O_2) has greater strength but lower ductility compared to 2507.

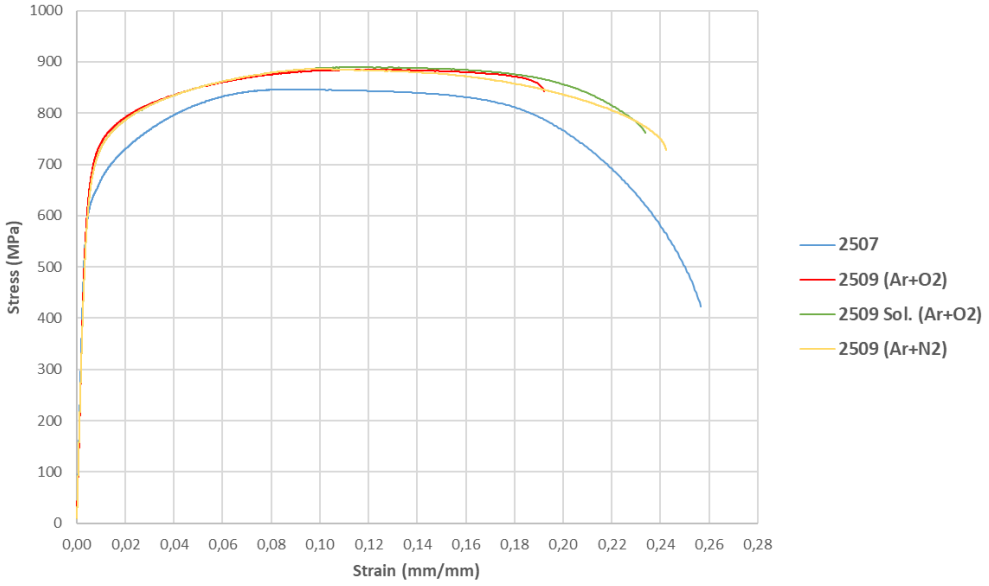

Figure 45. Stress - strain curves of coupons.

Table 11. Results of tensile tests.

	2507	**2509 ($Ar+O_2$)**	**2509 Sol. ($Ar+O_2$)**	**2509 ($Ar+N_2$)**
Yield Strength 0.2% offset ($R_{p0.2}$) (MPa)	635	694	695	687
Ultimate Tensile Strength (R_m) (MPa)	846	885	890	886
Young's Modulus (E) (GPa)	209	208	204	206
Elongation (A) (%)	37.9	22.8	26.1	31.1
Reduction in Area (Z) (%)	80.0	35.2	37.9	44.1

Coupons of 2507 and 2509 ($Ar+O_2$) were tested at -10°C via SENT specimens up to maximum stable crack extension points. Additionally, in order to support micro

hardness investigation results, notches were positioned in two different locations which are BCL and FL for 2509 (Ar+O_2) as stated in previous chapter. Forces versus CMOD curves of coupons are given in Figure 46.

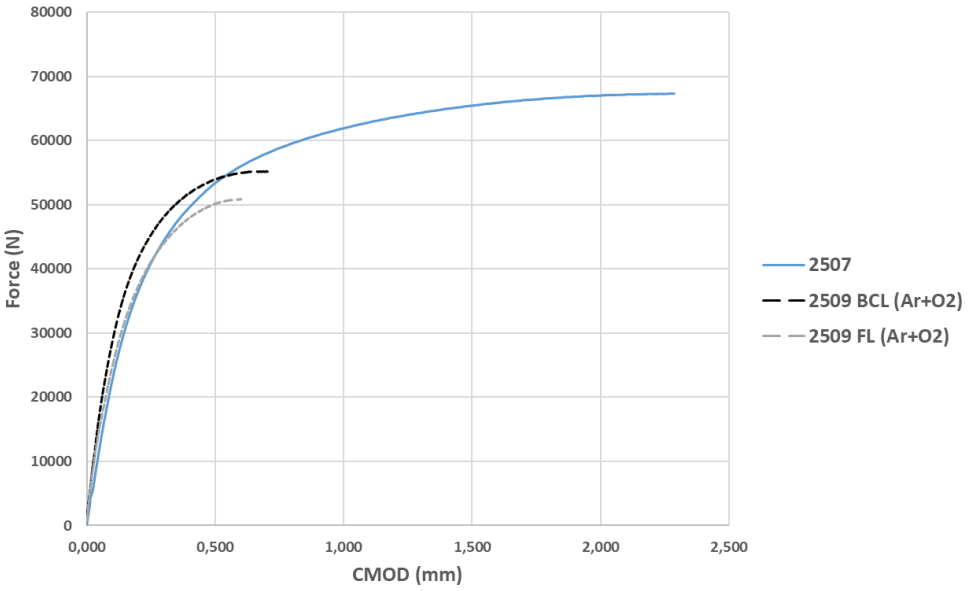

Figure 46. Force versus CMOD graphs of SENT specimens.

Calculated single point *J* values of SENT specimens are given in Table 12. As seen from results, 2509 BCL (Ar+O_2) which's notch was positioned at bead centerline has higher *J* value than 2509 FL (Ar+O_2) which's notch was positioned at fusion line zone.

Table 12. Fracture toughness of SENT specimens in terms of *J*.

	2507	**2509 BCL (Ar+O_2)**	**2509 FL (Ar+O_2)**
J_c (N/mm)	1301	339	255

Coupons of 2507, 2509 (Ar+O_2), 2509 Sol. (Ar+O_2) and 2509 (Ar+N_2) were tested at -10°C via SENB specimens up to maximum stable crack extension points. Additionally, again for encouraging micro hardness results, notches were positioned in two different locations which are bead centerline and fusion line for 2509 (Ar+O_2) as stated in previous chapter. Notch positions Forces versus CMOD curves of coupons are given in Figure 47.

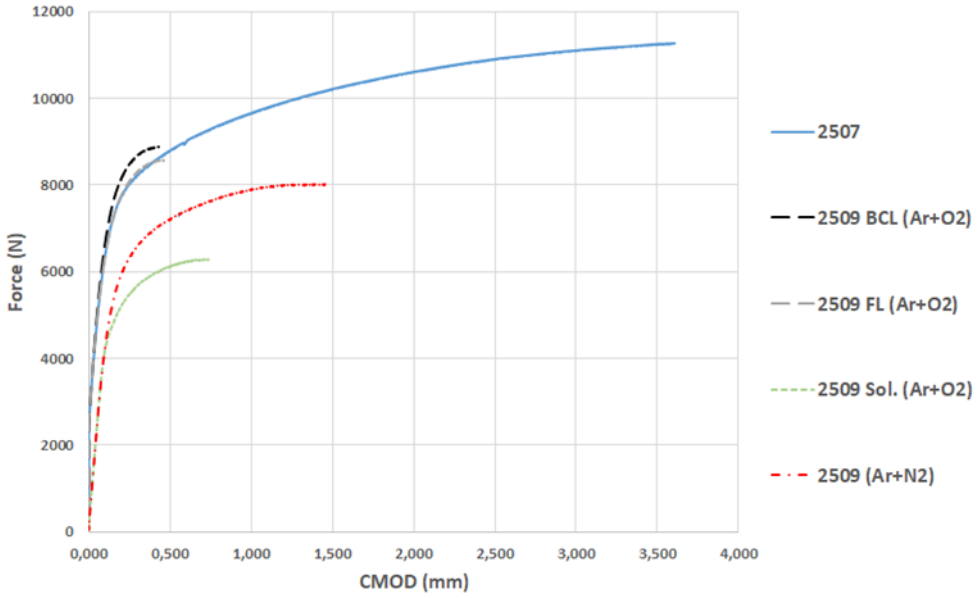

Figure 47. Force versus CMOD graphs of SENB specimens.

Calculated single point *J* values of SENB specimens are given in Table 13. Unlike SENT specimens, *J* results of SENB specimens of 2509 (Ar+O_2) do not differ remarkably. *J* results of 2509 BCL (Ar+O_2) and 2509 FL (Ar+O_2) are very close to each other in which notch is positioned at bead centerline and fusion line zone respectively.

Table 13. Fracture toughness of SENB specimens in terms of *J*.

	2507	**2509 BCL ($Ar+O_2$)**	**2509 FL ($Ar+O_2$)**	**2509 Sol. ($Ar+O_2$)**	**2509 ($Ar+N_2$)**
J_c (N/mm)	967	91	90	129	404

When Figure 46 and Figure 47 are analyzed, it is clear that coupon of 2509 ($Ar+O_2$) has low CMOD whereas force values are analogous in both notch configurations compared to reference parent metal 2507.

4.6 Post-Test Metallography and Fractography

The results of post-test metallography and fractography investigations are given in the following chapter.

CHAPTER 5

DISCUSSION

Fracture mechanics in a material is important in evaluating the structural integrity of the material and has a strong relation with the microstructure. The fracture behavior of a material can be evaluated by impact or fracture toughness testing. Whereas impact toughness testing uses a short blunt notch (2 mm deep 45° V notch with 0.25 mm tip radius) and dynamic loading to introduce the stress triaxiality and the plastic constraint, which is the consequence of the Poisson effect limitation due to material elasticity near the localized plastic zone, fracture toughness testing utilizes a sharp fatigue pre-crack and quasi-static loading. The pre-crack in the fracture toughness test specimens can simulate the most aggressive discontinuity in the material compared to the V-notch in the impact specimens, as well as allowing the specific fracture behavior of the targeted microstructure to be examined.

Fracture toughness is a mechanical metallurgy argument that defines the resistance of materials to brittle fracture. Stress-intensity factor definition is given in the linear-elastic fracture mechanics (LEFM) approach which lends itself to a quantitative analysis of fracture in terms of critical flaw sizes and stress levels. However, the ductile materials, like DSS, are beyond the region of LEFM applicability and elastic-plastic fracture toughness parameters emerge for such materials. The objective of elastic-plastic fracture toughness testing is to load a fatigue pre-cracked test specimen to include either stable or unstable crack extension, i.e. fracture instability (Figure 48).

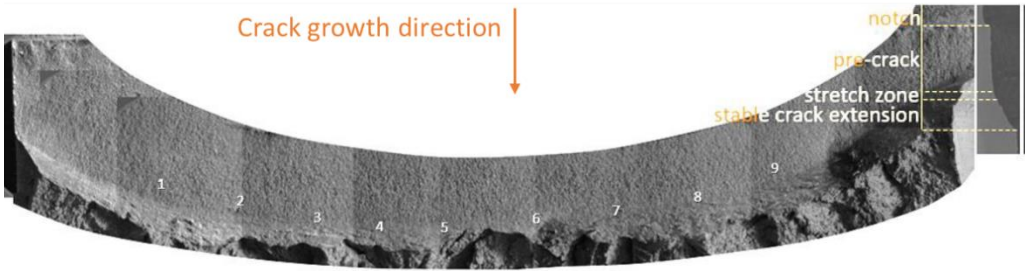

Figure 48. An example fracture surface which indicates 9 measurement points of notch, fatigue pre-cracking, stretch zone and stable crack extension [65].

5.1 Fracture Toughness with respect to Specimen Configuration

Fracture instability results in a single point value of fracture toughness determined at the point of instability, whereas stable tearing results in a continuous fracture toughness versus crack-extension relationship, which is called resistance curve (R-curve). On the R-curves, significant point-values may be determined for any assessment of the fracture toughness performance of material. While ASTM E1820 [66] or ISO 12135 [61] are applicable for single-edge bend, SE(B) or SENB, and compact tension, C(T) specimens, as the implementation of single edge notch tension, SENT, tests extend beyond the J R-curves for girth welds on enclosing assemblies described in DNVGL RP F108 [67], and into the British Standard BS 8571 [62].

Single parameter fracture toughness *J* or CTOD is applicable for evaluation of a cracked piece in case of small-scale yielding where plastic zone around crack is limited. As crack growth takes place, plastic zone becomes considerably large so that stresses and strains could not be defined by fracture toughness uniquely [68, 69]. At this point crack tip constraint have to be considered. Constraint could be defined as the difference in stress field of crack tip in the tested body and the reference (which is field of small-scale yielding) [69, 70]. There are several parameters such as loading type, mismatches in terms of strength, residual stresses and specimen geometry that have an effect on a crack's surrounding stress distribution. Due to these parameters, crack tip constraint is varied and fracture toughness is affected eventually [71].

Tearing resistance and constraint are inversely proportional. High constraint leads to a decrease in fracture toughness [72].

In this study, tests were carried out with both SENB and SENT specimens in order to determine the single point values and to obtain resistance curves if the microstructure allows. Figure 49 presents the load versus CMOD plots of specimens with SENB and SENT configurations sectioned and machined from SDSS 2507 plates. Obtained *J* values are also shown on the curves. As can be seen from the curves and the *J* values, the fracture toughness value of the material in the same condition is relatively lower when SENB type specimens are tested as compared to the values obtained when SENT type specimens are tested.

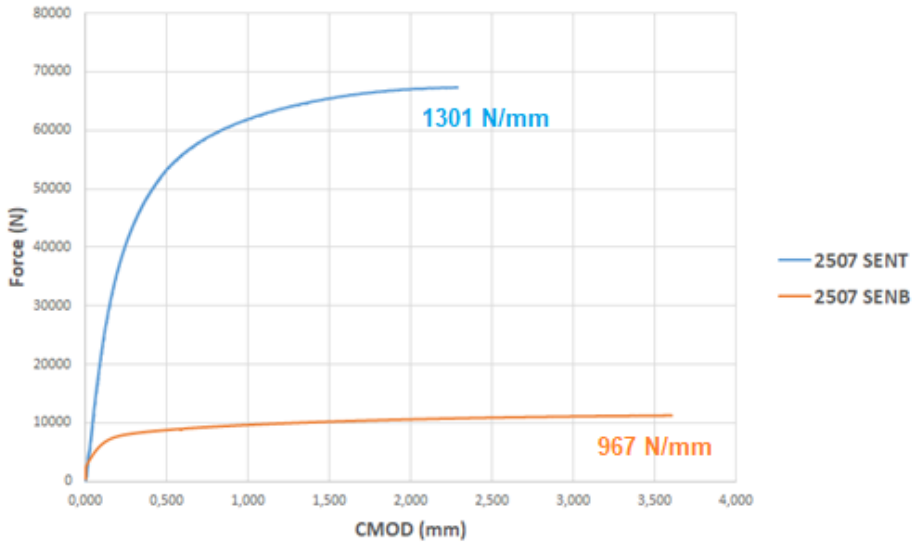

Figure 49. Force versus CMOD curves of SENT and SENB specimens of 2507 with calculated *J* values.

Since SENB has high constraint, it results in a lower bound fracture toughness. The situation is valid for all coupons which were tested. In addition, this consequence is also coherent with literature [68, 70, 71]. Crack tip constraint of SENT specimen is closer to the constraint of the structural part which is in service condition [73, 74]

(Figure 50). More accurate integrity assessments could be made by SENT specimens as they match with actual constraint and underpredictions could be avoided [65, 73, 75–77].

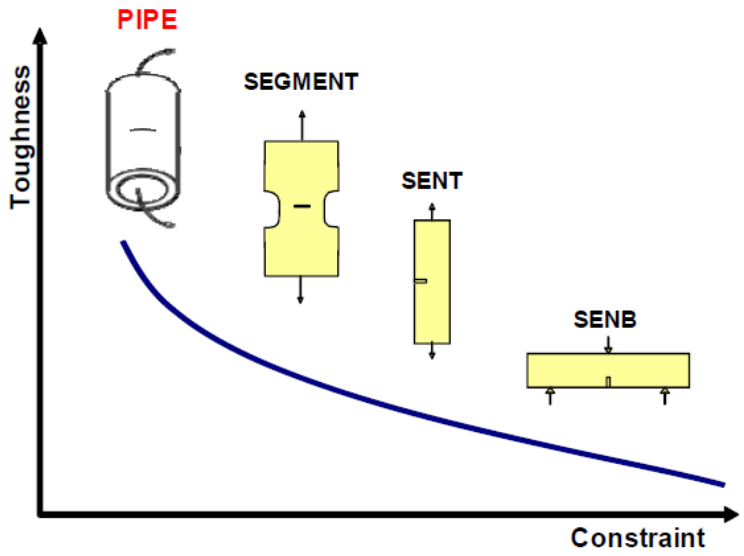

Figure 50. Toughness - constraint relationship of different loading types [74].

Crack tip plasticity is evaluated from quantity of strain hardening. As seen from Figure 51, micro hardness values of SENT specimens was higher as a result of strain hardening which indicates high crack tip plasticity and low constraint.

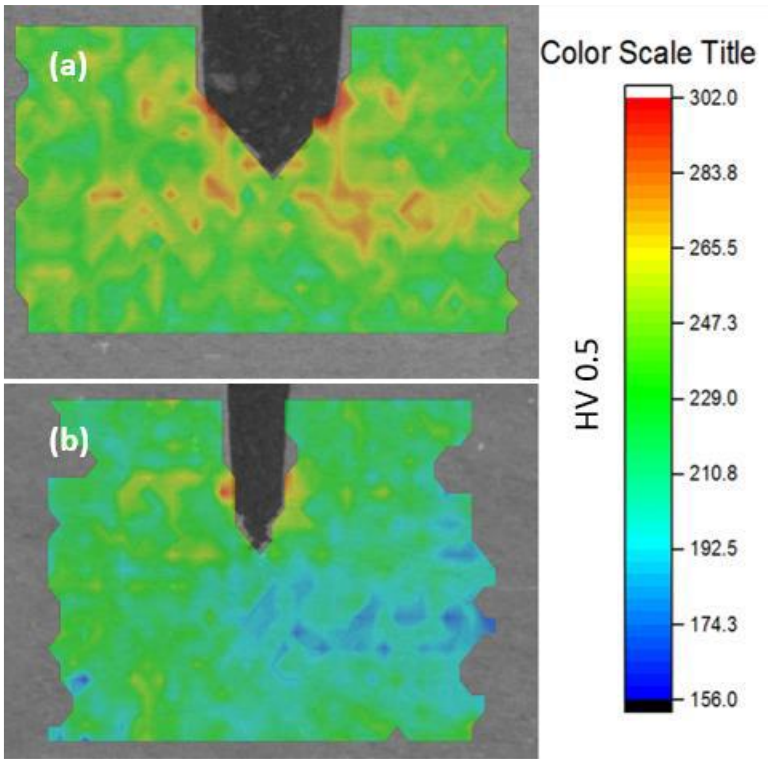

Figure 51. Micro hardness values of SENT (a) and SENB (b) specimens measured from cross section of fractured surfaces [65].

5.2 Fracture Toughness with respect to Notch Locations

The crack mount opening displacement (CMOD) measured under quasi-static loading simulate the pre-crack in the fracture toughness specimens, as well as possible flaws in the material. The most typical macro defects in additively manufactured assemblies may be cracks between solidification columns that meet at the center of the beads, or fusion failures between the beads. Any structural integrity assessment should take into consideration the presence of such flaws and ensure that the material exhibits sufficient toughness to prevent unstable flaw extension. In this respect, before testing the specimens with different material conditions, specimens with pre-cracks located at the bead centerline (BCL) and at the fusion line (FL) were tested (Figure 30 and Figure 52).

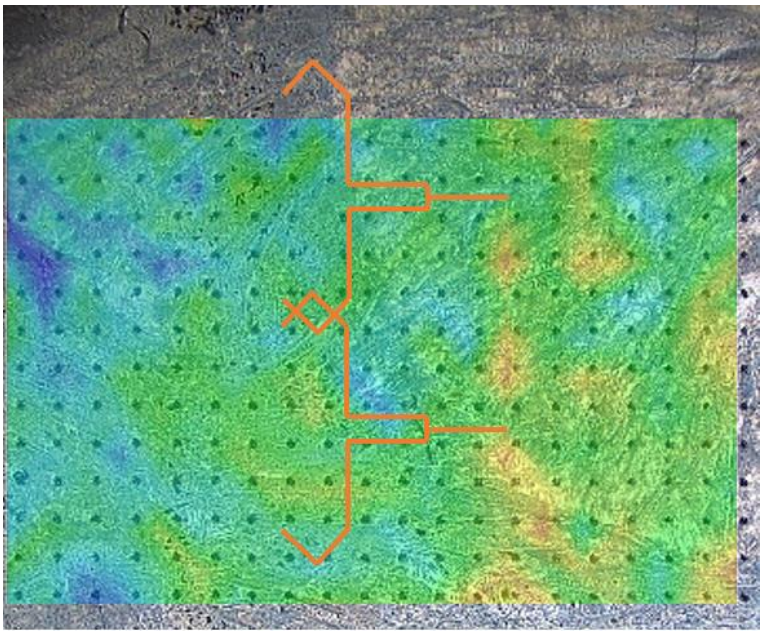

Figure 52. Notch locations and hardness map of 2509 ($Ar+O_2$).

As seen from Table 14, SENB results of BCL notched and FL notched specimens are very close to each other, nearly the same, whereas SENT results of BCL notched and FL notched specimens differ from each other, such that BCL notched SENT specimen is greater 33% than FL notched SENT specimen. This outcome demonstrates that SENB loading condition is so conservative that deviation due to different notch locations could not be identified. Since SENT loading type gives more practical attitude, variation in terms of notch positioning could be reflected to fracture toughness results. In order to observe the effect of significant microstructural features on fracture toughness and to compare with more conservative values, the study was continued with SENB tests.

Table 14. Fracture toughness of SENB and SENT specimens in terms of *J*.

	J_c (N/mm) SENB	J_c (N/mm) SENT
2507	967	1301
2509 BCL ($Ar+O_2$)	91	339
2509 FL ($Ar+O_2$)	90	255

5.3 Shielding Gas Composition and Material Condition

Except using self-shielded fluxed cored wires, shielding gases are used in WAAM operations to protect the fused metal from excessive oxidation and contamination of other gases in the ambient atmosphere. Since shielding gases can influence metal transfer mode, alloy content, bead shape, fume generation, and many other fused metal characteristics, their composition is one of the principal parameters in WAAM processes. However, investigations of microstructure and mechanical properties due to varying gas compositions are limited in the literature not only for duplex stainless but also for all other metal alloys, which have been investigated in terms of their additive manufacturability. Whereas the composition of shielding gases is quite important since it determines their ionization potential, dew point, thermal conductivity, specific gravity and density.

The stability of an arc is highly dependent on the ionization potential of the shielding gas used. On the one hand, it is mandatory to use pure inert gas in welding and WAAM processes of exotic alloys such as Aluminum, Titanium and Magnesium. On the other hand, it is possible to reduce the ionization potential of inert gases such as Ar (15.7 eV) and He (24.5 eV), which can be used in welding and WAAM operations of, with some active and reactive components, and thus to obtain a more stable arc. Active gases such as CO_2 (14.4 eV) and O_2 (13.2 eV), and reactive gases such as H_2 (13.5 eV) and N_2 (14.5 eV) have a lower ionization potential than inert gases and they can be mixed with inert gases in certain amounts for welding and

additive manufacturing of steels, including DSS. As the ionization potential of the shielding gas increases, the temperature of the arc increases as the ions release their ionization energies during contact with the molten metal surface.

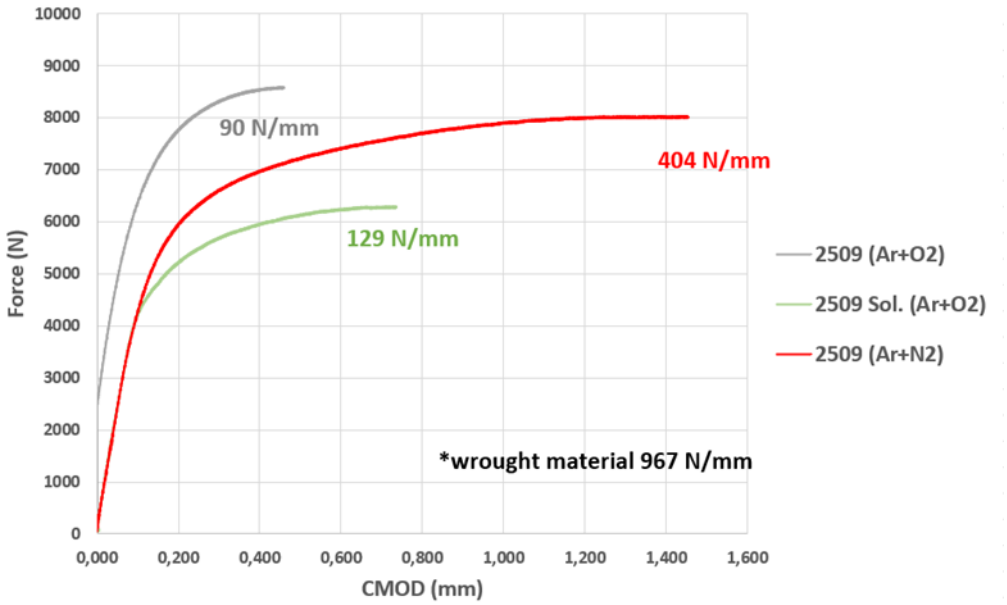

Figure 53. Force versus CMOD curves of SENB specimens with calculated *J* values.

In this study, two different mixed gases, in which the inert gas component is Ar and active/reactive gas component is either O_2 or N_2, were used while building the walls. Figure 53 shows the CMOD curves and fracture toughness values of SDSS structures obtained as a result of WAAM operations performed under shielding of Ar+O_2 and Ar+N_2 gas mixtures. As expected, the fracture toughness values of both walls are lower than for the same alloy grade (except for the 2% difference in Ni) in hot rolled and normalized condition. When the fracture toughness performance of the walls obtained with these two mixed gases is compared, it is observed that the SDSS wall built under Ar+N_2 mixed gas protection gives a more successful result, even though

$Ar+O_2$ shielding is more preferred in conventional duplex stainless steel welding operations.

The fracture phenomenon in SDSS is sensitive to fractions of the primary phases and their morphologies, and the secondary phases exist in the microstructure, their elemental constituents, morphologies and textures as well. Such microstructural features are determined primarily by the heat introduced by the arc and how fast the heat dissipates.

As mentioned previously, the heat input in WAAM operations can be calculated similarly to arc welding operations. This heat input can be approximated by multiplying the ratio of the arc power to the linear velocity of the arc by a factor called arc efficiency. Arc efficiency (or process efficiency) is a necessary input to numerical simulations or estimation of the as-built microstructure. Arc efficiency is simply the ratio between calorimetric energy input to the substrate or to the wall that have been piled up and the nominal energy input from the arc power supply. The arc energy input is commonly measured with the Seebeck calorimeter [78, 79] or any other calorimeter like nitrogen calorimeter and insulated box calorimeter.

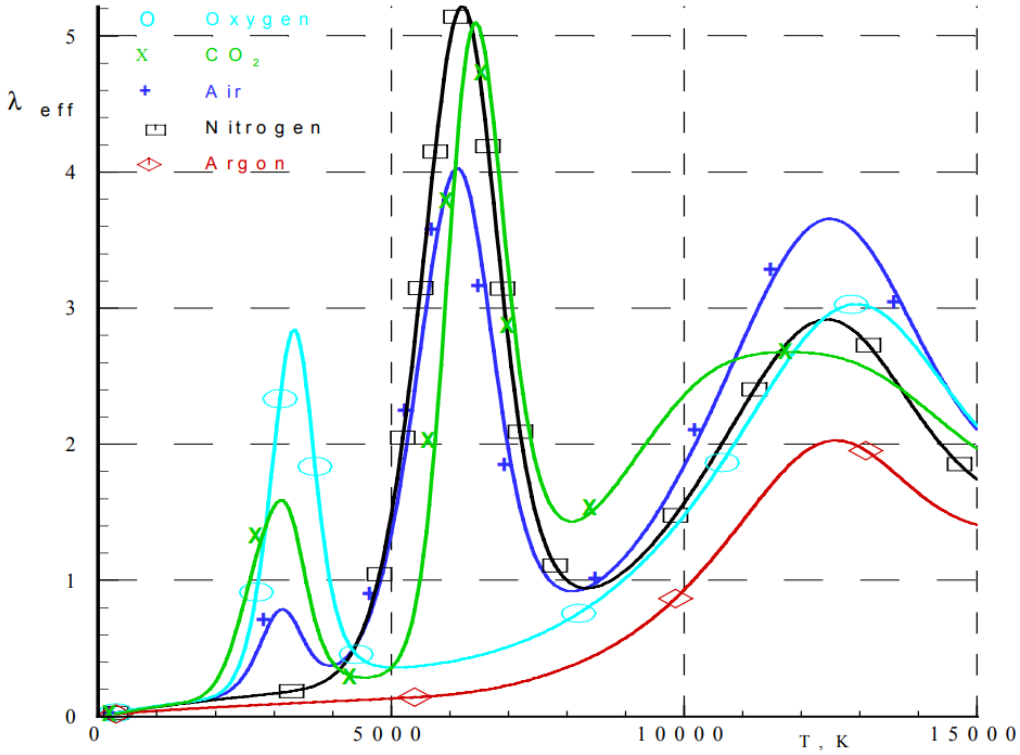

Figure 54. Heat conductivities ($W.m^{-1}.K^{-1}$) of various gases [80].

Despite to their lower ionization potential, O_2 and N_2 have higher thermal conductivity as compared to Ar (Figure 54). It is known that the arc efficiencies of active or reactive gases are relatively high compared to inert gases [81]. However, no study has been found in the literature comparing the effect of mixed gases with O_2 and N_2 constituents on the arc efficiency. Considering the thermal conductivity values at typical arc temperatures, which are 6000 K and more, it can be accepted that the mixed gas containing N_2 will have higher arc efficiency than the mixed gas containing O_2 (Figure 54). Since the process parameters such as arc power (3.78 kW), linear speed (7 mm s^{-1}) and interpass temperature (200°C) were kept constant in both operations, it is estimated that the heat input of the operation in which Ar+N_2 shielding gas is applied will be slightly higher than that in which Ar+O_2 shielding gas is applied (O_2 and N_2 are 2% in the gas mixtures). Concerning the possible heat inputs with respect to the shielding gas compositions, one could expect that the

austenite fraction would be higher in the walls built under $Ar+N_2$ shielding compared to the wall built under $Ar+O_2$ shielding, due to the relatively high heat input and therefore the relatively low cooling rate.

However, it has been observed that the walls built under $Ar+O_2$ protection contain 5% higher austenite than those built under $Ar+N_2$ shielding (Figure 40 and Figure 42). Of course, these phase fraction data obtained by quantitative metallography and XRD statistically represent reheated and/or remelted regions due to sampling. In a structure obtained by additive manufacturing, there is a very limited area that has not been reheated with subsequent passes. However, in addition to the difference between the heat inputs, the fact that the Nitrogen escape from the DSS structure under $Ar+N_2$ shielding would be relatively low and the Nitrogen content in the structure would be relatively rich, it might have been expected that the austenite content in this wall would have been higher. The inconsistency between the arc efficiency and heat inputs of the shielding gases used and the possible cooling rates depending on these, and the phase fractions in the as-built structures can be attributed to two reasons; differences in heat transfer conditions and/or secondary precipitations.

Regarding the amount of oxygen content in the shielding gasses, the oxide slag could have probably been thicker on the wall built under $Ar+O_2$, which would limit heat transfer via convection and radiation. These slag layers are very fragile and are largely shed when handling parts after operation or even during operation due to expansion and shrinkage of the part. Therefore, the thickness of the layers formed on the surface of the part could not be measured with respect to the active/reactive component used in the mixing gas. However, the temperature data collected during both operations show that the effect of the active/reactive component in the mixed gas on the cooling regime is insignificant (Figure 55). In this case, the phase ratios in the as-built structure can be explained by secondary/tertiary phase transformations.

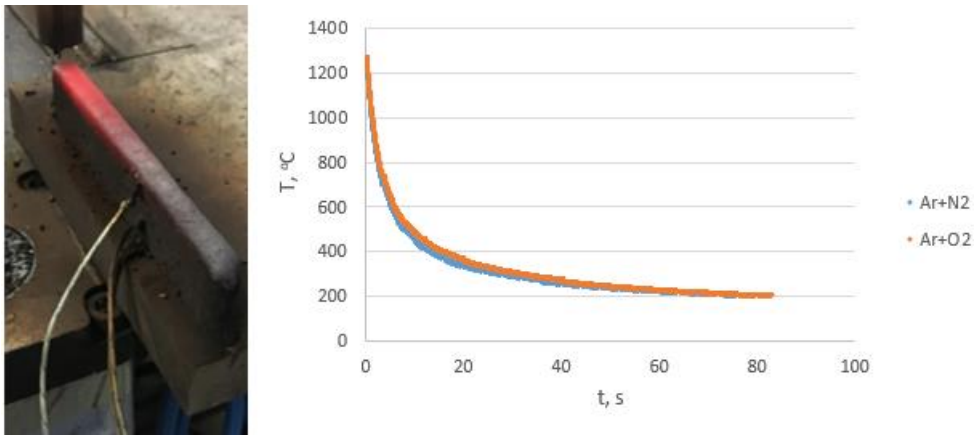

Figure 55. Attachment of thermocouples (left) and cooling curves of WAAM coupons manufactured by different shielding gas mixtures (right).

Liquid DSS with nonuniform element distribution crystallizes first in columnar and equiaxed δ grains. During cooling when the temperature falls down to about 1100°C, γ nucleates at the δ boundaries where austenite forming elements are segregated [82, 83]. When the temperature falls below the ones required for reconstructive phase transformation, austenite formation continues to take place from the allotriomorphic austenite by displacive transformation towards the grain interior (Widmänstatten austenite). Because the cooling rate of the molten metal is usually high in welding and additive manufacturing processes, the initial solidified microstructure is usually limited to the primary phases. However, exposing DSS to elevated temperatures (300 °C - 1000 °C) during application of the successive passes/layers leads to the formation of secondary phases, such as carbides ($M_{23}C_6$, M_7C_3), nitrides (π, CrN, Cr_2N), intermetallic phases (σ, χ, R), secondary austenite γ_2; in addition, G-phase formed by ferrite spinodal decomposition [84–89]. These phases certainly affect the mechanical, physical and chemical properties of DSS [87, 90–92]. The secondary and tertiary precipitations are generally rich in certain alloying elements and hence generate solute depleted zones at their proximity. Depending on their precipitation mechanism, they differ in texture with the neighboring ferrite and/or austenite phases as well.

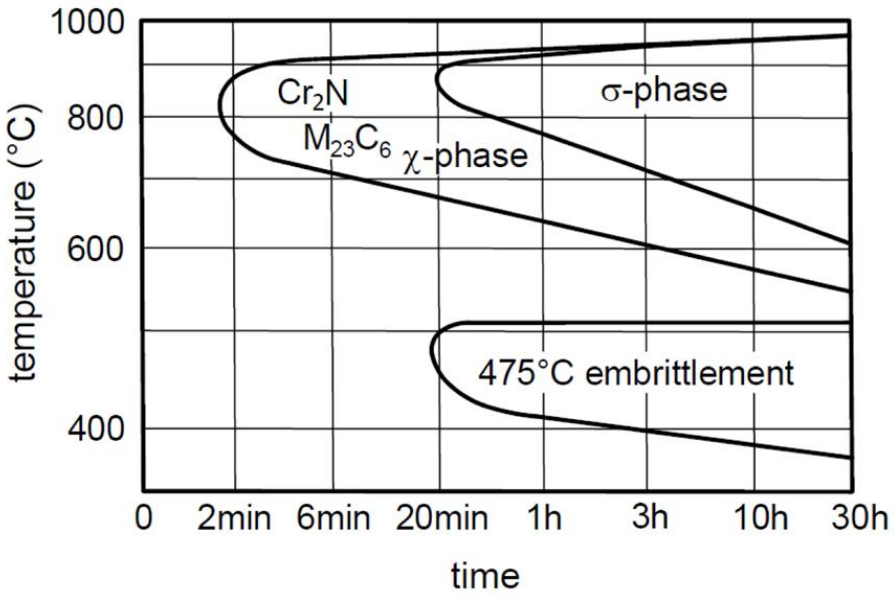

Figure 56. TTT curve for precipitations of DSS [93].

The main difference in terms of the microstructural features is that intragranular γ_2 formations are visibly more intense in the wall formed under $Ar+O_2$ shielding. Although γ_2 is present in the wall formed under the shielding of $Ar+N_2$, the austenite phase in this wall shows itself as longer Widmänstatten branches, which are close to each other, and γ_2's are mainly intergranular. Ramirez [94] and Atamert [95] suggest that the amount of γ_2 depends on the inclusion content and the grain size, as well as the cooling rate. The cooling rates and consequently Prior Ferrite Grain Size (PFGS) are comparative in both microstructures. Therefore, the inclusion content could be considered to provide the driving force for the intense propagation of γ_2 in the microstructure of the walls built under $Ar+O_2$ shielding.

The difference in fracture toughness performance of walls fabricated under different shielding gases are probably related to the secondary phases, with the difference in γ_2 formations being the most obvious difference in their microstructure. In order to examine the effects of secondary phases, post-test fractography and plateau metallography were performed. The fracture surface of the specimen sectioned from

the parent metal 2507 shows a ductile fracture dominated by larger and deeper dimples and voids. As compared to the parent metal specimens, although ductile character dominates at the vicinity of stretch zone in the specimens from the walls fabricated under $Ar+N_2$ shielding, there is a decrease in the size, number, and depth of dimples, which presents itself with reduced *J*-integral and CTOD values (Figure 57).

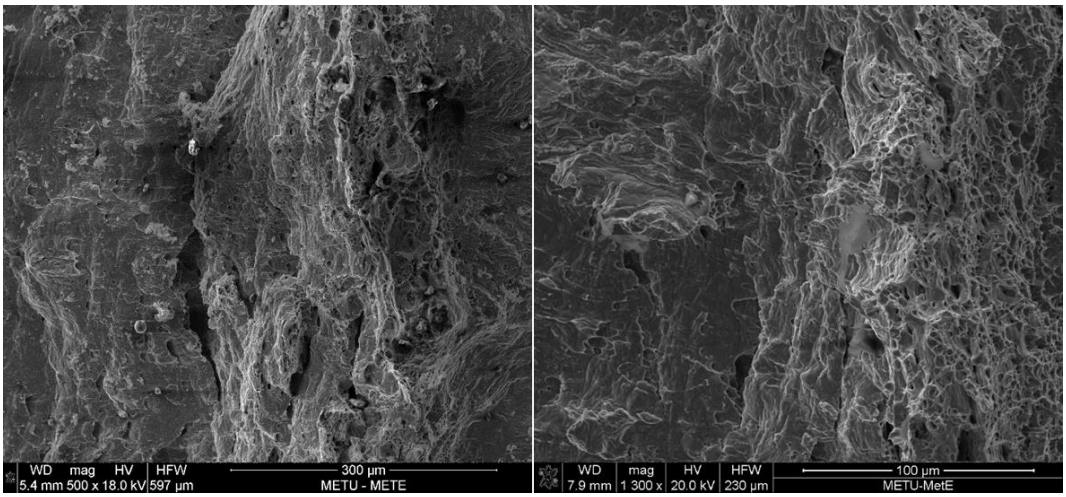

Figure 57. Fracture surface of SENB specimens sectioned from specimens built under $Ar+O_2$ (left) and $Ar+N_2$ (right).

Reduction in the elastic-plastic fracture toughness parameters are more severe in SENB specimens from the walls fabricated in $Ar+O_2$ atmosphere. A large number of oxide inclusions were found in shallow dimples (Figure 58), as well as and shear lips. Eo et.al. experienced that these oxide particles inside additively manufactured stainless steel were not a pure compound but a complex Si-Mn-Cr oxides [96].

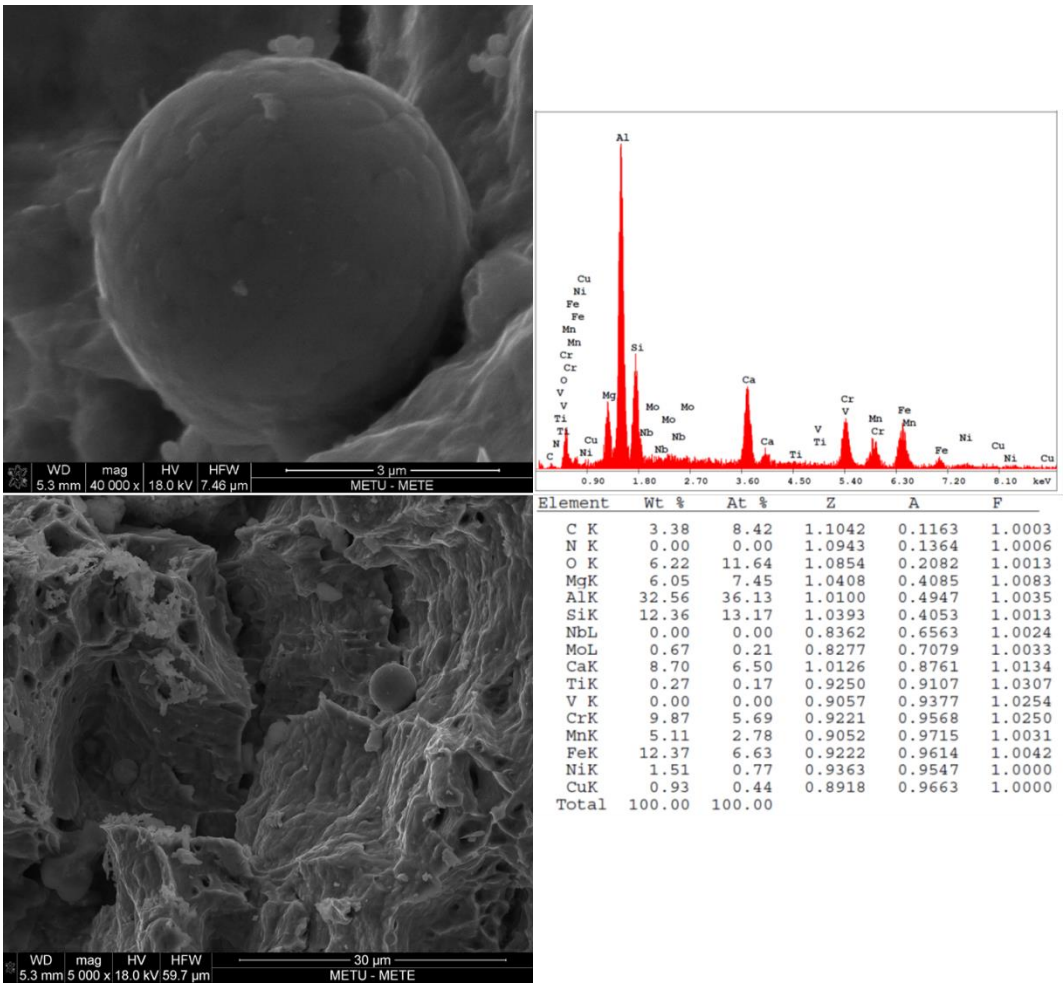

Element	Wt %	At %	Z	A	F
C K	3.38	8.42	1.1042	0.1163	1.0003
N K	0.00	0.00	1.0943	0.1364	1.0006
O K	6.22	11.64	1.0854	0.2082	1.0013
MgK	6.05	7.45	1.0408	0.4085	1.0083
AlK	32.56	36.13	1.0100	0.4947	1.0035
SiK	12.36	13.17	1.0393	0.4053	1.0013
NbL	0.00	0.00	0.8362	0.6563	1.0024
MoL	0.67	0.21	0.8277	0.7079	1.0033
CaK	8.70	6.50	1.0126	0.8761	1.0134
TiK	0.27	0.17	0.9250	0.9107	1.0307
V K	0.00	0.00	0.9057	0.9377	1.0254
CrK	9.87	5.69	0.9221	0.9568	1.0250
MnK	5.11	2.78	0.9052	0.9715	1.0031
FeK	12.37	6.63	0.9222	0.9614	1.0042
NiK	1.51	0.77	0.9363	0.9547	1.0000
CuK	0.93	0.44	0.8918	0.9663	1.0000
Total	100.00	100.00			

Figure 58. Oxides of 2509 ($Ar+O_2$) from fracture surfaces and EDX results of oxides.

It is seen that the specimens sectioned from the wall fabricated under $Ar+N_2$ have a relatively wide stretch zone, and the side cracks progress without a typical microstructural feature in the stable crack extension line. Whereas the crack extends in a dissociative manner with γ_2 particles as the source of cracking in the specimens from the wall built under $Ar+O_2$ shielding (Figure 59).

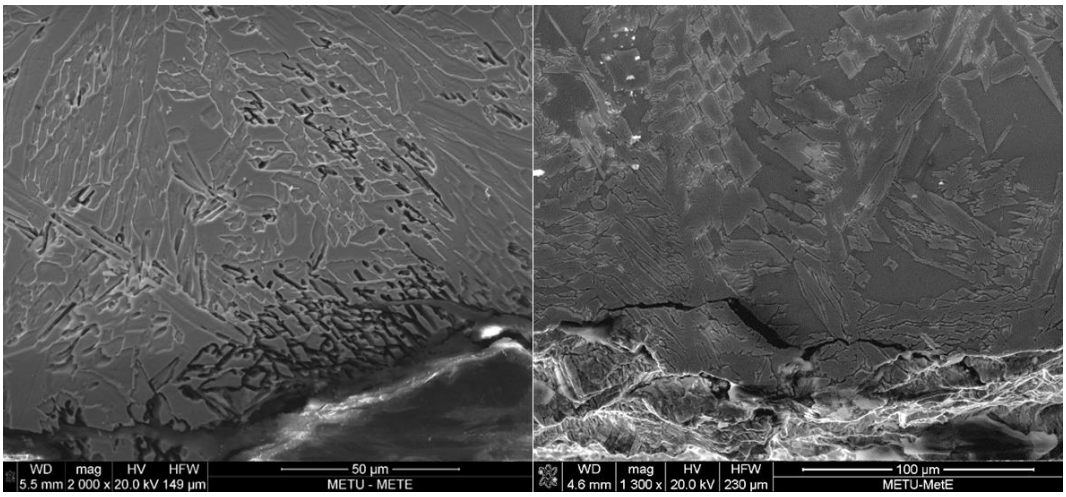

Figure 59. Fracture plateau of SENB specimens sectioned from specimens built under $Ar+O_2$ (left) and $Ar+N_2$ (right).

The intermetallic formation such as the sigma phase and nitrides were not evidenced in these post-test metallographic examinations with different etchants (Figure 60), as well as XRD analyses. However, oxide inclusions were confirmed on unetched metallographic specimens. Besides, as a result of inert gas fusion analysis, it has been understood that the main source of oxidation in the fusion zone is related to the shielding gas (Table 7).

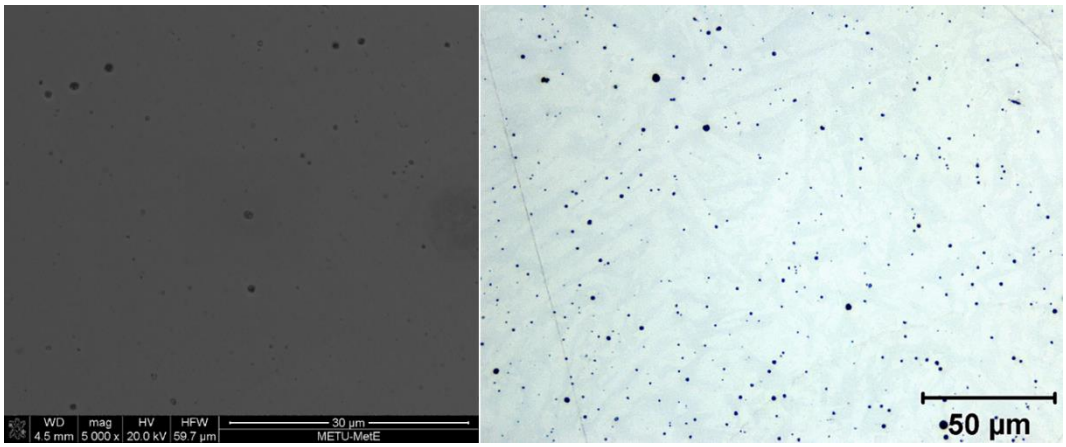

Figure 60. Unetched (left) and etched (right) microstructure images of $Ar+O_2$.

Due to the multiple thermal cycle exposure, decomposition of existing austenite occurs. It re-nucleates in ferrite phase among cooling. A certain amount of it grows with an acicular shape. This new precipitation is called secondary austenite [3, 97–99]. Secondary austenite is formed through diffusionless shear transformation [100]. Grain boundaries of ferrite phase have high energy therefore this region is an ideal nucleation site for WA austenite. Moreover, interface of ferrite and IGA which already transformed previously is another suitable site for nucleation [3]. Toughness improves through precipitation of secondary austenite [101, 102]. Under favor of fine crystal reinforcement impact, fine secondary austenite precipitations hinder crack propagation through ferrite grains which are brittle [30, 103].

Although secondary austenite was present in 2509 ($Ar+O_2$) somehow fracture toughness is deteriorated. At fusion zone concentration of oxide particles become higher if a shielding gas of 2.5% O_2 added argon is used during manufacturing of DSS [104]. As mentioned earlier in Table 3 one of the 2509 coupons was manufactured via $Ar+2\%O_2$. As clearly seen from Figure 58, oxide particles are present in 2509 ($Ar+O_2$). As a result of oxide inclusions, toughness is deteriorated since crack extension is encouraged in presence of them. The oxygen in the shielding gas is apparently arrested in the δ-phase matrix and formed inclusions. It is believed that the redistribution of these inclusions also creates sites for nucleation and growth of δ-phase during solidification and in the same way to generate austenite during cooling [11, 105].

Void nucleation becomes easier since large oxides could be cracked or debonded before deformation [48]. An interface is formed due to debonding of particle from matrix and when this interface coalescence with micro voids crack extension is favored [106]. If large size of inclusions (with a size of greater than 1 μm) exists, discontinuous fracture dimple and decreased area of load are main reasons of low toughness [102, 107]. From Table 14, it is seen that *J* values of both SENB and SENT specimens of 2509 ($Ar+O_2$) are considerably lower than reference 2507, due to the existed oxide inclusions with a size of approximately 5 μm. In addition, SENT specimens of W1 and FL1 are 339 N/mm and 255 N/mm respectively. Since oxide

concentration is greater at fusion zone, fracture toughness of FL1 is lesser. On the contrary, oxides lead to an increase in terms of hardness [102]. As seen from Figure 52, it is evident that regions of fusion line zone, where quantity of oxide inclusions are higher, micro hardness measurements also resulted in higher values [108].

5.4 Fracture Toughness with respect to Material Condition

From Figure 39 it is seen that microstructure of rolled 2507 was lamellar type where ferrite and austenite grains are in parallel arrangement. Due to this arrangement, a propagating crack is either deflected as it encounters phase interface or blunting occurs [109–111]. Since stresses around crack tip are relaxed, constraint becomes lesser [109, 112]. Furthermore, more energy is required for subsequent flaw initiation and extension and toughness is enhanced [109, 113, 114]. Fracture toughness of 2507 was greatest due to this phenomenon.

γ_2 has been reported to be formed by the eutectoid transformation from δ, where σ and Cr-nitrides may be the other product of this transformation [85, 88, 94, 101, 115–118]. In this synergic process, the precipitation of σ leads to Cr and Mo depletion and consequently surrounding δ becomes unstable. While this unstable δ transforms to γ_2, formation of γ_2 enriches its proximity in turn Cr and Mo, consequently, favors σ precipitation [118, 119]. In the present study, process conditions appear not to be sufficient for intermetallic precipitation (Figure 61). XRD and plateau metallography efforts did not indicate any intermetallic precipitation in the both as-built structures.

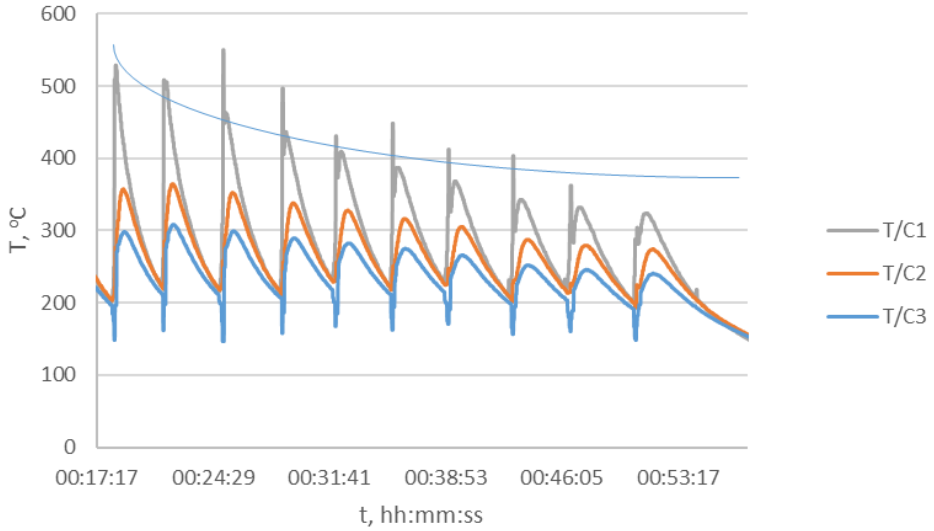

Figure 61. Cooling curves of subsequent weld passes.

Additionally, solution annealing is known to dissolve intermetallic formations [120]. When solution treatment, with parameters of 1100°C holding temperature for 1 hour and water quenching, was applied to 2509 ($Ar+O_2$), microstructure was changed. However, if there was a significant amount of intermetallic formation in the as-built structure, a greater increase in fracture toughness performance of the solution annealed structure would be expected. The increase in the fracture toughness value, though not radically, indicates other changes in the internal structure.

The one possible explanation is that the solutionizing heat treatment enables grain refinement. Grain boundary mobility is decreased as grains of austenite and ferrite are scattered. Due to restraint of grain growth, a finer microstructure is acquired [121]. As seen from Figure 40 and Figure 41, solutionized coupon 2509 Sol. ($Ar+O_2$) had finer grains while as build coupon 2509 ($Ar+O_2$) had coarser microstructure.

The crystallographic orientation of austenite [122–124] and interstitial elements, such as O and N [124], can also influence fracture behavior of the material. Certain ferrite-austenite orientations can restrict plastic deformation, and consequently promoting cleavage cracking. Whereas, interstitial elements raise the yield stress of

the ferrite matrix and again the cleavage failure may be promoted. Although the yield strength of solution annealed tensile specimens under argon atmosphere is comparable to specimens sectioned from the as-built structures (Figure 45), elemental analyzes indicate reduced N and O content (Table 7).

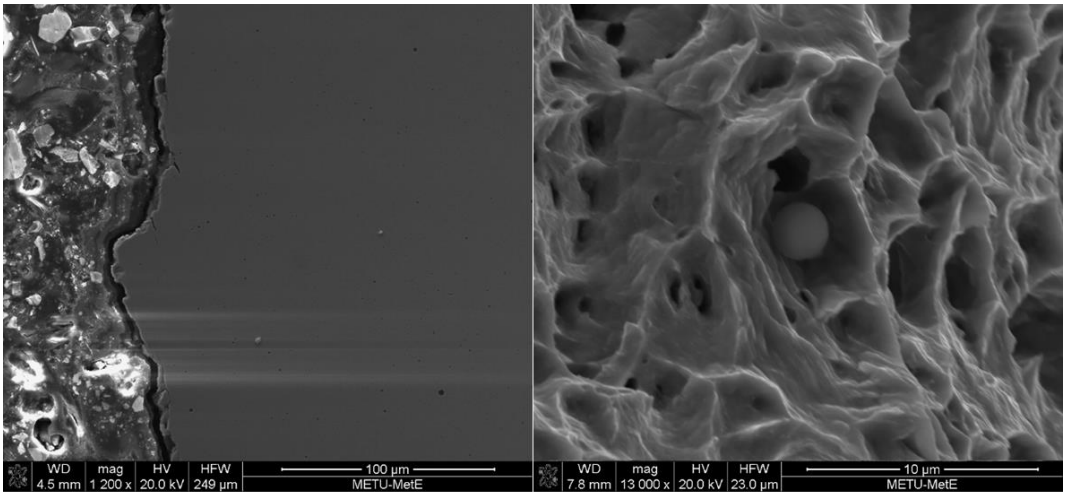

Figure 62. Fracture plateau (a) and fracture surface with dimples (b) of SENB specimen sectioned from the specimens of 2509 Sol. ($Ar+O_2$).

CHAPTER 6

CONCLUSION

In this study, additive manufacturability of super duplex stainless steels was investigated in terms of fracture toughness behavior, which is an important structural integrity parameter, and it constitutes an input in the design and fitness-for-service assessment of enclosing and supporting structures. Since assemblies made of duplex stainless steels are generally massive and have uncomplicated geometries, a direct energy deposition technique, namely wire arc additive manufacturing, was adopted in our study, where the feedstock wire was the grade 2509. Such assemblies are conventionally fabricated by casting or forging processes or by joining rolled materials. In this respect, the fracture toughness behavior of grade 2507 in hot rolled condition has been taken as reference in the study, considering that it will exhibit the best fracture toughness performance that can be obtained from this alloy.

In the literature, there are studies investigating the effects of different arc transfer modes and heat inputs on the microstructure and mechanical properties of wire arc additively manufactured duplex stainless steels. The primary interest in this present study was to investigate the effect of active (O_2) and reactive (N_2) agents in the shielding gasses on the as-built microstructure and its fracture behavior. Within this agenda, 2509 wire electrodes were deposited in shielding gas atmospheres with $Ar+O_2$ composition, which is popular in the welding of duplex stainless steels, and $Ar+N_2$ composition, which is not used much in welding processes.

The consequences of this study are mentioned below:

- As a result of the heat inputs and inter-pass temperatures adopted in this study, balanced primary phase fractions were obtained in both walls, and no intermetallic formations were detected in XRD analyses and metallographic examinations.

- The oxide inclusion density is higher in the walls deposited with an oxygen-containing shielding gas than in the walls deposited with a nitrogen-containing shielding gas. The inclusion content is suggested to provide the driving force for the intense propagation of secondary austenites in the microstructure of the walls built under $Ar+O_2$ shielding. The fracture toughness performance of the walls deposited by applying $Ar+O_2$ shielding gas is not conforming standard fitness-for-service requirements.
- Fracture toughness values of the solutionized structure suggest that the cause of the embrittlement of the as-built structure (obtained by $Ar+O_2$ shielding) is not intermetallic or other secondary phases that could be eliminated by solutionizing. The limited improvement in fracture toughness of the structure obtained by solution annealing can be explained by the decrease in residual stresses and grain refinement.
- Fracture toughness values in walls deposited under $Ar+N_2$ shielding are comparable to welded joints of wrought DSSs and conform to DNV requirements. N_2 addition in the shielding gas significantly compensated N loss and promoted the N solution in the structure. High N content caused a more efficient austenite formation and prevented high ferrite content in the structure despite rapid cooling.

REFERENCES

[1] L. Chen, H. Tan, Z. Wang, J. Li, and Y. Jiang, “Influence of cooling rate on microstructure evolution and pitting corrosion resistance in the simulated heat-affected zone of 2304 duplex stainless steels,” Corros Sci, vol. 58, pp. 168–174, May 2012, doi: 10.1016/j.corsci.2012.01.018.

[2] Y. Zhang, S. Wu, and F. Cheng, “A specially-designed super duplex stainless steel with balanced ferrite:austenite ratio fabricated via flux-cored wire arc additive manufacturing: Microstructure evolution, mechanical properties and corrosion resistance,” Materials Science and Engineering A, vol. 854, Sep. 2022, doi: 10.1016/j.msea.2022.143809.

[3] X. han Wu et al., “Morphologies of secondary austenite in 2507 duplex stainless steel after heat treatment,” Journal of Iron and Steel Research International, vol. 29, no. 6, pp. 994–1003, Jun. 2022, doi: 10.1007/s42243-021-00660-9.

[4] K. W. Chan and S. C. Tjong, “Effect of secondary phase precipitation on the corrosion behavior of duplex stainless steels,” Materials, vol. 7, no. 7. MDPI AG, pp. 5268–5304, 2014. doi: 10.3390/ma7075268.

[5] A. Maier et al., “Influence of process parameters on microstructural and mechanical properties of duplex stainless steel 2205 (1.4462) processed by DED-LB\M,” Procedia CIRP, vol. 111, pp. 241–246, 2022, doi: 10.1016/j.procir.2022.08.058.

[6] D. Zhang, A. Liu, B. Yin, and P. Wen, “Additive manufacturing of duplex stainless steels - A critical review,” Journal of Manufacturing Processes, vol. 73. Elsevier Ltd, pp. 496–517, Jan. 01, 2022. doi: 10.1016/j.jmapro.2021.11.036.

[7] V. A Hosseini, M. Högström, K. Hurtig, M. A. Valiente Bermejo, L. E. Stridh, and L. Karlsson, “Wire-arc additive manufacturing of a duplex stainless steel: thermal cycle analysis and microstructure characterization,” Welding in the World, vol. 63, no. 4, pp. 975–987, Jun. 2019, doi: 10.1007/s40194-019-00735-y.

[8] T. S. Srivatsan and T. S. Sudarshan, Additive Manufacturing Innovations, Advances and Applications. 2016.

[9] X. Zhang et al., “Microstructure and mechanical properties of TOP-TIG-wire and arc additive manufactured super duplex stainless steel (ER2594),” Materials Science and Engineering A, vol. 762, Aug. 2019, doi: 10.1016/j.msea.2019.138097.

[10] N. Knezović, I. Garašić, and I. Jurić, “Influence of the interlayer temperature on structure and properties of wire and arc additive manufactured duplex stainless steel product,” Materials, vol. 13, no. 24, pp. 1–16, Dec. 2020, doi: 10.3390/ma13245795.

[11] F. Hejripour, F. Binesh, M. Hebel, and D. K. Aidun, “Thermal modeling and characterization of wire arc additive manufactured duplex stainless steel,” J Mater Process Technol, vol. 272, pp. 58–71, Oct. 2019, doi: 10.1016/j.jmatprotec.2019.05.003.

[12] V. A Hosseini, K. Hurtig, and L. Karlsson, “Bead by bead study of a multipass shielded metal arc-welded super-duplex stainless steel,” Welding in the World, vol. 64, no. 2, pp. 283–299, Feb. 2020, doi: 10.1007/s40194-019-00829-7.

[13] M. F. Kanninen and C. H. Popelar, Advanced Fracture Mechanics. 1985.

[14] X. K. Zhu and J. A. Joyce, “Review of fracture toughness (G, K, J, CTOD, CTOA) testing and standardization,” Eng Fract Mech, vol. 85, pp. 1–46, May 2012, doi: 10.1016/j.engfracmech.2012.02.001.

[15] W. E. Frazier, “Metal additive manufacturing: A review,” Journal of Materials Engineering and Performance, vol. 23, no. 6. Springer New York LLC, pp. 1917–1928, 2014. doi: 10.1007/s11665-014-0958-z.

[16] S. M. Yusuf, S. Cutler, and N. Gao, “Review: The impact of metal additive manufacturing on the aerospace industry,” Metals, vol. 9, no. 12. MDPI AG, Dec. 01, 2019. doi: 10.3390/met9121286.

[17] T. DebRoy et al., “Additive manufacturing of metallic components - Process, structure and properties,” Progress in Materials Science, vol. 92. Elsevier Ltd, pp. 112–224, Mar. 01, 2018. doi: 10.1016/j.pmatsci.2017.10.001.

[18] American Society for Testing and Materials, “F2792-12a Standard Terminology for Additive Manufacturing Technologies,” 2015 doi: 10.1520/F2792-12A.

[19] B. Tomar, S. Shiva, and T. Nath, “A review on wire arc additive manufacturing: Processing parameters, defects, quality improvement and recent advances,” Materials Today Communications, vol. 31. Elsevier Ltd, Jun. 01, 2022. doi: 10.1016/j.mtcomm.2022.103739.

[20] D. Ding, Z. Pan, D. Cuiuri, and H. Li, “Wire-feed additive manufacturing of metal components: technologies, developments and future interests,” International Journal of Advanced Manufacturing Technology, vol. 81, no. 1–4. Springer London, pp. 465–481, Oct. 26, 2015. doi: 10.1007/s00170-015-7077-3.

[21] W. Huang, S. Chen, J. Xiao, X. Jiang, and Y. Jia, “Laser wire-feed metal additive manufacturing of the Al alloy,” Opt Laser Technol, vol. 134, Feb. 2021, doi: 10.1016/j.optlastec.2020.106627.

[22] A. Mostafaei et al., “Defects and anomalies in powder bed fusion metal additive manufacturing,” Current Opinion in Solid State and Materials

Science, vol. 26, no. 2. Elsevier Ltd, Apr. 01, 2022. doi: 10.1016/j.cossms.2021.100974.

[23] Z. Liu et al., “Additive manufacturing of metals: Microstructure evolution and multistage control,” J Mater Sci Technol, vol. 100, pp. 224–236, Feb. 2022, doi: 10.1016/j.jmst.2021.06.011.

[24] A. Bandyopadhyay and S. Bose, Additive manufacturing. 2016.

[25] D. G. Ahn, “Direct metal additive manufacturing processes and their sustainable applications for green technology: A review,” International Journal of Precision Engineering and Manufacturing - Green Technology, vol. 3, no. 4. Korean Society for Precision Engineering, pp. 381–395, Oct. 01, 2016. doi: 10.1007/s40684-016-0048-9.

[26] J. Fuchs, C. Schneider, and N. Enzinger, “Wire-based additive manufacturing using an electron beam as heat source,” Welding in the World, vol. 62, no. 2, pp. 267–275, Mar. 2018, doi: 10.1007/s40194-017-0537-7.

[27] J. W. Elmer et al., “Wire-based Additive Manufacturing of Stainless Steel Components The Welding Journal,” 2019.

[28] S. Pattanayak and S. K. Sahoo, “Gas metal arc welding based additive manufacturing - a review,” CIRP Journal of Manufacturing Science and Technology, vol. 33. Elsevier Ltd, pp. 398–442, May 01, 2021. doi: 10.1016/j.cirpj.2021.04.010.

[29] Y. Ding, M. Akbari, and R. Kovacevic, “Process planning for laser wire-feed metal additive manufacturing system,” International Journal of Advanced Manufacturing Technology, vol. 95, no. 1–4, pp. 355–365, Mar. 2018, doi: 10.1007/s00170-017-1179-z.

[30] K. Yurtişik, “Kinetics and Microstructural Analysis of Fatigue Fracture Progress in Weld Joints of Duplex Stainless Steel Grade 2205,” Middle East Technical University, 2013.

[31] P. Kah, H. Latifi, R. Suoranta, J. Martikainen, and M. Pirinen, “Usability of arc types in industrial welding,” International Journal of Mechanical and Materials Engineering, vol. 9, no. 1. University of Malaya, Dec. 01, 2014. doi: 10.1186/s40712-014-0015-6.

[32] D. Srinivasan, P. Sevvel, I. John Solomon, and P. Tanushkumaar, “A review on Cold Metal Transfer (CMT) technology of welding,” Mater Today Proc, vol. 64, pp. 108–115, Jan. 2022, doi: 10.1016/j.matpr.2022.04.016.

[33] M. Balasubramanian, M. V. Choudary, A. Nagaraja, and K. O. C. Sai, “Cold metal transfer process - A review,” in Materials Today: Proceedings, 2020, vol. 33, pp. 543–549. doi: 10.1016/j.matpr.2020.05.225.

[34] B. Choudhury and M. Chandrasekaran, “Investigation on welding characteristics of aerospace materials - A review,” 2017. [Online]. Available: www.sciencedirect.comwww.materialstoday.com/proceedings

[35] Y. Li, C. Su, and J. Zhu, “Comprehensive review of wire arc additive manufacturing: Hardware system, physical process, monitoring, property characterization, application and future prospects,” Results in Engineering, vol. 13. Elsevier B.V., Mar. 01, 2022. doi: 10.1016/j.rineng.2021.100330.

[36] C. R. de Farias Azevedo, H. Boschetti Pereira, S. Wolynec, and A. F. Padilha, “An overview of the recurrent failures of duplex stainless steels,” Engineering Failure Analysis, vol. 97. Elsevier Ltd, pp. 161–188, Mar. 01, 2019. doi: 10.1016/j.engfailanal.2018.12.009.

[37] American Society for Metals International, “Alloy Digest Sourcebook: Stainless Steels,” 2000. [Online]. Available: www.asminternational.org

[38] J. Charles, “Duplex Stainless steela - a Review after DSS ’07 held in Grado,” 2008, doi: 10.2374/SRI08SP063-79-2008-455.

[39] R. N. Gunn, Duplex Stainless Steels: Microstructure, Properties and Applications. 1997.

[40] V. Hosseini, “Super Duplex Stainless Steels-Microstructure and Properties of Physically Simulated Base and Weld Metal,” 2018.

[41] M. Knyazeva and M. Pohl, “Duplex Steels: Part I: Genesis, Formation, Structure,” Metallography, Microstructure, and Analysis, vol. 2, no. 2, pp. 113–121, Apr. 2013, doi: 10.1007/s13632-013-0066-8.

[42] N. I. A. Haddad, “The Development of Microstructure in Duplex Stainless Steel Welds,” University of Cambridge, 1989.

[43] J. Verma and R. V. Taiwade, “Effect of welding processes and conditions on the microstructure, mechanical properties and corrosion resistance of duplex stainless steel weldments—A review,” J Manuf Process, vol. 25, pp. 134–152, Jan. 2017, doi: 10.1016/j.jmapro.2016.11.003.

[44] H. Sieurin, “Fracture toughness properties of duplex stainless steels,” Royal Institute of Technology, 2006.

[45] J. O. Nilsson, “Super duplex stainless steels,” Materials Science and Technology (United Kingdom), vol. 8, no. 8, pp. 685–700, 1992, doi: 10.1179/mst.1992.8.8.685.

[46] J. Stützer, T. Totzauer, B. Wittig, M. Zinke, and S. Jüttner, “GMAW cold wire technology for adjusting the ferrite–austenite ratio of wire and arc additive manufactured duplex stainless steel components,” Metals (Basel), vol. 9, no. 5, May 2019, doi: 10.3390/met9050564.

[47] G. E. Dieter, Mechanical Metallurgy. 1988.

[48] T. L. Anderson, Fracture Mechanics Fundamentals and Applications. 2005.

[49] J. Luis Gonzalez Velazquez, A Practical Approach to Fracture Mechanics. 2021.

[50] F. Erdogan, “Fracture mechanics,” 2000. [Online]. Available: www.elsevier.com/locate/ijsolstr

[51] American Society for Testing and Materials, “E1019-18 Standard Test Methods for Determination of Carbon, Sulfur, Nitrogen, and Oxygen in Steel, Iron, Nickel, and Cobalt Alloys by Various Combustion and Inert Gas Fusion Techniques,” 2018

[52] J. Guo, Y. Zhou, C. Liu, Q. Wu, X. Chen, and J. Lu, “Wire arc additive manufacturing of AZ31 magnesium alloy: Grain refinement by adjusting pulse frequency,” Materials, vol. 9, no. 10, Oct. 2016, doi: 10.3390/ma9100823.

[53] American Society for Testing and Materials, “E1742/E1742M-18 Standard Practice for Radiographic Examination 1,” 2018 doi: 10.1520/E1742_E1742M-18.

[54] The International Organization for Standardization, “ISO 5817 Welding - Fusion-welded joints in steel, nickel, titanium and their alloys (beam welding excluded) - Quality levels for imperfections,” 2014

[55] American Society for Testing and Materials, “E562 Standard Test Method for Determining Volume Fraction by Systematic Manual Point Count 1,” 2020 doi: 10.1520/E0562-19E01.

[56] American Society for Testing and Materials, “E1245-03 Standard Practice for Determining the Inclusion or Second-Phase Constituent Content of Metals by Automatic Image Analysis 1,” 2016 doi: 10.1520/E1245-03R16.

[57] American Society for Testing and Materials, “E1508-12a Standard Guide for Quantitative Analysis by Energy-Dispersive Spectroscopy 1,” 2019 doi: 10.1520/E1508-12AR19.

[58] American Society for Testing and Materials, “E384-17 Standard Test Method for Microindentation Hardness of Materials 1,” 2021 doi: 10.1520/E0384-17.

[59] American Society for Testing and Materials, “E8/E8M-22 Standard Test Methods for Tension Testing of Metallic Materials 1,” 2022 doi: 10.1520/E0008_E0008M-22.

[60] The International Organization for Standardization, “ISO 6892-1 Metallic materials. Tensile testing Method of test at room temperature,” 2019

[61] The International Organization for Standardization, “ISO 12135 Metallic materials - Unified method of test for the determination of quasistatic fracture toughness,” 2021

[62] British Standards Institution, “BS 8571 Method of test for determination of fracture toughness in metallic materials using single edge notched tension (SENT) specimens,” 2018

[63] The International Organization for Standardization, “ISO 15653 Metallic materials - Method of test for the determination of quasistatic fracture toughness of welds,” 2018

[64] P. Ferro, F. Bonollo, G. Timelli, and A. Fabrizi, “Effect of microstructure and test temperature on impact toughness of superduplex stainless steel UNS S32760,” 2011, [Online]. Available: https://www.researchgate.net/publication/261794195

[65] U. Tosun, “Investigating The Fracture Behaviour Of X70M Linepipe Steel Girth Weldments via Single Edge Notched Tension and Bend Tests,” Middle East Technical University, 2018.

[66] American Society for Testing and Materials, “E1820-18 Standard Test Method for Measurement of Fracture Toughness,” 2019 doi: 10.1520/E1820-17.

[67] Det Norske Veritas, “DNVGL-RP-F108 Assessment of flaws in pipeline and riser girth welds,” 2017 [Online]. Available: http://www.dnvgl.com,

[68] C. Thaulow, E. Østby, B. Nyhus, Z. L. Zhang, and B. Skallerud, “Constraint correction of high strength steel Selection of test specimens and application of direct calculations,” Eng Fract Mech, vol. 71, no. 16–17, pp. 2417–2433, Nov. 2004, doi: 10.1016/j.engfracmech.2004.01.003.

[69] S. Cravero and C. Ruggieri, “Correlation of fracture behavior in high pressure pipelines with axial flaws using constraint designed test specimens - Part I: Plane-strain analyses,” Eng Fract Mech, vol. 72, no. 9, pp. 1344–1360, Jun. 2005, doi: 10.1016/j.engfracmech.2004.10.010.

[70] H. Pisarski and C. Wignall, “Fracture toughness estimation for pipeline girth welds,” in International Pipeline Conference, 2002.

[71] J. Xu, Z. L. Zhang, E. Østby, B. Nyhus, and D. B. Sun, “Effects of crack depth and specimen size on ductile crack growth of SENT and SENB specimens for fracture mechanics evaluation of pipeline steels,” International Journal of Pressure Vessels and Piping, vol. 86, no. 12, pp. 787–797, Dec. 2009, doi: 10.1016/j.ijpvp.2009.12.004.

[72] A. Karstensen, A. Horn, and M. Goldthorpe, “Constraint loss in welds due to geometry, loading mode and strength mismatch,” in 2nd International Symposium on High Strength Steel, 2002.

[73] B. Nyhus and M. L. Polanco, “SENT Specimens an Alternative to SENB Specimens for Fracture Mechanics Testing of Pipelines.”

[74] G. Benedetto Melis and L. Francesco Di Vito, “Measurement Of Fracture Resistance Of Pipelines For Strain Based Design,” 2015.

[75] S. Tiku, N. Pussegoda, M. Ghovanlou, W. R. Tyson, and A. Dinovitzer, “Standardization of SENT (or Se(T)) Fracture Toughness Measurement: Results of A Round Robin on A Draft Test Procedure,” 2016.

[76] Y. G. Matvienko, “The effect of crack-tip constraint in some problems of fracture mechanics,” Eng Fail Anal, vol. 110, Mar. 2020, doi: 10.1016/j.engfailanal.2020.104413.

[77] X. K. Zhu, “Full-range stress intensity factor solutions for clamped SENT specimens,” International Journal of Pressure Vessels and Piping, vol. 149, pp. 1–13, Jan. 2017, doi: 10.1016/j.ijpvp.2016.11.004.

[78] P. W. Fuerschbach and G. A. Knorovsky, “A Study of Melting Efficiency in Plasma Arc and Gas Tungsten Arc Welding A method for selecting optimal weld schedules to minimize net heat input is derived from calorimetric measurements,” pp. 287–298, 1991.

[79] J. N. Dupont and A. R. Marder, “Thermal Efficiency of Arc Welding Processes,” pp. 406–416, 1995.

[80] S. Utyuzhnikov et al., “Numerical modelling subsonic and supersonic inductive plasma flows,” in ECCOMAS Computational Fluid Dynamics Conference 2001, 2001. [Online]. Available: https://www.researchgate.net/publication/229044428

[81] O. Grong, Metallurgical Modelling of Welding, vol. Second Edition. 1997.

[82] K. Yurtisik, S. Tirkes, I. Dykhno, C. Hakan Gur, and R. Gurbuz, “Characterization of Duplex Stainless Steel Weld Metals Obtained by Hybrid Plasma-Gas Metal Arc Welding,” vol. 18, no. 03, pp. 207–216, 2013.

[83] P. D. Southwick and R. W. K Honeycombe, “Decomposition of ferrite to austenite in 26%Cr-5%Ni stainless steel,” 1980.

[84] V. A. Hosseini, L. Karlsson, S. Wessman, and N. Fuertes, “Effect of sigma phase morphology on the degradation of properties in a super duplex stainless steel,” Materials, vol. 11, no. 6, Jun. 2018, doi: 10.3390/ma11060933.

[85] B. Raha, “Study on Deleterious Phases Precipitation on Super Duplex Stainless Steel Grade 6A-ASTM A890,” Mater Today Proc, vol. 5, pp. 7836–7844, 2018, [Online]. Available: www.sciencedirect.comwww.materialstoday.com/proceedings2214-7853

[86] G. C. L. D. Freitas, G. S. da Fonseca, L. P. Moreira, and D. N. F. Leite, “Phase transformations of the duplex stainless steel UNS S31803 under non-isothermal conditions,” Journal of Materials Research and Technology, vol. 11, pp. 1847–1851, Mar. 2021, doi: 10.1016/j.jmrt.2021.02.008.

[87] K. H. Lo, C. T. Kwok, and W. K. Chan, “Characterisation of duplex stainless steel subjected to long-term annealing in the sigma phase formation temperature range by the DLEPR test,” Corros Sci, vol. 53, no. 11, pp. 3697–3703, 2011, doi: 10.1016/j.corsci.2011.07.013.

[88] N. Llorca-Isern, H. López-Luque, I. López-Jiménez, and M. V. Biezma, “Identification of sigma and chi phases in duplex stainless steels,” Mater Charact, vol. 112, pp. 20–29, Feb. 2016, doi: 10.1016/j.matchar.2015.12.004.

[89] L. Liao, Z. Zhao, F. Xu, W. Zhang, and J. Li, “Influence of N on precipitation behavior and transformation kinetics of super austenitic stainless steels after isothermal ageing at 900 °C,” Journal of Materials Research and Technology, vol. 19, pp. 3670–3684, Jul. 2022, doi: 10.1016/j.jmrt.2022.06.111.

[90] N. Sathirachinda, R. Pettersson, and J. Pan, “Depletion effects at phase boundaries in 2205 duplex stainless steel characterized with SKPFM and

TEM/EDS," Corros Sci, vol. 51, no. 8, pp. 1850–1860, Aug. 2009, doi: 10.1016/j.corsci.2009.05.012.

[91] M. Pohl, O. Storz, and T. Glogowski, "Effect of intermetallic precipitations on the properties of duplex stainless steel," Mater Charact, vol. 58, no. 1, pp. 65–71, Jan. 2007, doi: 10.1016/j.matchar.2006.03.015.

[92] K. Chandra, R. Singhal, V. Kain, and V. S. Raja, "Low temperature embrittlement of duplex stainless steel: Correlation between mechanical and electrochemical behavior," Materials Science and Engineering A, vol. 527, no. 16–17, pp. 3904–3912, Jun. 2010, doi: 10.1016/j.msea.2010.02.069.

[93] I. Mészáros and B. Bögre, "Complex study of eutectoidal phase transformation of 2507-type super-duplex stainless steel," Materials, vol. 12, no. 13, Jul. 2019, doi: 10.3390/ma12132205.

[94] C. M. Garzón and A. J. Ramirez, "Growth kinetics of secondary austenite in the welding microstructure of a UNS S32304 duplex stainless steel," Acta Mater, vol. 54, no. 12, pp. 3321–3331, Jul. 2006, doi: 10.1016/j.actamat.2006.03.018.

[95] S. Atamert and J. E. King, "Super duplex stainless steels Part 1 Heat affected zone microstructures," 1992.

[96] D. R. Eo, S. G. Chung, J. H. Yang, I. H. Jung, and J. W. Cho, "Numerical modeling of oxide particle evolution during additive manufacturing," Addit Manuf, vol. 51, Mar. 2022, doi: 10.1016/j.addma.2022.102631.

[97] X. han Wu, Z. gang Song, L. zhou Liu, J. guo He, and L. Zheng, "Effect of secondary austenite on fatigue behavior of S32750 super duplex stainless steel," Mater Lett, vol. 322, Sep. 2022, doi: 10.1016/j.matlet.2022.132487.

[98] X.-H. Wu, Z.-G. Song, J.-G. He, H. Feng, B.-S. Wang, and M.-H. Wu, “Effect of secondary austenite on the mechanical properties of UNS S32750 duplex stainless steel.”

[99] V. A Hosseini, L. Karlsson, D. Engelberg, and S. Wessman, “Time-temperature-precipitation and property diagrams for super duplex stainless steel weld metals,” Welding in the World, vol. 62, no. 3, pp. 517–533, May 2018, doi: 10.1007/s40194-018-0548-z.

[100] V. Muthupandi, P. B. Srinivasan, S. K. Seshadri, and S. Sundaresan, “Effect of nitrogen addition on formation of secondary austenite in duplex stainless steel weld metals and resultant properties,” Science and Technology of Welding and Joining, vol. 9, no. 1, pp. 47–52, Jan. 2004, doi: 10.1179/136217104225017143.

[101] Z. Zhang, H. Jing, L. Xu, Y. Han, L. Zhao, and C. Zhou, “Effects of nitrogen in shielding gas on microstructure evolution and localized corrosion behavior of duplex stainless steel welding joint,” Appl Surf Sci, vol. 404, pp. 110–128, May 2017, doi: 10.1016/j.apsusc.2017.01.252.

[102] Q. Wang, G. Gu, C. Jia, C. Wu, and K. Li, “Investigation of Microstructure Evolution, Mechanical and Corrosion Properties of SAF 2507 Super Duplex Stainless Steel Joints by Keyhole Plasma Arc Welding,” Journal of Materials Research and Technology, Nov. 2022, doi: 10.1016/j.jmrt.2022.11.107.

[103] Z. Zhang, H. Jing, L. Xu, Y. Han, G. Li, and L. Zhao, “Investigation on Microstructure and Impact Toughness of Different Zones in Duplex Stainless Steel Welding Joint,” J Mater Eng Perform, vol. 26, no. 1, pp. 134–150, Jan. 2017, doi: 10.1007/s11665-016-2441-5.

[104] Y. Zou, R. Ueji, and H. Fujii, “Effect of oxygen in shielding gas of advanced A-TIG (AA-TIG) welding on crystallographic orientation relationship of duplex stainless steel weld.”

[105] M. A. García Rentería, V. H. López Morelos, R. G. García Hernández, F. Curiel López, and J. Lemus Ruíz, “Effect on the microstructure and mechanical properties of the electromagnetic stirring during GMA welding of 2205 DSS plates,” Materials Science Forum, vol. 755, pp. 61–68, 2013, doi: 10.4028/www.scientific.net/MSF.755.61.

[106] B. Blessto, S. Katakam, M. Veerappan, and M. Arumugam, “Effect of crack path and high angle grain boundaries on fracture toughness and fatigue behaviour of cryorolled AA2219,” Fatigue Fract Eng Mater Struct, vol. 43, no. 11, pp. 2608–2622, Nov. 2020, doi: 10.1111/ffe.13320.

[107] Z. Zhang, H. Jing, L. Xu, Y. Han, and L. Zhao, “Investigation on microstructure evolution and properties of duplex stainless steel joint multi-pass welded by using different methods,” Mater Des, vol. 109, pp. 670–685, Nov. 2016, doi: 10.1016/j.matdes.2016.07.110.

[108] H. Guo, S. Yang, T. Wang, H. Yuan, Y. Zhang, and J. Li, “Microstructure evolution and acicular ferrite nucleation in inclusion-engineered steel with modified MgO@C nanoparticle addition,” J Mater Sci Technol, vol. 99, pp. 277–287, Feb. 2022, doi: 10.1016/j.jmst.2021.02.033.

[109] N. Haghdadi, P. Cizek, P. D. Hodgson, and H. Beladi, “Microstructure dependence of impact toughness in duplex stainless steels,” Materials Science and Engineering A, vol. 745, pp. 369–378, Feb. 2019, doi: 10.1016/j.msea.2018.12.117.

[110] T. Inoue, F. Yin, Y. Kimura, K. Tsuzaki, and S. Ochiai, “Delamination effect on impact properties of ultrafine-grained low-carbon steel processed by warm caliber rolling,” Metall Mater Trans A Phys Metall Mater Sci, vol. 41, no. 2, pp. 341–355, Feb. 2010, doi: 10.1007/s11661-009-0093-x.

[111] B. Verhaeghe, F. Louchet, Y. Brechet, and J.-P. Massoud, “Damage and Rupture Mechanisms in an Austenoferritic Duplex Steel,” Actu muter, vol. 45, no. 5, 1997.

[112] X. Min, Y. Kimura, T. Kimura, and K. Tsuzaki, “Delamination toughening assisted by phosphorus in medium-carbon low-alloy steels with ultrafine elongated grain structures,” Materials Science and Engineering A, vol. 649, pp. 135–145, Jan. 2016, doi: 10.1016/j.msea.2015.09.102.

[113] A. L. Rouffié et al., “Influences of process parameters and microstructure on the fracture mechanisms of ODS steels,” Journal of Nuclear Materials, vol. 433, no. 1–3, pp. 108–115, 2013, doi: 10.1016/j.jnucmat.2012.08.050.

[114] M. Pozuelo, F. Carreño, and O. A. Ruano, “Delamination effect on the impact toughness of an ultrahigh carbon-mild steel laminate composite,” Compos Sci Technol, vol. 66, no. 15, pp. 2671–2676, Dec. 2006, doi: 10.1016/j.compscitech.2006.03.018.

[115] I. N. Bastos, S. S. M. Tavares, F. Dalard, and R. P. Nogueira, “Effect of microstructure on corrosion behavior of superduplex stainless steel at critical environment conditions,” Scr Mater, vol. 57, no. 10, pp. 913–916, Nov. 2007, doi: 10.1016/j.scriptamat.2007.07.037.

[116] D. M. Fellicia, Sutarsis, B. A. Kurniawan, D. Wulanari, A. Purniawan, and A. T. Wibisono, “Study of Sigma Phase in Duplex SAF 2507,” in IOP Conference Series: Materials Science and Engineering, May 2017, vol. 202, no. 1. doi: 10.1088/1757-899X/202/1/012039.

[117] A. Sarkar et al., “Relating microstructures of hierarchical tertiary phases with corrosion performance in a super duplex stainless steel,” Mater Charact, vol. 194, Dec. 2022, doi: 10.1016/j.matchar.2022.112426.

[118] M. B. C Quigley, P. H. Richards, D. T. Swift-Hook, and A. E. F Gick Ma, “Heat flow to the workpiece from a TIG welding arc,” J. Phys. D: Appl. Phys,

vol. 6, p. 2250, 1973, [Online]. Available: http://iopscience.iop.org/0022-3727/6/18/310

[119] H. Smartt, J. Stewart, and C. Einerson, “Heat transfer in gas tungsten arc welding,” 85 ASM International Welding Congress, 1985.

[120] P. Salvetr et al., “Characterization of super duplex stainless steel SAF2507 deposited by directed energy deposition,” Materials Science and Engineering A, vol. 857, Nov. 2022, doi: 10.1016/j.msea.2022.144084.

[121] G. Zhao, R. Zhang, J. Li, H. Li, L. Ma, and Y. Li, “Study on microstructure and tensile damage evolution of 2205 duplex steel at different solution temperatures,” Materials Today Communications, vol. 33. Elsevier Ltd, Dec. 01, 2022. doi: 10.1016/j.mtcomm.2022.104472.

[122] N.-Y. Tang, K.-F. Yao, N.-P. Chen, and A. Plumtree, “In Situ Fracture Experiment on a Duplex Stainless Steel,” Materials" Science and Engineering, A, vol. 1, no. 7, pp. 157–165, 1989.

[123] E. Erauzkin and A. M. MIrisarri, “Effect of The Testing Temperature on The Fracture Toughness of a Duplex Stainless Steel,” vol. 25, pp. 1731–1736, 1991.

[124] P. Joly, R. Cozar, and A. Pineau, “Effect of Crystallographic Orientation of Austenite on The Formation of Cleavage Cracks in Ferrite in an Aged Duplex Stainless Steel,” vol. 24, pp. 2235–2240, 1990.